UNCONVENTIONAL PROCESSING AND CHARACTERIZATION METHODS IN LITHOGRAPHY

by Jing Sha

UNCONVENTIONAL PROCESSING AND CHARACTERIZATION METHODS IN LITHOGRAPHY

A Dissertation

Presented to the Faculty of the Graduate School

of Cornell University

in Partial Fulfillment of the Requirements for the Degree of

Doctor of Philosophy

by

Jing Sha

August 2010

UNCONVENTIONAL PROCESSING AND CHARACTERIZATION METHODS IN LITHOGRAPHY

Jing Sha, Ph.D.

Cornell University 2010

As lithography moves toward feature sizes of 22 nm and smaller and pushing for applications beyond the semiconductor industry, unconventional processing and characterization methods are in demand for patterning of unusual structures, new processing techniques, and better understanding and control of resist performance. Chapter 1 introduces conventional lithographic processing and characterization methods and their unconventional counterparts as well. As a typical lithographic process includes exposure, post-exposure bake, and development, chapters 2, 3 and the appendix cover some unconventional processing methods. Chapter 2 discusses a laser heating method for exposed chemically amplified photoresists in an attempt to control acid diffusion during post-exposure bake and thus improve pattern resolution and quality. Chapter 3 details supercritical carbon dioxide as an environmentally friendly and sustainable solvent to develop high resolution resist patterns. Two photon lithography is demonstrated in the appendix as a direct write technique to introduce three dimensional defects inside photonic materials. While conventional characterization of the materials and/or patterns is usually carried out before and after the lithographic process, an *in situ* FTIR method is discussed in chapter 4 as a technique to monitor reaction-diffusion kinetics of acids in chemically amplified molecular glass resists during post-exposure bake and to understand the molecular architectural effect on the kinetics.

BIOGRAPHICAL SKETCH

Jing Sha was born on November 20, 1982 in Shanghai, China. After high school, she remained in Shanghai and enrolled in Fudan University in 2001. Although she almost started medical school on her first day in college to become a real doctor, she was somehow led by fate to major in Physics and received her Bachelor of Science degree in 2005. At the end of her sophomore year, Jing was awarded the title of "Chun-Tsung Scholar", granted by Nobel Physics Prize laureate Dr. Tsung-Dao Lee, along with an undergraduate research opportunity in Prof. Jian Zi's lab. For the "Chun-Tsung" program and her senior thesis, Jing studied photonic crystal and structural coloration in the nature through experiments and some computational simulation under the guidance of Prof. Zi. Throughout the four years at Fudan, she also became fairly interested in other areas of experimental condensed matter physics such as organic semiconductors, which inspired her to switch to materials science for graduate study.

In August 2005, Jing enrolled in Department of Materials Science and Engineering at Cornell University where she joined Prof. Christopher Ober's group. As her projects changed with funding sources, she carried out research in different areas of lithography. In the summer of 2009, she participated in the collaboration with Polymers Division of National Institute of Standards and Technology (Gaithersburg, MD) where she conducted a fundamental study on reaction-diffusion kinetics of acids in photoresists. Other highlights of her time in graduate school include earning Enid Seaton Ruoff Teaching Assistant Award, receiving the highest score in the cooking class offered at the hotel school, and developing significant interest in investment and metaphysics. After finishing her Ph.D. degree in 2010, Jing will join the semiconductor industry in the hope of enjoying more spare time to work towards her dream life.

To my parents

ACKNOWLEDGEMENTS

I would most sincerely like to thank Professor Christopher Ober for recruiting me into his research group and providing his insightful guidance. I am very grateful for his encouragement and faith in me especially when sometimes even I doubted myself. I would also like to thank Professor Michael Thompson, a co-advisor in one of my projects, for his enlightenment and advising, and Professor Chris Xu for his assistance in my committee.

I'd also like to acknowledge several funding sources for sponsoring me to conduct research throughtout the years: Cornell Center for Materials Research (CCMR), National Science Foundation (NSF), SRC/ERC Center for Environmentally Benign Semiconductor Manufacturing, and Intel Corporation.

I would like to express gratitude to the Polymers Division of National Institute of Standards and Technology (Gaithersburg, MD) for hosting me in the summer of 2009. Special thanks to the division chief Dr. Eric Lin, the electronic materials group leader Dr. Chris Soles and the photoresist project leader Dr. Vivek Prabhu for making my internship possible and very productive.

I would also like to thank some of the present and former members of the Ober group who have helped me along the way in research: Dr. Jin-Kyun Lee, Byungki Jung, Dr. Anuja De Silva, Dr. Nelson Felix, Dr. Margarita Chatzichristidi, Eisuke Murotani, Dr. Manabu Tanaka, etc.. I'm glad that I've also developed friendship with them outside the lab and they've made my life in graduate school much more colorful. I'd also like to thank the rest of the Ober Group for keeping a very friendly working environment and making our group activities so enjoyable.

I am very grateful to the plentiful research and studying resources that I have enjoyed at Cornell. Special thanks to Cornell Nanoscale Facilities (CNF) and

Cornell Center for Materials Research (CCMR) for their advanced equipment and extremely helpful staff members. Also, my spare time has been enriched by the large and diverse Cornell PE program and several classes taken and audited at the hotel school and Johnson business school.

Last but not least, I would like to thank my parents for their unconditional love, support, and encouragement. Special gratitude to my dad who is always there for me as the greatest listener and counselor.

I remember Prof. Ober once saying that every student undergoes some (personality) changes more or less on the way to getting their Ph.D.'s. I feel like I was dramatically broken and reshaped at Cornell and have grown spiritually throughout graduate school. I am grateful to all the encounters that I have had here, whether pleasant or not so much, because they shaped who I am now one way or the other.

TABLE OF CONTENTS

LIST OF TABLES

LIST OF FIGURES

CHAPTER 1

INTRODUCTION

1.1 Overview of Lithography

Lithography was first invented in 1796 as a low-cost method of printing theatrical works by using a stone or a metal plate with a completely smooth surface. With the development of the semiconductor industry in the last few decades, lithography has broadened its meaning to fabrication of patterned materials on a very fine scale for applications like integrated circuits (ICs), microelectromechanical system (MEMS) and other semiconductor devices.

Microlithography or nanolithography involves several consecutive processing steps, e.g. imaging/exposure, post-exposure bake, and development. As depicted in Figure 1.1, the traditional lithographic process involves use of radiation-sensitive organic materials called ”resists” or ”photoresists” to produce patterns on substrates such as single crystals of silicon. The resist material is applied by spin-coating to form sub-0.1 - 1 μm thick films on substrates (wafers). The wafers are subsequently baked on hot plates to remove casting solvents. The resist films are then exposed through a mask (photolithography) or directly with finely focused electron beams (electron-beam lithography). Following the exposure, certain resists, especially chemically amplified resists, need to be baked for thermally activated catalytic chemical reactions in the resists. The exposed resist films are subsequently developed like photographic films with a developer solvent to generate relief images. Resist materials are generally classified as positive-tone or negative-tone. The exposed resist areas are rendered more/less soluble than the unexposed areas in the developer

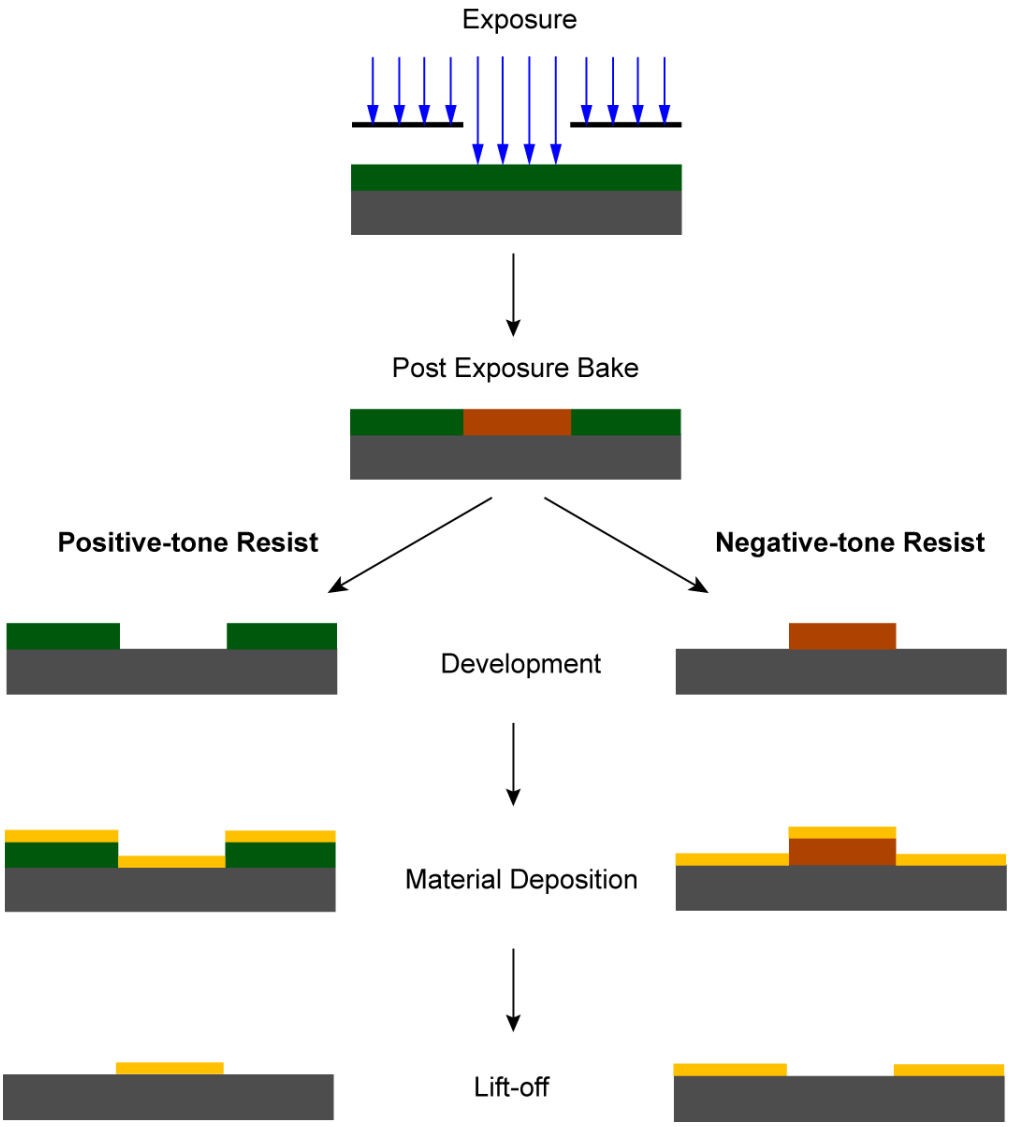

Figure 1.1: Conventional lithographic processing steps of positive- and negative-tone resists.

for positive-tone/negative-tone resists. The resist film remaining after development functions as a protective stencil during low temperature deposition of materials or etching of the wafer. The resist film must protect the underlying substrate while the areas dissolved during development are being deposited with a thin film of a specific material or etched. The resist film remaining after deposition or etching is finally removed, leaving behind desired patterns

in the substrate. The whole process is repeated several times to fabricate complex semiconductor devices. A post-development lift-off step is demonstrated in Figure 1.1.

Characterization of resist materials and/or patterns is usually carried out before and after the lithographic process for better understanding and control of resist performance. Components of resist formulation are generally analyzed to determine their purity and molecular weights, thermal and optical properties, and dissolution rates in developers. Also, quality inspection of patterned resist films is of paramount importance to optimization of resist lithographic performance.

1.2 Conventional Processing and Characterization Methods

1.2.1 Exposure Methods

Contact/Proximity Printing

The simplest type of printing machine is a contact aligner where a photomask is pressed in direct contact with a resist-coated wafer during illumination. The first integrated circuits had features of 200 micrometres which were printed using a contact aligner. Contact printing is still commonly practised nowadays, mainly in applications requiring thick resist and/or double-sided alignment and exposure.

In a typical contact exposure system, the photomask is placed with chrome-

side down in a frame right below the miscroscope objectives. The resist-coated wafer is moved by vernier screws with respect to the photomask. Once the wafer is aligned to the photomask, vacuum is applied between the two and the microscope objectives are retracted. A common irradiation source is a high intensity mercury lamp with wavelength filters.

Ideally, because of the direct contact between the wafer and the photomask, the gap between the two goes to zero and diffraction effects get minimized. In reality, the gap cannot be zero because neither the wafer nor the photomask is perfectly flat. Upon exiting the photomask/resist interface, the irradiation light is subject to near-field diffraction as it propagates through the resist film. Diffraction causes the image to lose contrast with increasing depth into the resist. Imaging resolution of contact aligners using common irradiation sources is about 0.5 μm.

The major disadvantage of contact printing is defect generation due to the contact between the resist-coated wafer and the photomask. Defects can be generated on both the resist film and the photomask on every contact cycle. Therefore, contact aligners are typically limited to applications that can tolerate high defect levels. Proximity printing was developed to avoid defect generation by floating the photomask off the surface of the wafer usually on a flow of nitrogen. A common gap of 10-50 μm reduces defect generation sharply. The major problem of proximity printing is a reduction in resolution due to diffraction. Another disadvantage of introducing a small gap in proximity printing is that the variations in the gap can lead to line width variations across the wafer.

Projection Printing

Projection aligners have become by far the most widely used exposure tool in the semiconductor industry. The most common projection system is step and repeat projection aligners (also known as steppers) frequently with a 5:1 reduction reduction built in, which is an advantage over the 1:1 pattern transfer in contact/proximity aligners. This means that only a small region of the wafer, also known as a field (typically 0.5-3 cm^2), is exposed at a time, which allows systems to be built with very high NA lenses and thus high resolution. Between exposures, the wafer is mechanically moved in the stepper to the next field.

The resolution of an optical aligner is determined by the optical limitation of the lenses, which can be referred to as Rayleigh's criterion

$$W_{min} \approx k\frac{\lambda}{NA} = k\frac{\lambda}{n\sin(\alpha)} \tag{1.1}$$

where λ is the exposure light wavelength, α is one-half the angle of maximum cone of light that can enter or exit the lens, n is the refractive index of the medium between the objective and the wafer, and k is a constant (typically 0.4-0.8) dependent on the ability of the resist to distinguish between small changes in intensity.

In the effort to continue scaling resolution W_{min} to smaller dimensions, the exposure tools can be tuned to reduce exposure light wavelength λ and increase the numerical aperture NA of the system. The common ligth sources used in contact aligners and steppers are in the ultraviolet regime (typically $\approx 250 - 405$ nm). The past decade has seen significant development in light exposure tools operating at shorter wavelengths, e.g. 193 nm and 13.5 nm (extreme UV, a.k.a. EUV).

Immersion Lithography

Until recently, the photolithography operating medium was always air (refractive index $n = 1$). By replacing air with water ($n = 1.33$) or higher index immersion liquids, the minimum patternable feature size can be lowered according to Equation 1.1. Immersion lithography using 193 nm light is the leading exposure technique for top-notch IC fabrication at this writing. For the 32 nm node fabrication in 2009, Intel began using immersion lithography and confirmed that since EUV was not available, it would extend 193 nm immersion lithography to the 22 nm node [1] and 15 nm node [2]. Intel has already outlined a path to use 193 nm immersion lithography down to 11 nm node.[3]

As a photolithography resolution enhancement technique, immersion lithography is implemented by having the liquid dispersed locally from the nozzle onto the resist-coated wafer to be exposed. After exposure, the lens moves to the next exposure site with the liquid remaining under the lens due to surface tension. Another method is to draw the liquid back into the nozzle after exposure and redispense it onto the next field.

Some of the concerns with immersion lithography include: 1) presence of impurities in the immersion fluid resulting in defects in the resist pattern; 2) potential interaction between the immersion fluid and the resist; 3) refractive index mismatch between the immersion fluid and the resist resulting in high reflection at the interface. To overcome these obstacles, significant effort is needed for the design of resists to meet the special requirements of 193 nm immersion lithography.

EUV Lithography

EUV lithography is one of the next-generation lithography technologies using the 13.5 nm EUV wavelength. It is a significant departure from the aforementioned deep ultraviolet lithography. Since all matters absorb EUV radiation, EUV lithography needs to take place under vacuum and all the optical elements, including the photomask, must make use of defect-free Mo/Si multilayers which act to reflect light by means of interlayer interference. Due to certain unsolved technical issues of EUV exposure tools and photomasks and the negative impact of the significant reduction/increase in wavelength/photon energy, EUV lithography currently cannot replace 193 nm immersion lithography and double patterning techniques as the mainstream patterning technology beyond the 22 nm node.

Electron Beam Lithography

Electron beam lithography (EBL) may be used either for photomask generation or directly writing patterns on resist-coated wafers. EBL is the main technology for mask generation due to its ability to accurately pattern fine features. Although several versions of projection and proximity EBL systems have also been developed [4], most EBL tools are direct-write systems which move a small electron beam spot with respect to the substrate to expose the resist pixel by pixel. Throughput, therefore, is the major concern for broad application of EBL for IC manufacturing. High brightness electron sources, vector scan systems, and correction of proximity effect have all been developed to improve throughput, but EBL still remains an order of magnitude slower than optical lithography.[5]

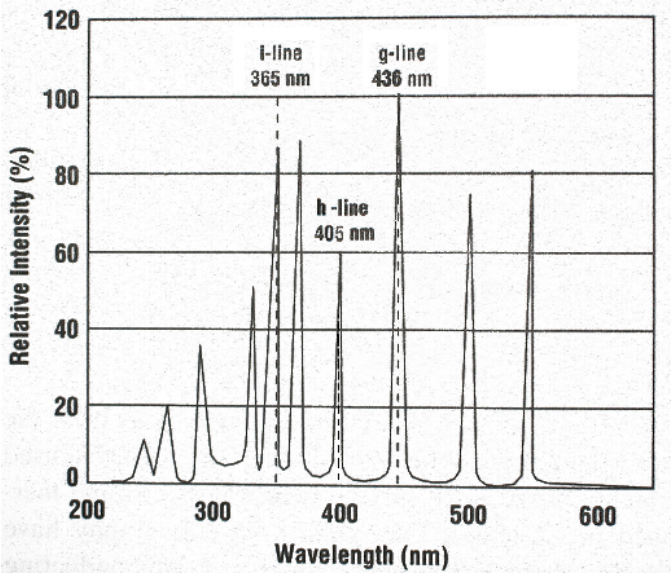

Figure 1.2: Line spectra of a typical mercury arc lamp.

1.2.2 Thermal Bake Steps

Chemically Amplification Concept for Resists

The most common type of optical source for photolithography has long been the high pressure arc lamp, which is the brightest incoherent sources available. Mercury arc lamps can still be found in many steppers and contact aligners nowadays. Figure 1.2 shows the line spectra of a typical mercury lamp. Contact aligners and steppers usually filter out but a single line. Exposure wavelengths commonly used in exposure tools are g-line (436 nm), h-line (405 nm), and i-line (365 nm). The drive to higher resolution necessitated a further shift from i-line to deep UV employing the 254 nm emission from Xe-Hg lamps or the 248 nm emission from KrF excimer lasers. The Hg discharge lamp had an extremely small output at 254 nm while insertion of many optical elements between the KrF laser source and the wafer plane dramatically reduced the radiation output

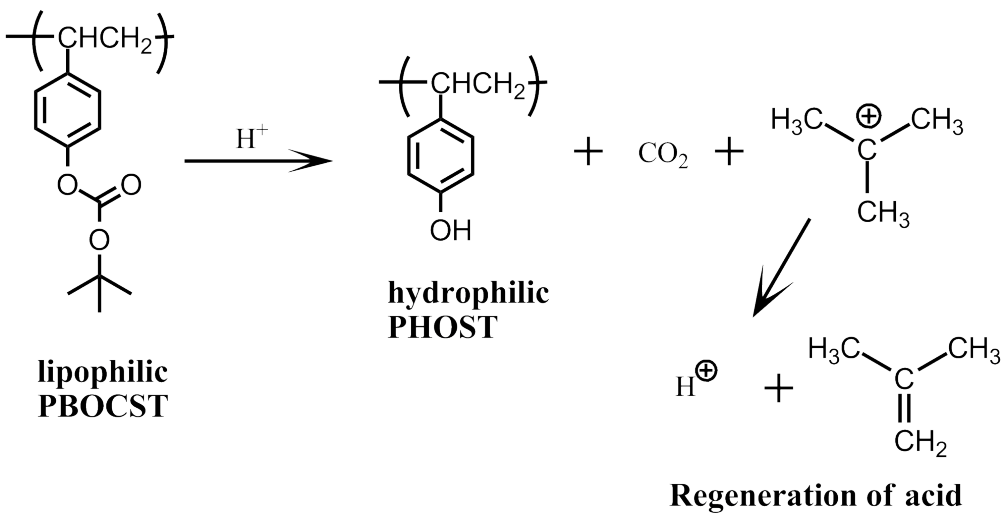

Figure 1.3: Acid-catalyzed deprotection for polarity change of a *t*BOC-protected resist adapted from Reference [42].

to the resist film. Therefore, the shift to deep UV lithography required a completely new resist concept that could improve resist sensitivity to counteract the low intensity of exposure light.

The chemical amplification concept has become the exclusive foundation for advanced high resolution resist systems and played such a pivotal role in realization of lithography in the deep UV regime and beyond that most resists used nowadays are chemically amplified. In 1982, Ito, Willson, and Fréchet proposed the concept of chemical amplification[6, 7, 8], where irradiation activates photoacid generators in the resist film and the generated photoacids subsequently catalyze numerous (typically ≈ 100) reactions in the resist before being trapped or quenched. An example of a chemically amplified resist is illustrated in Fig. 1.3. The catalytic chemical transformations are generally accomplished by heating the exposed resist film (post exposure bake).

Post Apply Bake

Since the shift to chemically amplified resists was not evolutionary but revolutionary, many problems unique to chemically amplified resists have surfaced and these problems were typically related to the catalytic nature of the resists. For example, a trace amount of airborne base such as *N*-methylpyrrolidone (NMP) and amines absorbed by the chemically amplified resist film upon standing after coating (especially after exposure) interferes with the desired acid catalyzed reaction, resulting in formation of an insoluble surface layer (T-topping) in positive-tone resists and in linewidth shift in negative-tone resists. Good annealing and thus reduced free volume was found essential to decrease the amount of NMP absorbed by resist films.[9]

Post apply bake (PAB) steps can not only remove residual solvent from the spin cast films but also reduce the free volume of the resist film by annealing in an appropriate temperature range where the resist components are thermally and hydrolytically stable.[10, 11] Post apply bake is usually conducted on a hotplate or in an oven.

Post Exposure Bake

Post exposure bake (PEB) is not required for all resists but almost all chemically amplified resists. Chemically amplified resists require PEB to accelerate acid-catalyzed reactions due to high activation energies in general. PEB is normally done on a hot plate (typically with vacuum applied between wafers and hot plates to remove the air gap and promote heat conduction) at a temperature of 90 - 150 ^{o}C for 30 - 120 seconds. To finish the PEB step, wafers are removed from

hot plates and placed on chill plates to reach room temperature. Hot plate annealing is a fairly simple and convenient method for post exposure bake but it is not perfect for uniform heat distribution over the hot plate and uniform heat conduction from the hot plate to the exposed resist-coated wafer resulting from hot plate's intrinsic tool limitation and variation of thickness and flatness across the resist-coated wafer respectively. The resulting non-uniform heat distribution in the resist on top of the wafer can ultimately lead to non-uniform critical dimension (CD) of resist patterns across the wafer.

Study of PEB has attracted serious attention in the resist community because PEB not only provides heat for the catalytic chemical reactions in the exposed resist film but also allows for acid diffusion during the thermal process. Acid diffusion in chemically amplified resists during PEB has been found to have two opposing effects on line edge roughness (LER) of developed resist patterns [12]: 1. smoothing out the spatial distribution of photochemical events at the interface between exposed and unexposed regions and thus reducing LER; 2. degrading image contrast and thus increasing LER. Quantifying acid diffusion in chemically amplified resists is an active area of research in lithography to improve LER of resist patterns and ultimately the LER transferred to the underlayers after etching through the resist.

1.2.3 Development

Traditional development of resist films uses organic solvents or most often aqueous base, in which dissolution rates of exposed and unexposed regions of the resist films show significant difference resulting in pattern contrasts.

The development process was discovered to be a large contributor to sidewall roughness of developed resist patterns mainly through the effects of development time and developer concentration.[13] The development process contributed on the order of 2.5 - 3 nm rms to the roughness in the resist studied in the reference. Experimental results showed that the lower the developer concentration the smaller the resist LER and that the shorter the development time the smaller the resist LER.

1.2.4 Characterization

Characterization in lithography basically has two categories: characterization of resist materials and characterization of resist patterns. Typical analysis methods of resist materials include gel permeation chromatography (GPC) and matrix-assisted laser desorption/ionization (MALDI) for molecular weight determination of resist polymers, differential scanning calorimetry (DSC) and thermal gravimetric analysis (TGA) for the glass transition and thermal decomposition temperatures of resist components, x-ray reflectometry for (electron) density of resist film, and infrared spectroscopy (IR) for resist composition and change in chemical environment. The most common analysis technique of resist patterns is scanning electron microscopy (SEM), both top-down and cross-sectional. SEM images are usually processed with such technical software as SuMMIT (an interactive off-line analysis package developed by EUV Technology Corporation) for critical dimension (CD) and line-edge/width roughness (LER/LWR) measurement.

1.3 Unconventional Processing and Characterization Methods

The exploration of unconventional processing and characterization methods in lithography has been driven by increasing demand for higher device quality, burgeoning novel designs of micro- or nano-scale devices, and more environmentally friendly processing conditions. This section covers a selection of the most important contributions in the area.

1.3.1 Exposure Methods

Interference Lithography

In physics, interference is defined as the superposition of two or more waves that results in a new wave pattern. When two or more optical waves are present simultaneously in the same region of space, the optical waves interfere and generate a periodic spatial modulation of light. Interference lithography is a technique for patterning periodic fine resist features using the spacial modulation of light intensity in the resist film. The photochemistry and lithographic processes involved in interference lithography are similar to those in conventional lithography except that photomasks and complex optical systems are not required, and the substrate may be transparent since all of the laser beams are not necessarily launched from the same side of the substrate.

Interference among any N ($\leq$4) collimated and coherent laser beams produces an intensity grating with (N-1) dimensional periodicity if the difference between the wave vectors is non-coplanar. This means that 1D periodicity (line patterns) can be produced by 2 laser beams, 2D periodicity (e.g. dot patterns) by

3 beams, and 3D structures by 4 beams.[14, 15, 16] Despite the high throughput, interference lithography is only capable of patterning periodic patterns, which limits itself from a broader application.

Phase Mask Lithography

Phase masks are alternating [17] or attenuated [18] phase shift photomasks that take advantage of the interference generated by phase differences to improve image resolution in photolithography. A conventional photomask is a transparent plate with the same thickness everywhere, parts of which are covered with non-transmitting material in order to image patterns in the resists. In alternating phase-shift masks, certain transmitting regions are made thinner or thicker to induce a phase-shift in the light traveling through those regions of the mask, which results in interference between the phase-shifted light and the non-modulated transmission light. Attenuated phase-shift masks employ a different approach. Certain light-blocking regions of the mask are modified to allow a small amount of light to be transmitted through (typically just a few percent). The attenuated light is not strong enough to produce patterns in the resists, but it can interfere with the light coming from the transparent parts of the mask. Phase mask lithography is not just limited to two-dimensional patterning. Conformable poly(dimethylsiloxane) (PDMS) phase masks have also been explored to pattern large-area three-dimensional non-crystalline nanostructures.[20, 155]

Two-Photon Lithography

Two-photon lithography takes advantage of two-photon absorption of such resist components as photoinitiators and photoacid generators to trigger chemical reactions in the resist. It provides high-resolution mask-directed [21] or mask-free [22] microfabrication capabilities in three dimensions. This unconventional exposure method will be discussed in the appendix in detail.

1.3.2 Post Exposure Bake

The most noticeable development progress in the post exposure bake step is technically improving uniform heat conduction between hot plates and exposed resist-coated wafers. Some research effort has been devoted to understanding the dependence of resist pattern qualities on hot plate PEB temperature and time.[23]

A rapid thermal anneal (RTA) furnace was explored to anneal exposed resists.[24] RTA is a common semiconductor manufacturing process which heats silicon wafers to precisely controlled high temperatures for a short period of time (1 second to several minutes). It is most often exploited to activate dopants, change morphologies of grown inorganic films, repair damage from ion implantation, densify deposited films, and so on. Since acid diffusion in chemically amplified resists is directly related to pattern resolution, optimizing PEB temperature and/or time is pivotal to controlling acid diffusion and thus enhancing pattern quality. RTA provides a platform to study the impact of subtle changes in PEB conditions on resist patterns.

An ultrafast annealing method, laser spike annealing, has been used to extend the study to a totally unexplored sub-millisecond time regime for PEB.[25] The topic and latest research findings will be discussed in Chapter 2.

1.3.3 Development

Aqueous base is most commonly used in the development process. Concerns with environmentally friendly lithographic processes, as evidenced by the establishment of NSF/SRC Engineering Research Center for Environmentally Benign Semiconductor Manufacturing, have directed research interest toward designing resist materials that can be cast from and/or developed with environmentally benign and recyclable fluids.

Water as Developer

Attempts were made to design chemical amplified resists that can be cast from and/or developed with pure water, which involved synthesis of water-soluble homo- and copolymers. Since water is a high surface tension solvent, no aqueous resist system has been reported to have high resolution.[42]

Hydrofluoroethers as Developer

Segregated hydrofluoroethers (HFEs), a type of fluorous solvents commercialized by 3M, have been investigated as a developer for specially designed chemically amplified resists for patterning delicate organic electronic materials to a scale of sub 100 nm.[26, 27] HFEs are proven as an environmentally friendly

developer because of their nonflammability, zero ozone-depletion potential and low toxicity for humans.[28] With their very low surface tensions, HFEs can promise high resolution and high aspect ratio patterns after development.

Thermal Development

Dry resist development techniques attract interest as they are expected to have a number of advantages over the prevalent wet development. Absence of hazardous solvents makes them environmentally friendly and potentially cheaper. In addition, dry development may avoid some of the notorious problems inherent to the traditional wet development such as resist swelling, increased line edge roughness, capillary-force driven resist collapse, and pattern detachment from the substrate.

Thermal development takes advantage of a dramatic volatility difference between unexposed and exposed resists. It has been successfully carried out on hot plates in air and low vacuum conditions. The development temperature should be chosen such that the resist should become volatile or degrade into volatile products rather than oxidizing and/or cross-linking and also resist melting or flow should be minimal. 25 nm half-pitch dense line/space patterns and 17 nm isolated lines with smaller line edge roughness were achieved in a thermally developed non-chemically amplified molecular glass resist [29], which demonstrates the feasibility of using thermal development for high-resolution lithography.

Supercritical Carbon Dioxide as Developer

As another approach to dry development, carbon dioxide in the supercritical state has been investigated as an environmentally friendly developer. Although CO_2 tends to be a very poor solvent for most polymers including current resists, certain fluoropolymers, silicones and molecular glass resists have been successfully developed soluble in CO_2 under moderate supercritical conditions. Chapter 3 will cover more on the topic and our contribution to this research area.

1.3.4 Characterization

Analysis of Resist Components

Chemically amplified resists are multi-component systems typically comprised of polymeric or molecular glass resist, photoacid generators (PAGs) and base additives/quenchers. The spacial distribution of these components within the spin coated thin film is critical to patterning nanoscale features in lithography. Resist thin films can exhibit surface segregation of PAGs that relies on the balance between PAG and resist chemistry.

Rutherford backscattering spectroscopy (RBS) was used to understand the miscibility of arsenic and sulfur containing PAGs as a function of photoresist chemistry [30] and to examine the diffusion and distribution characteristics of PAGs by examining heavy atoms [31]. X-ray photoelectron spectroscopy (XPS) was utilized to reveal the enrichment of perfluorooctanesulfonate of a variety of PAGs in the top few Angstroms of a resist film. Near-edge X-ray absorption fine

structure (NEXAFS) spectroscopy proves a solution to the limitation by providing a sensitive bond-selective and depth-selective method to quantify the PAGs depth profile over the top 2 - 6 nm.[33] The methodology can be extended to a diverse set of resist systems without the need for special labeling or preparatory procedures.

Compositional profiles can also be measured by neutron reflectometry, enabled by synthesizing a resist material with a deuterium-substituted protecting group for neutron scattering contrast.[35, 36] Because neutrons are scattered by nuclear interactions, there is a large difference in the neutron scattering cross section between deuterium and hydrogen nuclei, providing strong contrast with slight chemical modification. Therefore, spatial evolution of the deprotection reaction of deuterium-substituted protecting groups in the resist film is possible with neutron reflectometry measurement.

In addition to the aforementioned non-destructive techniques, the distribution of chemical compositions along the depth of a resist film can be probed through layer-by-layer removal of the film surface by sputtering under an ion beam.[34] Time-of-flight secondary-ion mass spectrometry (ToF-SIMS) uses a pulsed ion beam (Cs or microfocused Ga) to remove molecules from the very outermost surface of the sample. The ionized particles are removed from atomic monolayers on the surface (secondary ions) and then accelerated into a ”flight tube” and their mass is determined by measuring the exact time at which they reach the detector (i.e. time-of-flight).

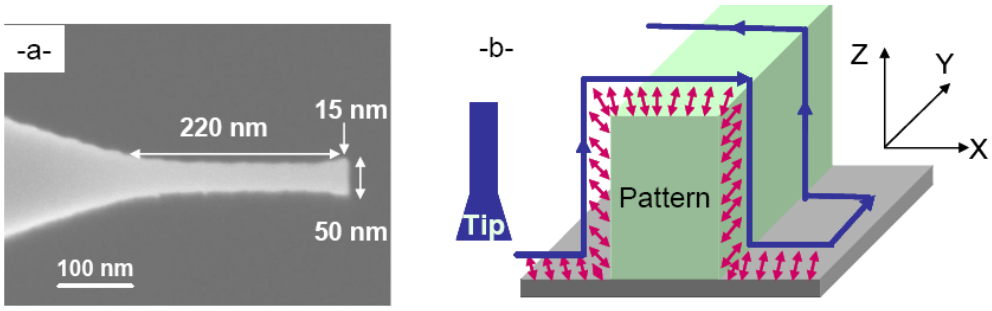

Figure 1.4: Basic principle of the 3D AFM technique: (a) the flared silicon tip used for the measurements (CDR50S model tip); (b) the CD-Mode scan principle.[38] Reproduced with permission from Reference [38]. Copyright 2007 Society of Photo Optical Instrumentation Engineers.

Analysis of Resist Patterns

The lithography community has been commonly using standard CD-SEM with conventional CD and LER algorithms for characterization of resist pattern quality and lithography process development. Some of the drawbacks of the technique include required sampling coating for high resolution imaging at high accelerating voltages of SEM and incorrect equipment parameters affecting edge roughness measurement.[37] Also, CD-SEM is mainly a top-down imaging tool so it is difficult to characterize the pattern sidewall roughness that contributes to the LER/LWR transferred to the underlayer after the etching step.

3D-AFM (three dimensional atomic force microscopy) has been developed to overcome the aforementioned disadvantages CD-SEM faces.[38] The AFM tip used is a specially designed flared silicon tip (Model CDR50S from Team Nanotec GmbH). Figure 1.4 shows the basic principles of the technique for 3D characterization of resist patterns. The immediate advantages are better sidewall resolution and thus better output accuracy and precision such as LER, LWR, CD and sidewall angle. Combining both CD-SEM and 3D-AFM techniques is

now strongly recommended for advance node development in order to have access to the best possible measurement accuracy.

1.4 Summary

This chapter has reviewed most of the conventional and unconventional processing and characterization methods in lithography. Unconventional methods have attracted increasing research interest because of their potential for patterning unusual structures, more environmentally friendly processing, and providing better understanding and control of resist performance.

The following chapters and the appendix are organized to demonstrate our efforts at unconventional exposure, post exposure bake, development, and characterization methods in lithography. Although they cover different aspects of lithography, a common theme running throughout is better understanding the properties of resist materials and tailoring them to expand the applications. Chapter 2 discusses laser spike annealing as an ultrafast post exposure bake method for chemically amplified resists. Chapter 3 details supercritical carbon dioxide as an environmentally friendly and sustainable solvent to develop high resolution resist patterns. An *in situ* FTIR method is discussed in chapter 4 as a technique to monitor reaction-diffusion kinetics of acids in chemically amplified molecular glass resists during post-exposure bake. Two-photon lithography is demonstrated in the appendix as a direct write technique to introduce three dimensional defects inside photonic materials.

CHAPTER 2

POST EXPOSURE BAKE BY CO_2 LASER SPIKE HEATING

Pattern formation in a chemically amplified photoresist requires a post exposure bake (PEB) to catalytically deprotect the polymer. Excessive diffusion of the photo- or electron-generated acid results in the loss of line edge definition, blurring of latent images, and changes in the line edge roughness. While post exposure bake of photon/electron-exposed resists is typically performed on a hot plate for tens of seconds to minutes, sub-millisecond PEB using a CO_2 laser-based scanned heating system is demonstrated in this chapter in an attempt to minimize excessive acid diffusion by drastically reducing the PEB time. Several polymer and photoacid generator resist systems have been studied under 500 μs laser spike heating in a range of powers (temperatures) for their thermal stabilities and lithographic performance compared to equivalent hot plate samples. A resist bilayer structure was used to quantify photoacid diffusion in resists and study its effect on line edge roughness by creating a well-defined step gradient of photoacids to mimic an ideal lithographic line-edge.

2.1 Ultrafast Post Exposure Bake

Chemically amplified resists (CARs) have been the workhorse in lithography for semiconductor device manufacturing over the past three decades because of their high sensitivity and excellent patterning performance. In 1982, Ito, Willson, and Fréchet proposed the concept of chemical amplification[6, 7, 8], where irradiation activates photoacid generators and the generated photoacids sub-

[1]Section 2.5 is reprinted with permission from J. Sha, B. Jung, M. O. Thompson, C. K. Ober, M. Chandhok, and T. R. Younkin, *J. Vac. Sci. Technol. B.*, Vol. 27, 3020 (2009). Copyright 2009 American Vacuum Society.

sequently catalyze numerous reactions in a resist film before being trapped or quenched. In CARs, acids must be mobile enough within the resist matrix to deprotect sufficient acid-labile protecting groups to achieve the solubility switch in the developing media, but excessive acid diffusion can lead to image blur and loss of resolution.[42, 43, 44] This chemistry occurs during the post-exposure bake, normally done on a hot plate at a temperature of 90 - 150 ^{o}C for 30 - 120 seconds. In this work, an alternative PEB approach involving higher temperatures for dramatically shorter times has been investigated. As both acid diffusion and deprotection are thermally activated processes, the relative rates will be impacted by the time/temperature profile of the PEB. Such high temperature short time PEB also impacts resist sensitivity and may ultimately help improve the line edge roughness (LER). To the degree LER depends on acid diffusion, improved utilization of the photogenerated acids in a smaller diffusion volume may result in reduced LER. To access very short PEB times, we have used a scanning laser heat source, referred to as laser spike annealing (LSA).

2.2 Laser Spike Annealing and Laser PEB

Laser spike annealing (LSA), also known as millisecond transient thermal annealing, has been developed and utilized in the semiconductor industry to address issues in front-end processing, particularly the need to activate impurity dopants while minimizing their diffusion for shallow junction formation.[45, 46] The dopant activation enthalpy is greater than the activation enthalpy for diffusion. Therefore, diffusion can be minimized by annealing at higher temperatures for increasingly short times. To achieve sub-millisecond thermal cycles, a line focused continuous wave (CW) laser is scanned over the surface, heating

the surface to a controlled temperature (up to 1400 °C) in time scales of 0.2 - 5 ms and cooling in a similar time by thermal conduction into the cold substrate.

A CW CO_2 laser at λ = 10.6 μm was used for this work with a dwell time of 500 μs, where dwell is defined as laser beam full width at half maximum (FWHM) divided by the scan velocity. In Figure 2.1(a), a simulation of the surface temperature as a function of time is shown for typical conditions (500 μs dwell, 260 W/cm) resulting in a peak temperature of 195 °C. In contrast to hot plate annealing, the temperature is never entirely isothermal but remains within 20 °C of the peak for approximately 270 μs. Within 5 ms, the surface cools and returns to essentially the initial substrate temperature. Simulations were used to estimate peak temperatures as a function of the CO_2 laser power at a dwell time of 500 μs as shown in Figure 2.1(b). To achieve equal temperatures, the power must be decreased as the dwell increases. Simulated temperatures were calibrated with actual experimental conditions using the melting temperature of pure silicon. However, as temperatures are estimated from the simulation, data hereafter are presented as actual laser powers (W) along with the estimated maximum temperatures. For the measured beam profile, the value of the linear power density (W/cm) is approximately 10 times the absolute laser power in watts.

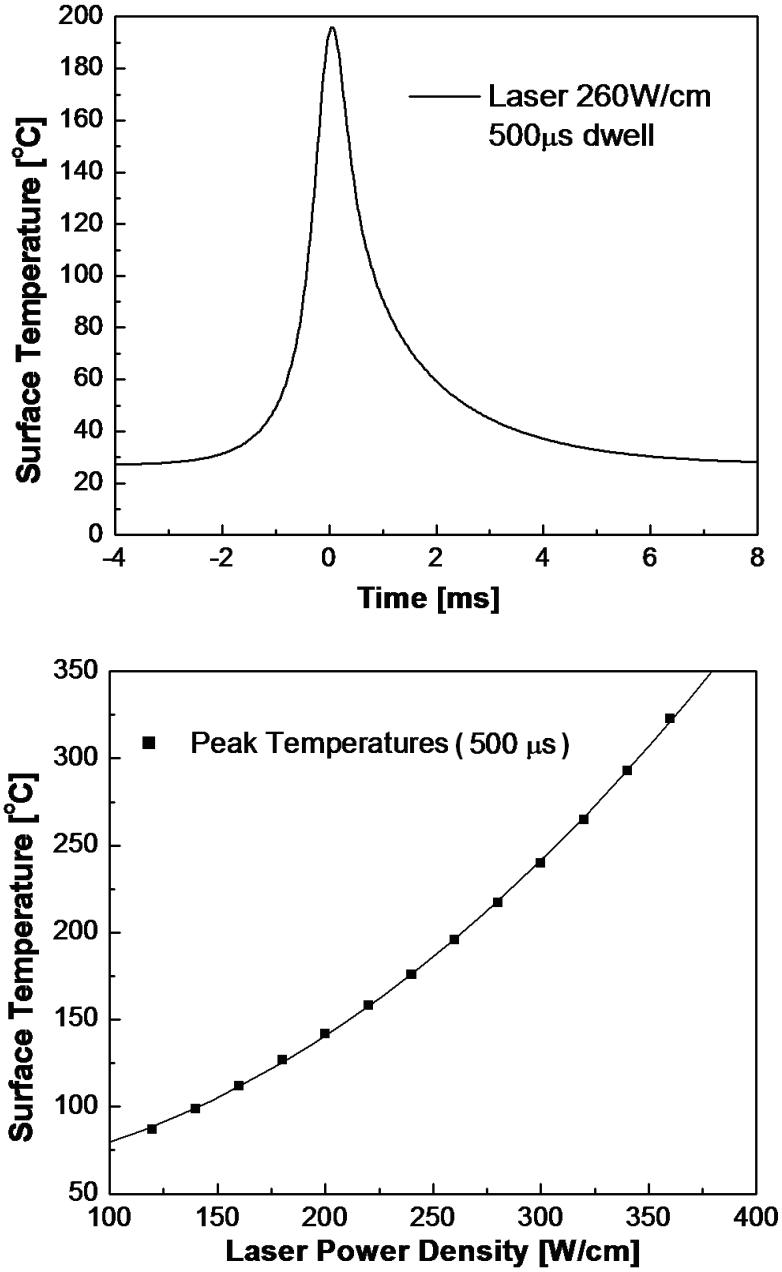

Figure 2.1: Simulated surface temperature of a heavily doped silicon substrate as a function of time (upper) and as a function of CO_2 laser power density (bottom) at 500 μs dwell time. As shown in the upper plot, the peak temperature is not entirely isothermal but remains within 20 ^{o}C for approximately 300 μs.

2.3 Experimental

2.3.1 Materials

Two resist copolymers and three photoacid generators (PAGs) were used in this study to make several resist formulations (Fig. 2.2). Poly(hydroxystyrene-co-styrene-co-tert-butylacrylate) (**ESCAP**) (glass transition temperature: ~147°C), with a number average molecular weight (Mn) = 13,100 g/mol, polydispersity (Mw/Mn) = 2.06, and 59.3/15.7/25 composition by mole, was obtained from DuPont Electronic Materials. Poly(methyladamantane methacrylate-co-α-methacryloxy-γ-butyrolactone) (**P(MAdMA-co-GBLMA)** or **193resist** for short) (molar ratio: 43.5/56.5, glass transition temperature: ~157°C) was kindly provided by Mitsubishi Rayon America Inc. Triarylsulfonium hexafluoroantimonate salts (50 wt.% in propylene carbonate) (**THS**), triphenylsulfonium perfluoro-1-butanesufonate (**TPS-Nf**), N-hydroxynaphthalimide triflate (**NI-Tf**), coumarin 6, poly(hydroxystyrene) (**PHOST**), and hexamethyldisilazane (**HMDS**) were used as received from Sigma-Aldrich. Finally, a formulated and commercially available photoresist TOK-EUVR P1123 ME was kindly provided by TOK America.

2.3.2 Sample Preparation and Exposure

Single layers of photoresist were spin-cast onto HMDS-primed heavily doped silicon wafers (4" P/BOR ⟨100⟩ 0.01-0.02 Ωcm, 500-550 μm SSP) from 5 wt.% solutions of propylene glycol methyl ether acetate (PGMEA) with 5 wt.% (with respect to resist copolymers) loading of PAGs. After spin casting, a post apply

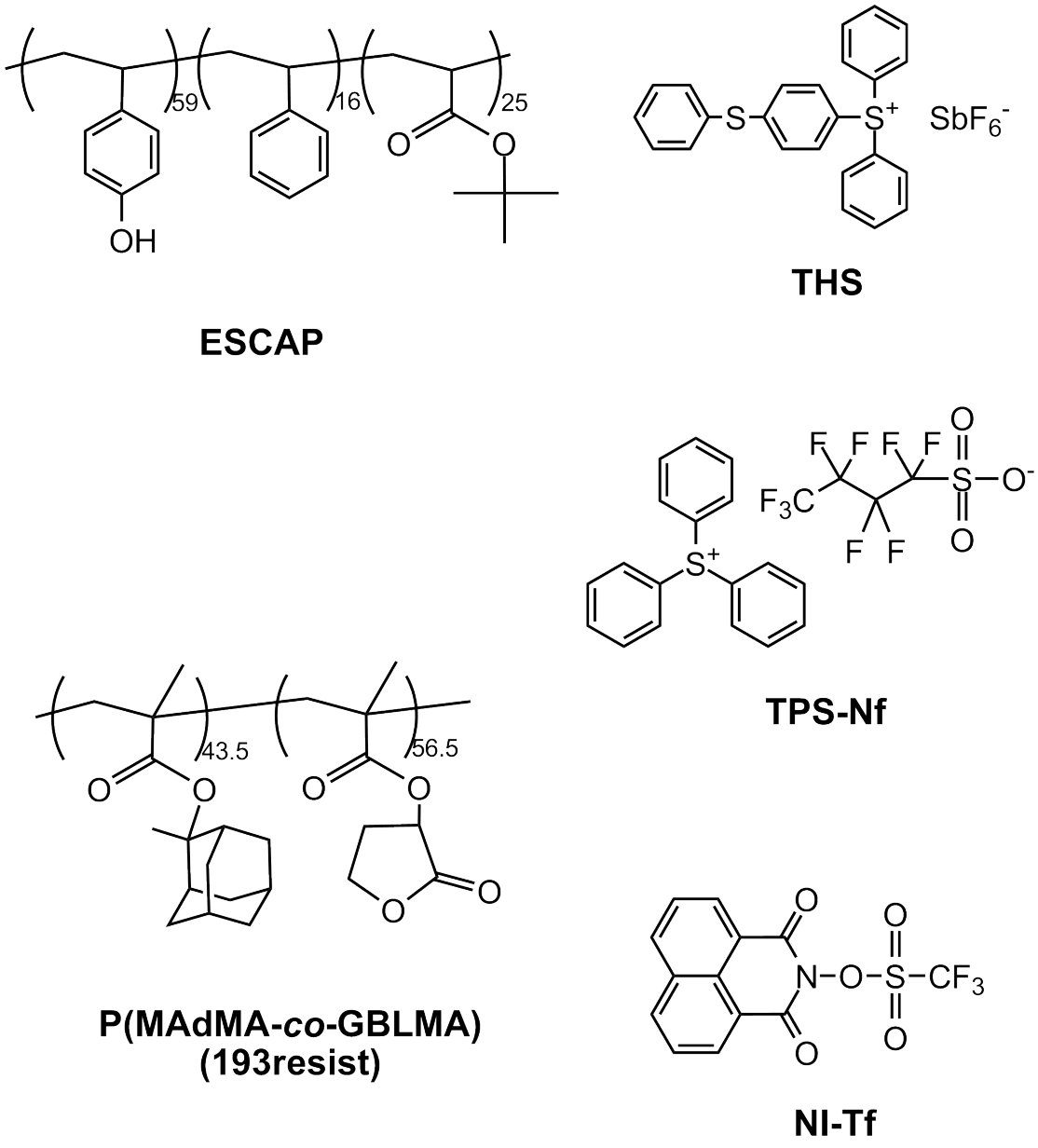

Figure 2.2: Chemical structures of resist copolymers and photoacid generators used in the experiments.

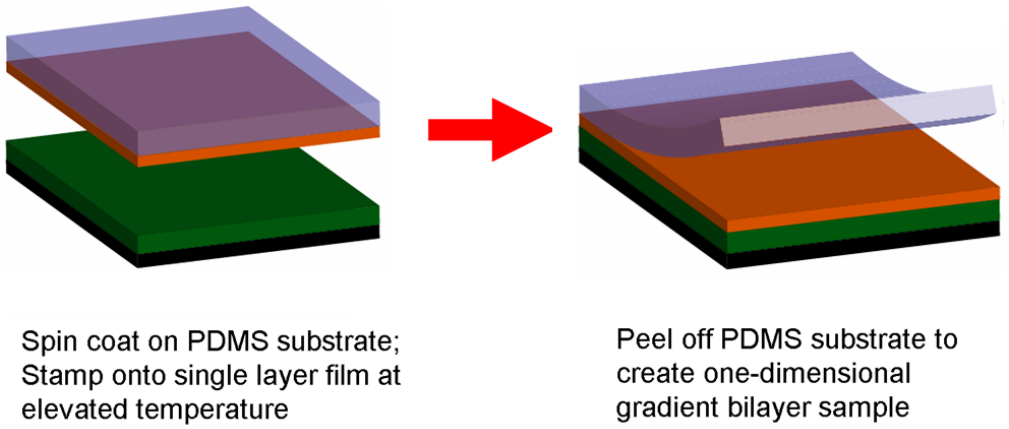

Figure 2.3: Bilayer sample preparation using the PDMS stamping technique.

bake (PAB) was performed at 130 °C for 60 sec to evaporate the spinning solvent.

A PDMS stamping technique was used to create bilayer samples with PAG-loaded resist films at the top and PAG-free films at the bottom (Fig. 2.3).[39] The bottom layers of bilayer samples were prepared on HMDS-primed heavily doped silicon wafers from PAG-free solutions in the same way as single layer samples. Resist solutions containing PAG were spin-cast on PDMS substrates and then stamped onto prepared PAG-free resist films at 90 °C for 20 sec. PDMS stamps were peeled off after the stacks cooled down to room temperature. The resist bilayers were baked again at 115 °C for 60 sec to remove any residual spinning solvent. A typical bottom layer was about 100 nm thick while a top layer was measured to be between 50 and 60 nm thick.

DUV exposure was carried out for varying times using an HTG (Hybrid Technology Group) System III-HR contact/proximity mask aligner at wavelengths of 235-260 nm (measured power 2.5 mW/cm^2 at 254 nm) or 405 nm (measured power 20 mW/cm^2) or an ABM high resolution mask aligner at 254 nm (measured power ~6 mW/cm^2). DUV flood exposure was conducted on sin-

gle photoresist layers for contrast curves and all bilayer samples while a quartz mask was used for patterning of single layers. Electron beam patterning was performed using a Leica VB6 operating at 100 kV. EUV exposure at 13.5 nm was performed at the Lawrence Berkeley National Laboratory (LBNL) Advanced Light Source (ALS) or an EUV ROX system at SEMATECH (Albany, NY).

2.3.3 Post-Exposure Baking and Development

After DUV exposure, the photoresist films were baked using either a hotplate (115 ^{o}C/60 s or 30-380 ^{o}C/15-120 s) or the CO_2 based LSA system. The LSA system consists of a CO_2 laser, a He-Ne laser (for collimation and marking of optical path), a beam splitter, shutters, focus lenses, and reflecting mirrors. A schematic and some photos of the setup are shown in Fig. 2.4 and Fig. 2.5 respectively. The CO_2 laser (λ = 10.6 μm) provides up to 110 W of power in a focused beam 140 $\times$ 1000 μm^2 on the wafer surface. Samples are scanned under the beam at a dwell time of 500 μs. The laser beam is stepped 109 μm between scans to fully anneal the irradiated area. The CO_2 laser power is adjusted to control the peak temperatures. For precision, however, laser power is mainly used in discussions, sometimes along with a simulated temperature for reference.

An aqueous solution of tetramethylammonium hydroxide (TMAH 0.26 N; AZ 300 MIF) was purchased from AZ Electronic Materials USA Corp. and used as received. All the exposed photoresist films were developed in 0.26 N TMAH for 60 seconds, rinsed with de-ionized water, and blown dry with nitrogen.

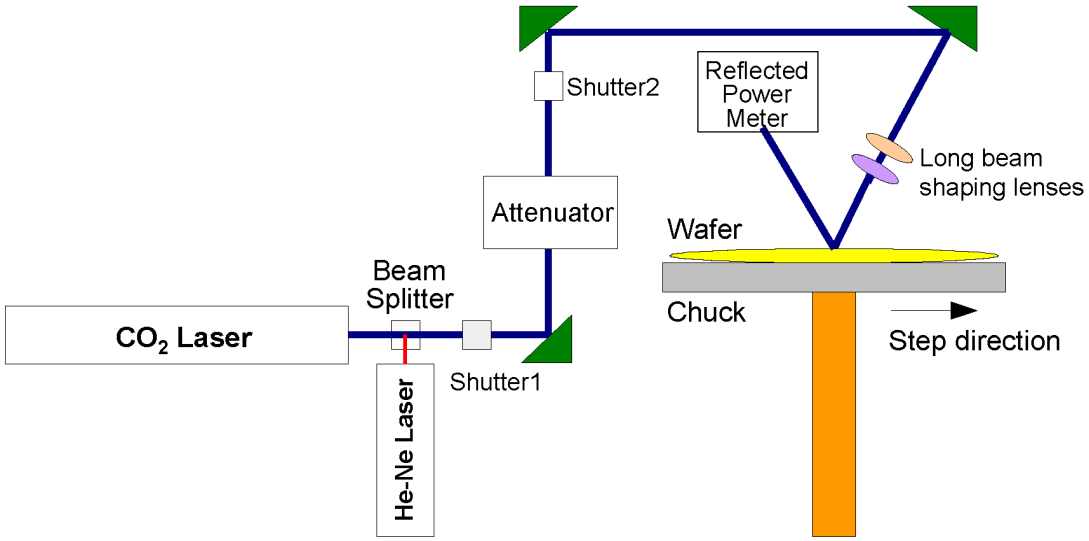

Figure 2.4: A schematic of the laser annealing PEB system setup.

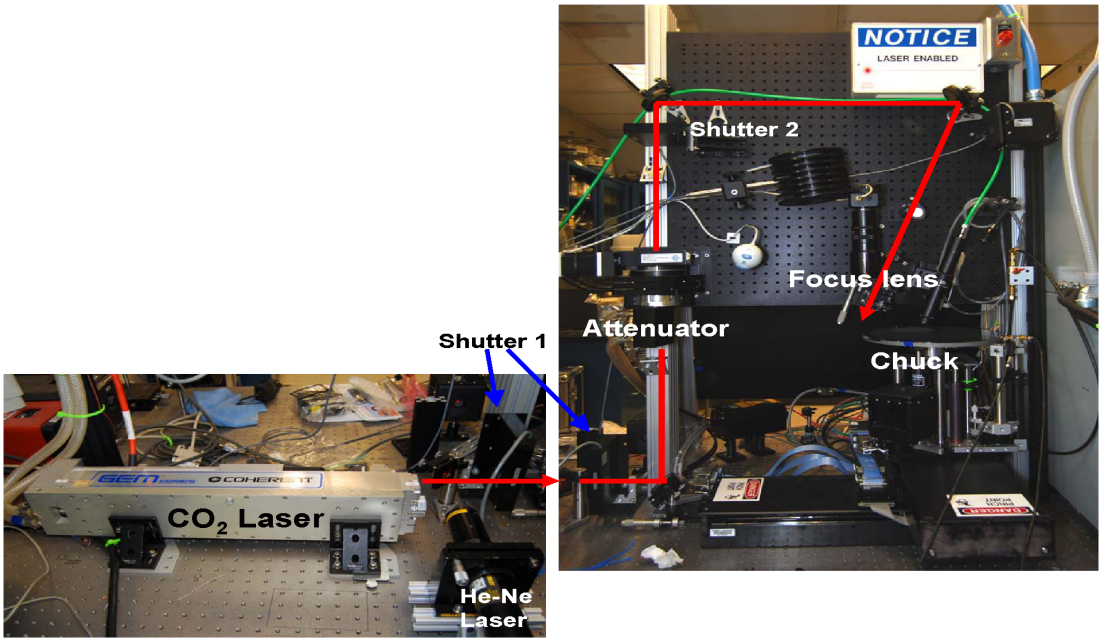

Figure 2.5: Photos of the laser annealing system setup.

2.3.4 Characterization

Film thickness was measured using a FilmMetrics film measurement system. Optical microscopy images were taken on an Olympus BX60/U-CFU microscope. A LEO 1550 FESEM was used for scanning electron microscopy on high resolution patterns. Atomic force microscopy (AFM) was performed on developed bilayer samples with a Veeco Dimension 3100 in tapping mode.

2.4 Thermal Stability of Photoresist Components

Thermal stability of several polymer and photoacid generator (PAG) resist systems were studied under 500 μs laser spike annealing. All the resist systems exhibited remarkable stability in this temperature/time regime, with the maximum useful temperature limited by thermal deprotection and/or decomposition of the polymer backbone.

Resist polymers ESCAP and P(MAdMA-co-GBLMA) with and without PAG TPS-Nf were annealed at varying laser powers (temperatures) to test their thermal stability. Figure 2.6 shows the film thickness of post-annealed polymer films before and after developing in 0.26 N TMAH for 60 sec. For example, for ESCAP and ESCAP/TPS-Nf, laser powers above ~ 55 W removed the films entirely, with partial thickness loss for powers above 40 W. Partial film loss after development was observed between 35 and 40 W. The P(MAdMA-co-GBLMA) resist systems behaved qualitatively the same. We believe that thermal decomposition of polymer backbone occurred at the highest powers (temperatures) with thermal deprotection of protecting groups occurring in the intermediate

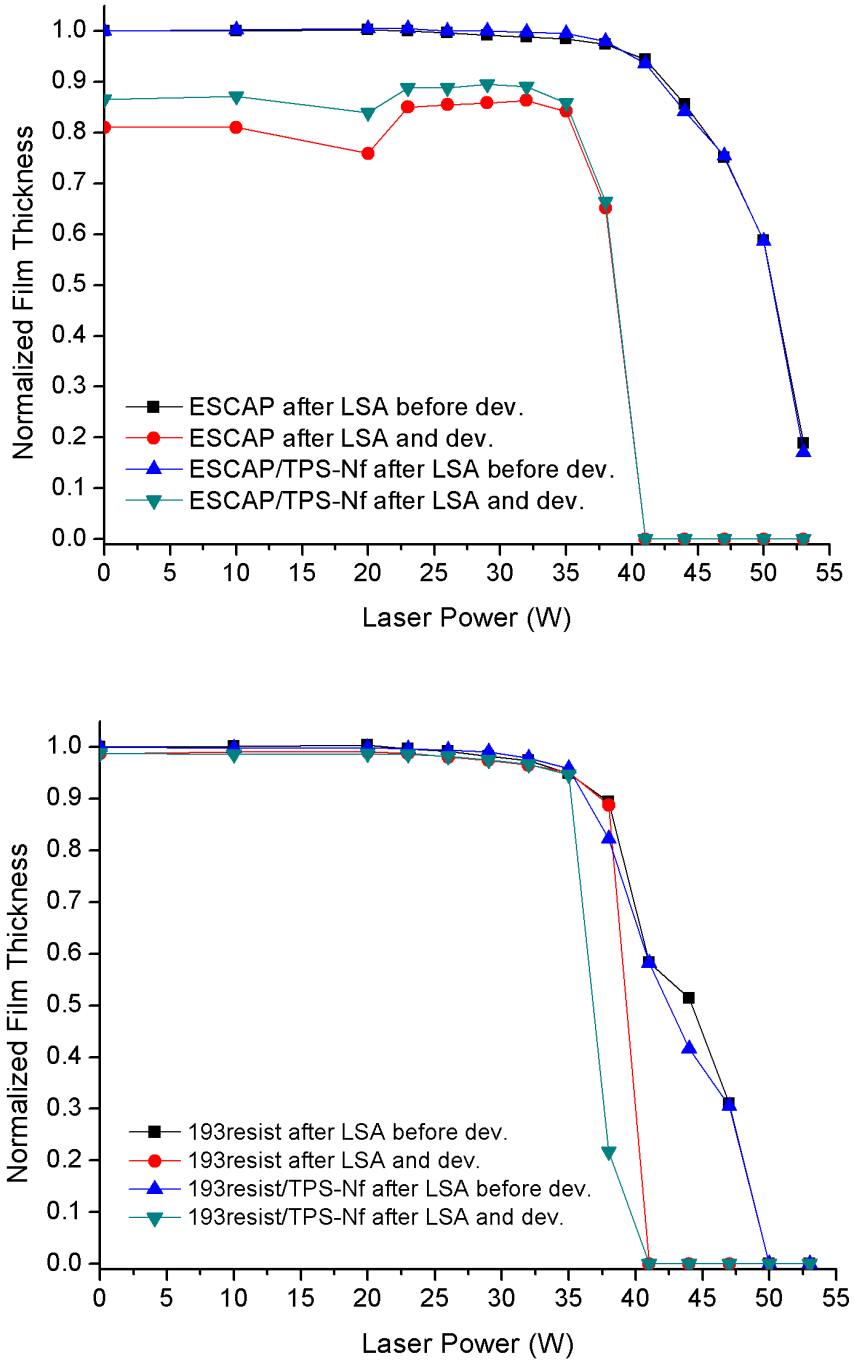

Figure 2.6: Thickness of ESCAP vs. ESCAP/TPS-Nf films (upper) and P(MAdMA-co-GBLMA) vs. P(MAdMA-co-GBLMA)/TPS-Nf films (bottom) under CO_2 laser PEB at different powers, before and after developing in 0.26 N TMAH for 60 sec.

temperatures. From Figure 2.1, the critical critical temperature for resist loss by thermal deprotection is ≈ 400 °C. The resist itself can survive to temperatures on the order of 500 °C, a direct result of sub-millisecond time scales involved. For ESCAP, a significant temperature difference exists between thermal deprotection and resist decomposition, while both occur at approximately the same temperature with the P(MAdMA-co-GBLMA) resist. As no difference is noted between PAG containing and PAG free films, we also conclude that the PAG was stable to the highest temperatures used. Between ~ 20 and 35 W, the ESCAP film loss after development was less than that observed below 20 W, indicating that LSA hindered dissolution of ESCAP at moderate powers (temperatures). This may be the result of further removal of residual solvents from the ESCAP films during laser heating at moderate temperatures. Loss of the solvents would result in less free volume (closer packing of molecules) in the polymers and thus a reduced dissolution rate in TMAH. From these stability studies, the appropriate PEB processing condition for both P(MAdMA-co-GBLMA) and ESCAP must be below 35 - 40 W.

For comparison, Figure 2.7 shows film thickness of ESCAP (without PAG) annealed on a hot plate for 15, 60, and 120 sec at different temperatures. The temperature required for full film removal after development ranges from 200 to 250 °C for 15 - 120 seconds. This is consistent with the estimated temperatures under LSA given the much longer time scales.

With regard to other aspects of laser annealed resist films, at moderate laser powers (below 35 W), the resists could be readily stripped; at higher powers, some residuals were observed, indicating some thermally induced decomposition. Etch resistance of laser annealed resist films was investigated after de-

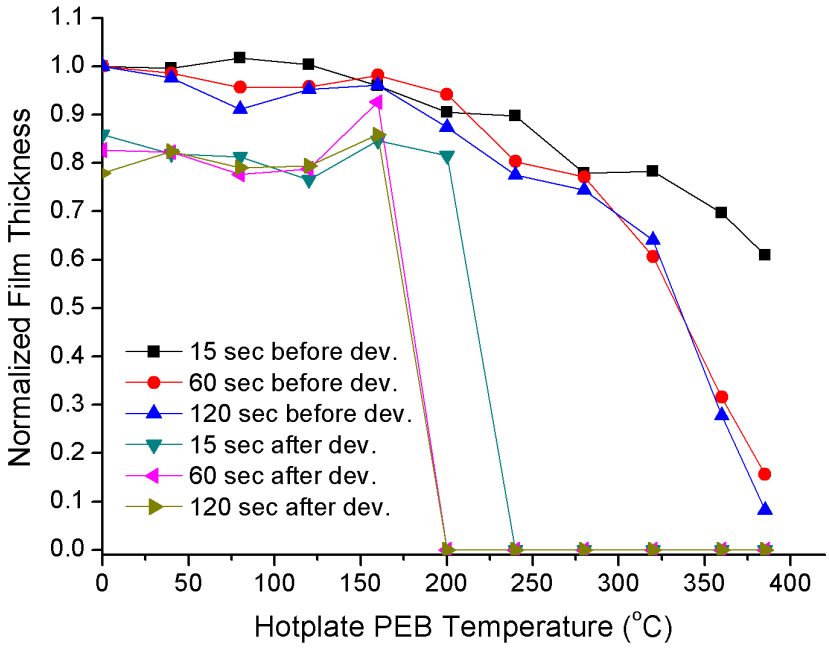

Figure 2.7: Film thickness of ESCAP (without PAG) annealed on a hot plate for 15, 60, and 120 sec at different temperatures.

velopment of the films in 0.26 N TMAH. Figure 2.8 shows that there was no significant change in etch resistance between unannealed (0 W) and annealed (up to ~ 35 W) photoresist films for both CHF_3(50 sccm)/O_2(2 sccm) and CF_4(30 sccm) etch, which confirms the preservation of the chemical integrity of the resists after laser annealing.

Thermal or IR induced decomposition of PAGs was investigated by adding an acid sensitive dye indicator coumarin 6 (C6) to PHOST/PAG solutions. PHOST was selected as the polymer matrix because it lacks acid-labile protecting groups and thus no additional hydroxyl groups result from thermal deprotection during PEB. Hydroxyl groups are known to ”trap” photoacids via hydrogen bonding. Photoacids generated through PAG decomposition react with C6 molecule (strong light absorption at 470 nm) to form a protonated coumarin

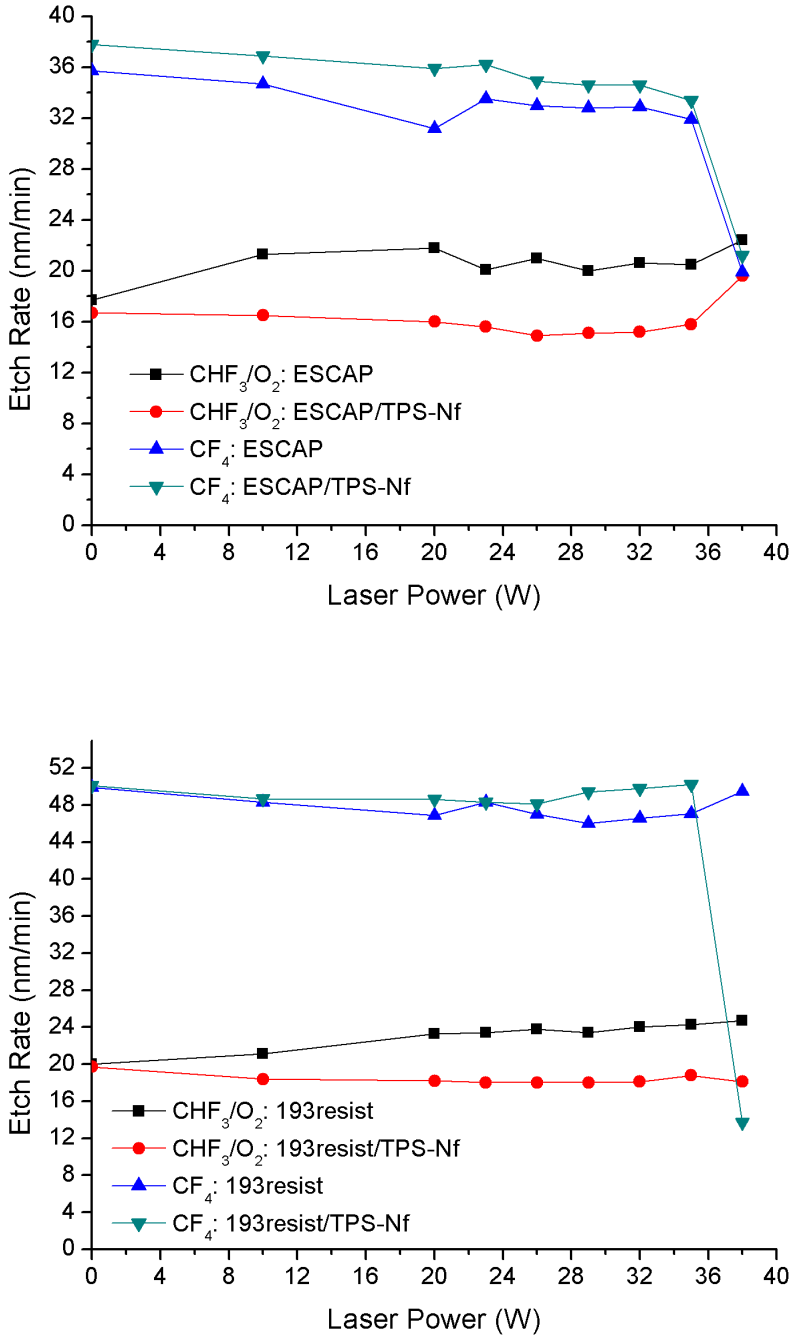

Figure 2.8: Etch rates of laser post exposure baked ESCAP (upper) and P(MAdMA-co-GBLMA) (bottom) resist films.

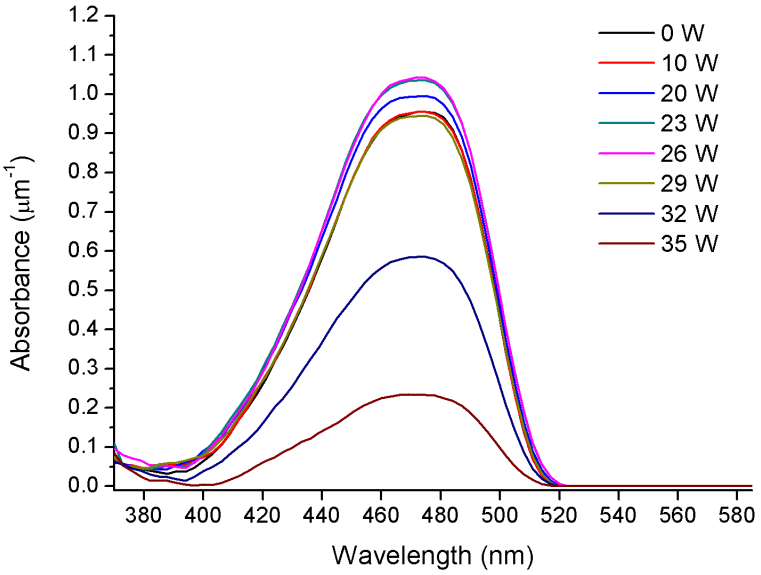

(a) Absorbance spectra of annealed PHOST/C6

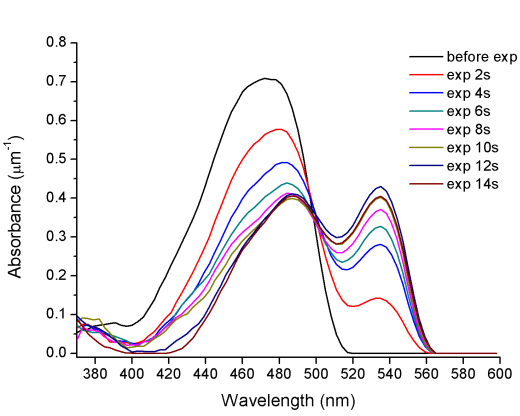

(b) Absorbance spectra of PHOST/TPS-Nf/C6

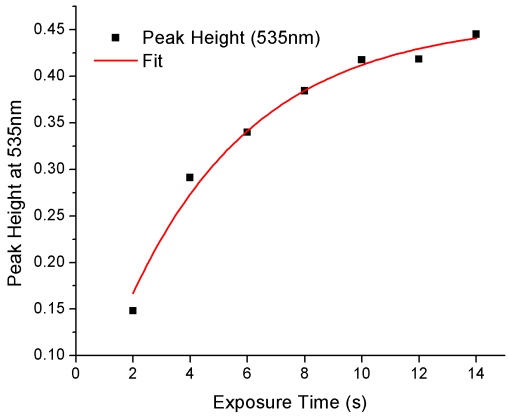

(c) Absorbance peak height vs. exposure time

Figure 2.9: Demonstration of using C6 as an acid indicator in PHOST/PAG films. (a) Absorbance spectra of PHOST/C6 annealed at laser powers varying from 0 to 35 W. (b) Absorbance spectra of PHOST/TPS-Nf/C6 exposed at DUV for 2 - 14 sec. (c) Fitting absorbance peak height data of $C6^{+}$ versus exposure time.

($C6^+$) which shows an absorption peak at 535 nm in PHOST films. The complex refractive indices of each film were used to calculate the $C6^+$ absorbance (α_{C6^+}) according to the equation $\alpha_{C6^+} = 4\pi k(\lambda)/\lambda$ where k is the imaginary part of the refractive index and λ is the corresponding wavelength.

Stability of C6 in a PHOST film under laser heating was first tested with the results shown in Figure 2.9(a). The absorbance spectra of a PHOST/C6 film do not show much difference from 0 W to approximately 29 W while the absorbance peak height decreases as laser power increases above 30 W, which may indicate thermal decomposition of C6 molecules. Therefore, C6 can work properly as an acid indicator for laser PEB below ≈ 30 W (≈ 250 °C).

As a proof of the validity of the methodology, Figure 2.9(b) displays the absorbance peak height of a PHOST/TPS-Nf/C6 film as a function of exposure time (dose) with no PEB. The absorbance peak height is plotted against exposure time in Figure 2.9(c) and increases as expected with exposure dose. The curve was fit using a relation $y = a \cdot (1 - e^{-b \cdot x})$ based on the Dill equation $H = [PAG] \cdot (1 - e^{-C \cdot E})$.

Films of PHOST/C6 formulated with three different PAGs (TPS-Nf, THS, and NI-Tf) were prepared, exposed to laser PEB, and tested for the thermal stability of the PAGs. The absorption spectra of the films annealed at laser powers up to 35 W are shown in Figure 2.10. No absorption peak at 535 nm was observed in films containing the two ionic PAGs (TPS-Nf and THS) while the film containing the non-ionic PAG NI-Tf shows a small peak at 535 nm in the absorption spectra at and above 20 W indicating existence of acids from thermally decomposed NI-Tf. In summary, TPS-Nf and THS are thermally more stable than NI-Tf at powers above 20 W.

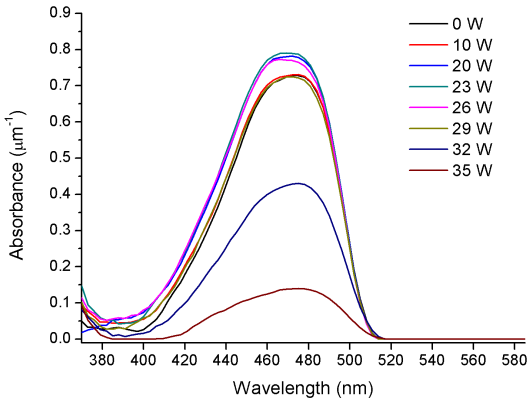

(a) Absorbance spectra of PHOST/C6/TPS-Nf

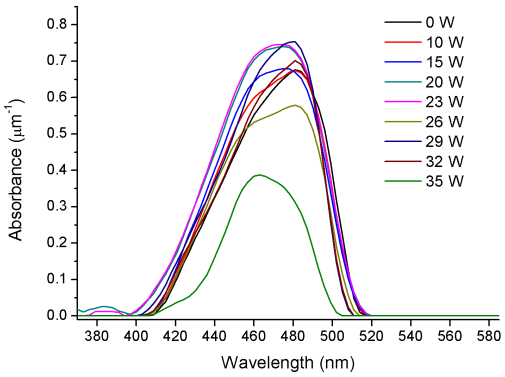

(b) Absorbance spectra of PHOST/C6/THS

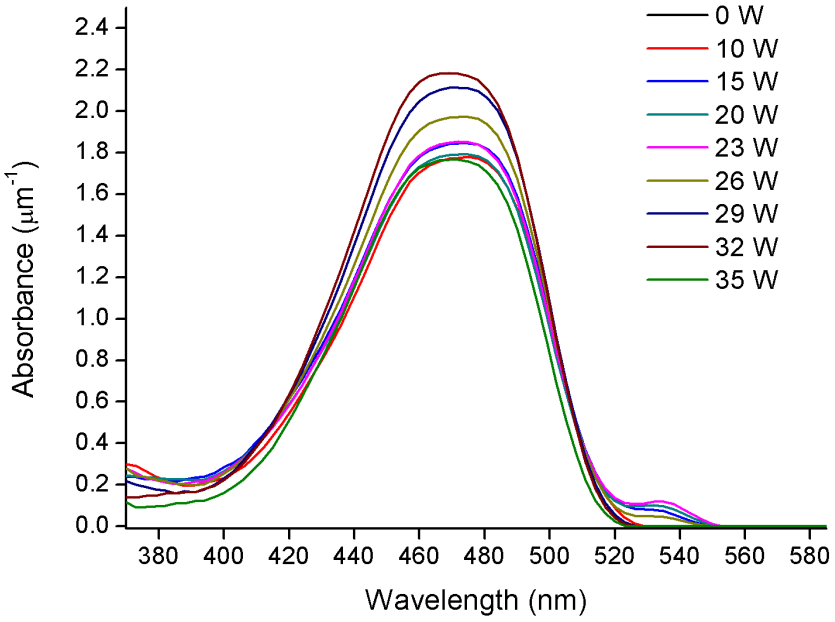

(c) Absorbance spectra of PHOST/C6/NI-Tf

Figure 2.10: Thermal stability of three PAGs under laser annealing. Absorbance spectra of annealed films of PHOST, C6 and a PAG: (a) TPS-Nf, (b) THS, (c) NI-Tf.

2.5 Resist Sensitivity Change Under Laser PEB

The sensitivities (dose-to-clear) of several resist systems were compared under laser PEB and conventional hot plate PEB. Data for the P(MAdMA-co-GBLMA)/NI-Tf resist are illustrated in Figure 2.11 as an example. Under deep ultraviolet (DUV) (235-260 nm) exposure on HTG contact aligner, this resist system showed a more than 2.5 times sensitivity enhancement with laser PEB above 33 W. Micron line patterns of comparable quality were obtained at only 40% of the exposure dose for laser PEB compared to hot plate PEB. A similar trend was observed for 405 nm exposure with sensitivity enhancements up to 5 times.

A quantitative comparison of E_0 (dose-to-clear) of laser PEB and hot plate PEB is summarized in Figure 2.12. Although all of the resist systems behaved similarly, there were some interesting differences. For all but the ESCAP/NI-Tf system under DUV exposure, the sensitivity improved with increasing laser power (temperature). P(MAdMA-co-GBLMA)/NI-Tf showed the strongest sensitivity to temperature, while ESCAP/THS showed a consistent weak dependence. ESCAP/NI-Tf showed lowered sensitivity under DUV irradiation but improved sensitivity under 405 nm illumination. The temperature sensitivity is associated with thermal activation of PAGs and the activation energies for deprotection, while the origin of the wavelength dependence remains unclear at the moment.

The sensitivity enhancement may also be linked to transient trapping and/or quenching of photogenerated acids. The thermal ramp of laser PEB is extremely high (10^6 K/s compared to < 100 K/s for hot plates) and may be as important

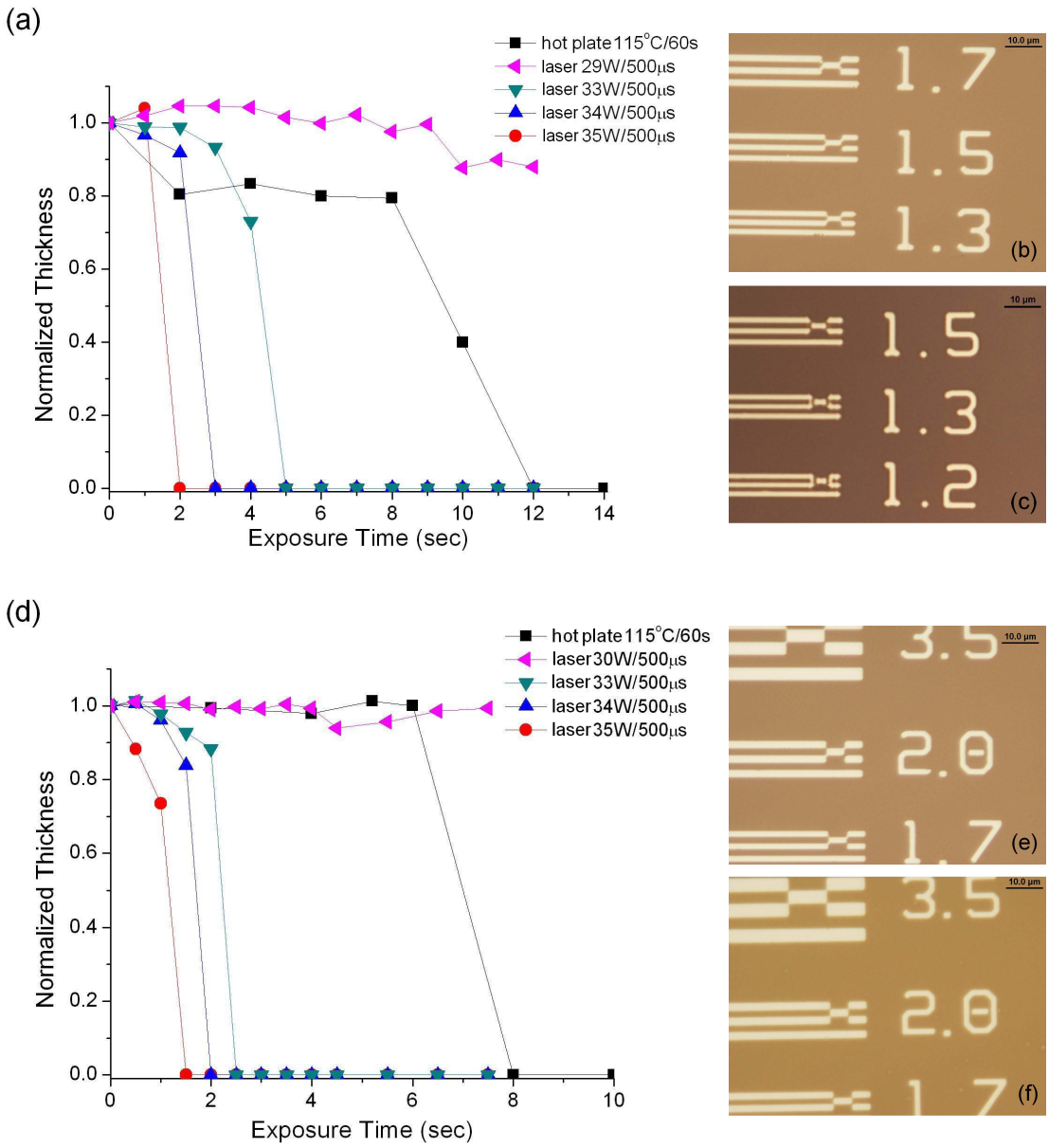

Figure 2.11: Contrast curves (a)(d) of the P(MAdMA-co-GBLMA)/NI-Tf resist system and optical microscopy images of patterned resist films of hot plate [(b) and (e), dose was 14.0 and 10.5 mJ/cm^2 respectively] and laser PEB [(c) and (f), dose was 6.0 and 3.4 mJ/cm^2 respectively]. DUV (235-260 nm) exposure (a)-(c); 405 nm exposure (d)-(f).

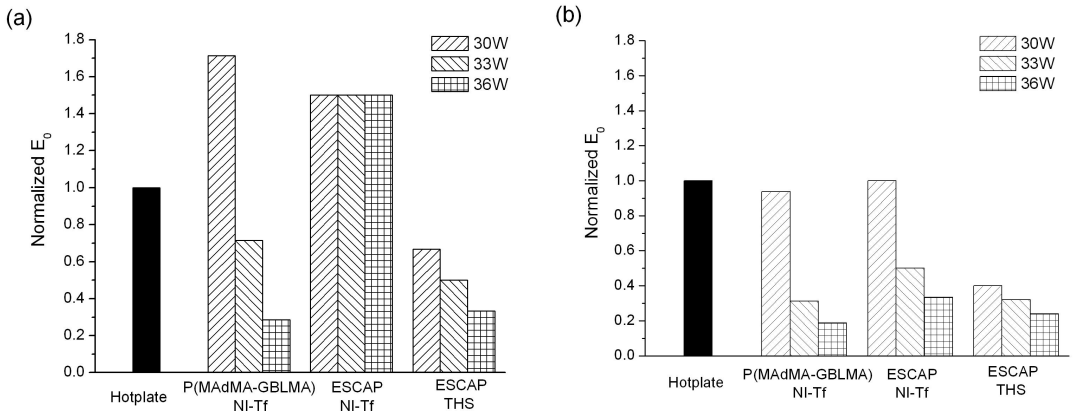

Figure 2.12: Comparison of E_0 for the resist systems of hot plate and laser PEB at 30, 33, and 36 W under (a) DUV (235-260 nm) and (b) 405 nm exposure.

as peak temperature. PEB on a hot plate may allow limited use of the photoacid before being trapped at quench sites formed upon exposure, while laser PEB can provide sufficient PEB temperature to continually break the trap/quench site and enable continued deprotection.

In contrast, the commercially available TOK-EUVR P1123 ME resist was also tested at DUV exposure wavelengths. Over a wide range of laser PEB conditions, the dose-to-clear showed only small changes and generally slightly less sensitivity than the hot plate PEB (Fig. 2.13).

In this section, we discussed the difference in resist sensitivity when using sub-millisecond laser PEB versus minute scale hot plate PEB. Under DUV exposure at 235-260 nm, up to 3.5 times sensitivity enhancement was achieved for P(MAdMA-co-GBLMA)/NI-Tf resist system, 0.67 times for ESCAP/NI-Tf and 3 times for ESCAP/THS. Under 405 nm exposure, up to 5.3 times sensitivity enhancement was achieved for P(MAdMA-co-GBLMA)/NI-Tf resist system, 3 times for ESCAP/NI-Tf and 4.2 times for ESCAP/THS. Comparable imaging capabilities were observed.

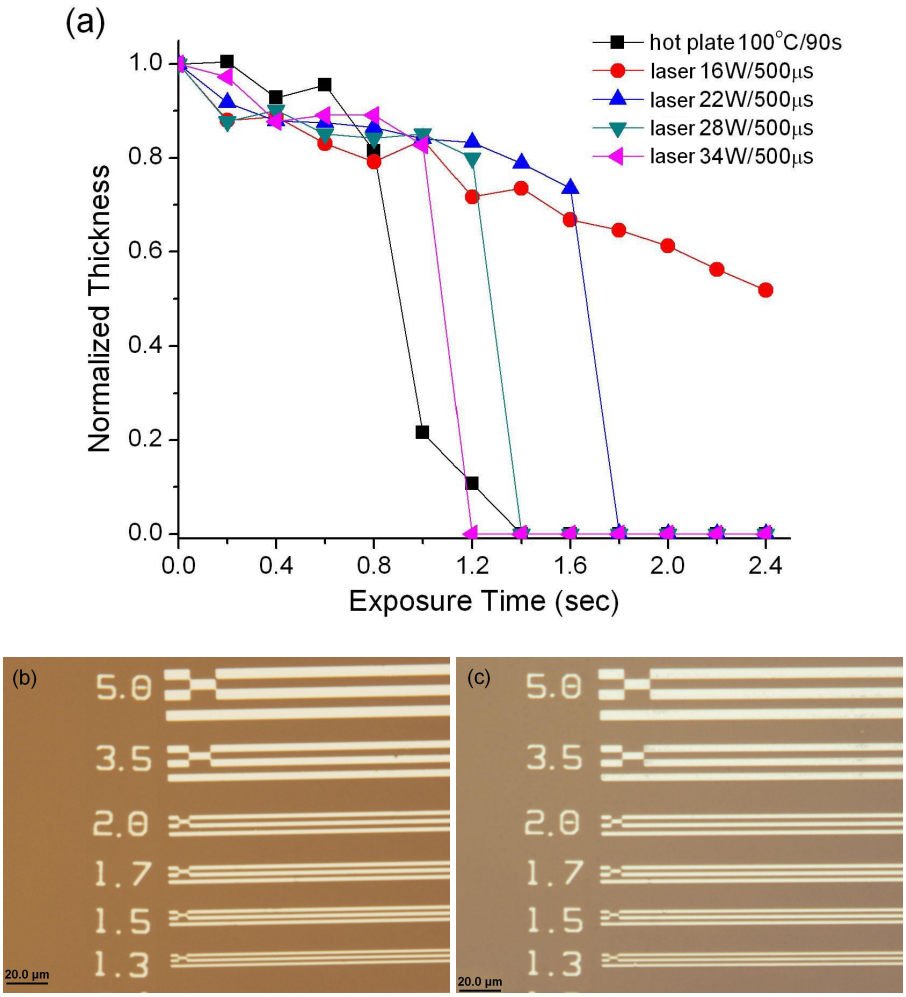

Figure 2.13: Contrast curves of (a) TOK-EUVR P1123 ME resist and optical microscopy images of patterned resist films of (b) hot plate and (c) laser PEB under DUV (235-260 nm) exposure.

2.6 High Resolution Patterning

To assess the potential for high resolution patterns with laser PEB, electron-beam lithography was used to pattern the TOK-EUVR P1123 ME resist. Figure 2.14 shows SEM images of 80 nm 1:1 line/space patterns annealed by hot plate (100 °C, 90 sec; e-beam dose = 17.4 μC/cm^2) and laser PEB (31 W, 500 μs; e-beam dose = 43.1 μC/cm^2). Line edges of the laser sample clearly demonstrate less

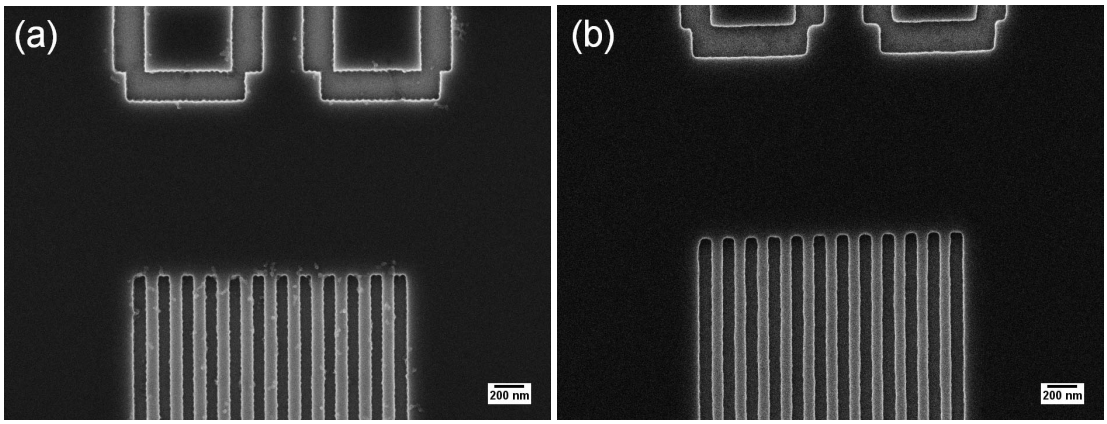

Figure 2.14: SEM images of electron-beam patterned TOK-EUVR P1123 ME resist with (a) hot plate and (b) laser PEB.

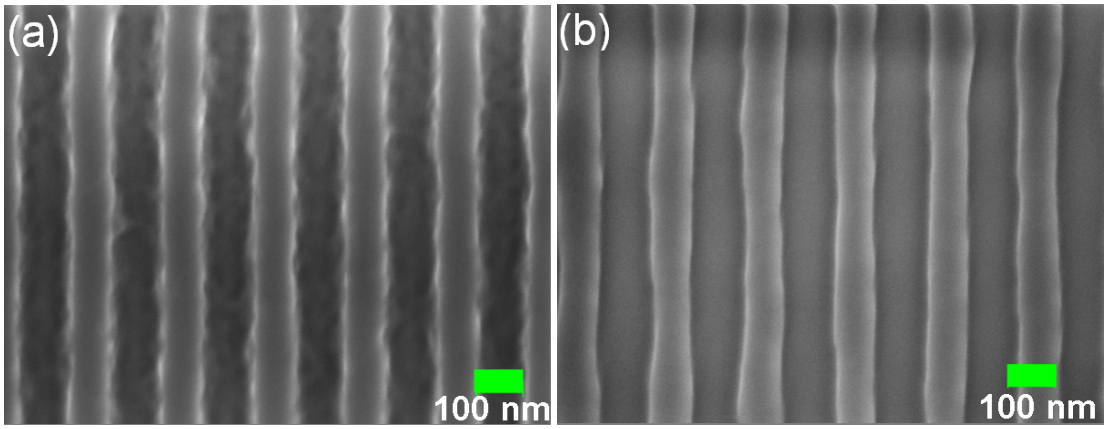

Figure 2.15: SEM images of EUV patterned P(MAdMA-co-GBLMA)/THS resist with (a) hot plate and (b) laser PEB.

roughness than the hot plate sample.

While comparable patterning resolution was observed, the dose required more than doubled from the hot plate to laser PEB. The mechanism for this loss of sensitivity under e-beam exposure is not clear at this time. It is possible that damage from the energetic electron beam may result in additional trap/quench in sites that remain active under the fast thermal ramp of laser PEB.

EUV exposure at 13.5 nm was conducted on P(MAdMA-co-GBLMA)/THS films at the Lawrence Berkeley National Laboratory (LBNL) Advanced Light Source (ALS). Figure 2.15 shows SEM images of 100 nm half-pitch lines for both laser PEB (22 W, 500 μs) and hot plate (115 ^{o}C, 60 sec) PEB. While the resolutions are comparable, the photoresist line edges are smoother on the laser PEB sample (dose = 3.86 mJ/cm^2) compared to the hot plate one (dose = 9.04 mJ/cm^2). An enhanced sensitivity was observed with laser PEB under EUV exposure just as under longer wavelength photon irradiations, which implies that the different mechanisms of electron-beam and photon exposures may be the reason for the divergence in resist sensitivity change.

2.7 Characterization of Acid Diffusion by Resist Bilayers

As patterning feature sizes move toward 22 nm and beyond, the challenge to simultaneously reduce exposure dose, feature critical dimension (CD), and line edge roughness (LER) has been attacked experimentally and theoretically. The tri-lateral challenge of resolution, dose, and LER suggests only two of these metrics may be met simultaneously at the sacrifice of the third.[128]

To quantify photoacid diffusion in resists and study its effect on CD and LER, an approach of creating a resist bilayer structure with PAG loaded just in the top layer was proposed to mimic an ideal lithographic line-edge that forms a well-defined step gradient of photoacids after flood light exposure.[39] After exposure and PEB, the samples were developed so that acid diffusion from the top PAG-loaded layer to the bottom PAG-free layer could be indirectly measured by the film thickness loss (due to acid-catalyzed deprotection) in the bottom layer

and the surface roughness of the bottom layer could be quantified by AFM to correlate with LER in real lithographic patterning. Our goal here is to compare hot plate PEB with laser PEB in terms of how photoacids generated upon irradiation diffuse in resists during the heating step.

The bilayer experiments were first carried out using an EUV (wavelength = 13.5 nm) irradiation source on an EUV ROX system at SEMATECH (Albany, NY). The samples consisted of a PAG(THS)-loaded P(MAdMA-co-GBLMA)(**193resist** for short in this section) layer at the top and a PAG-free 193resist layer at the bottom. After EUV exposure, the samples were annealed with laser from 18 to 30 W at a dwell time of 500 μs. Subsequently, the samples were developed in 0.26 N TMAH for 60 sec and rinsed with de-ionized water. Film thickness was measured on a FilMetrics. Figure 2.16(a) plots post-development film thickness against EUV exposure dose. The horizonal line at around $y = 0.55$ marks the interface between the top PAG-loaded layer and the bottom PAG-free layer. At higher laser powers, the top layer dissolved at lower exposure doses, e.g. 2 mJ/cm^2 for 26 W versus 6 mJ/cm^2 for 22 W. By increasing EUV exposure dose above the threshold to clear the top layer after development, more photoacids were generated in the PAG-loaded top layer, which then diffused into the PAG-free bottom layer so as to deprotect the resist polymer and render part of the bottom layer soluble in the developer. The dose to clear the bottom layer was lower at a higher laser power, e.g. 8 mJ/cm^2 for 30 W versus $>$ 10 mJ/cm^2 for 22 W or lower powers.

The data points under the horizontal line $y = 0.55$ are of interest because they represent conditions where the top layer is cleared after development, which correspond to achieving and surpassing the desired pattern size of a positive-

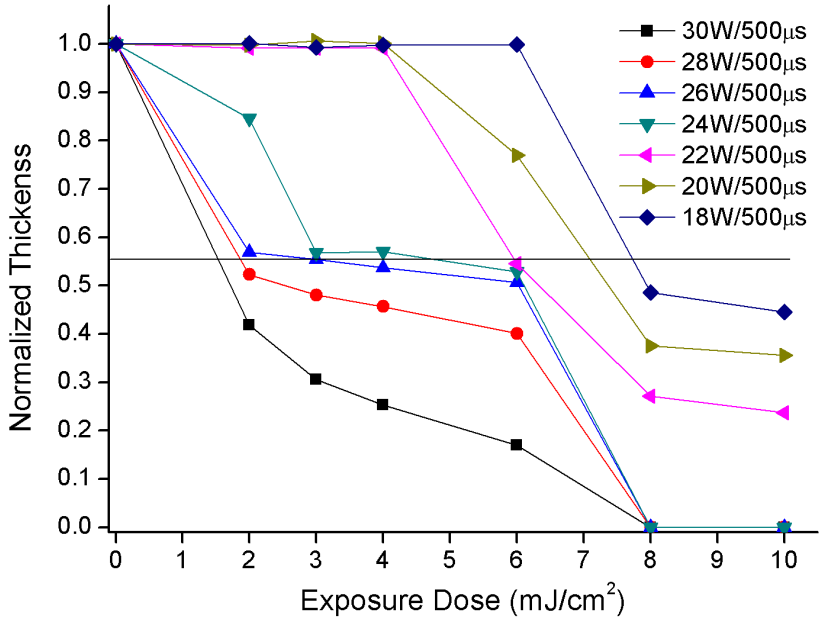

(a)

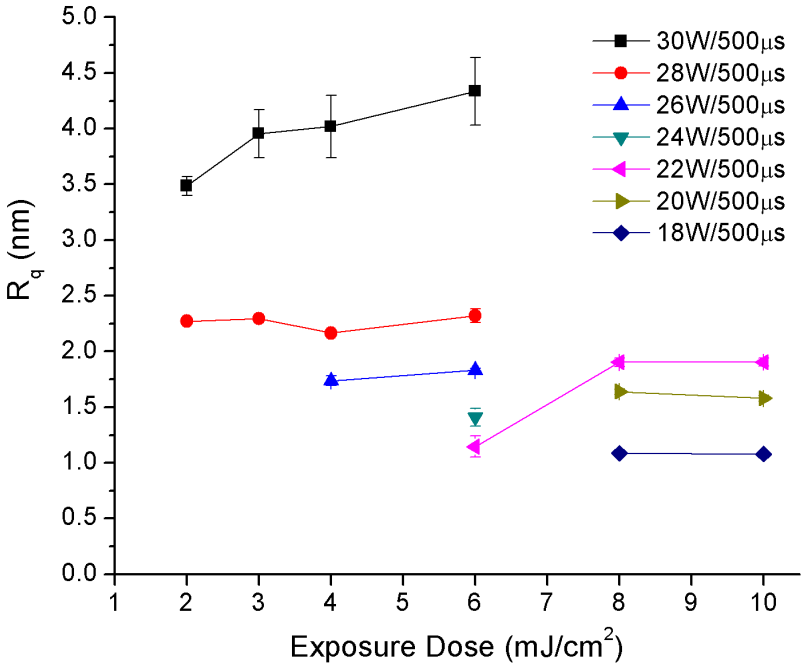

(b)

Figure 2.16: Film thickness (a) and surface roughness (b) of 193resist/THS bi-layer samples after EUV exposure, hot plate or laser PEB, and development.

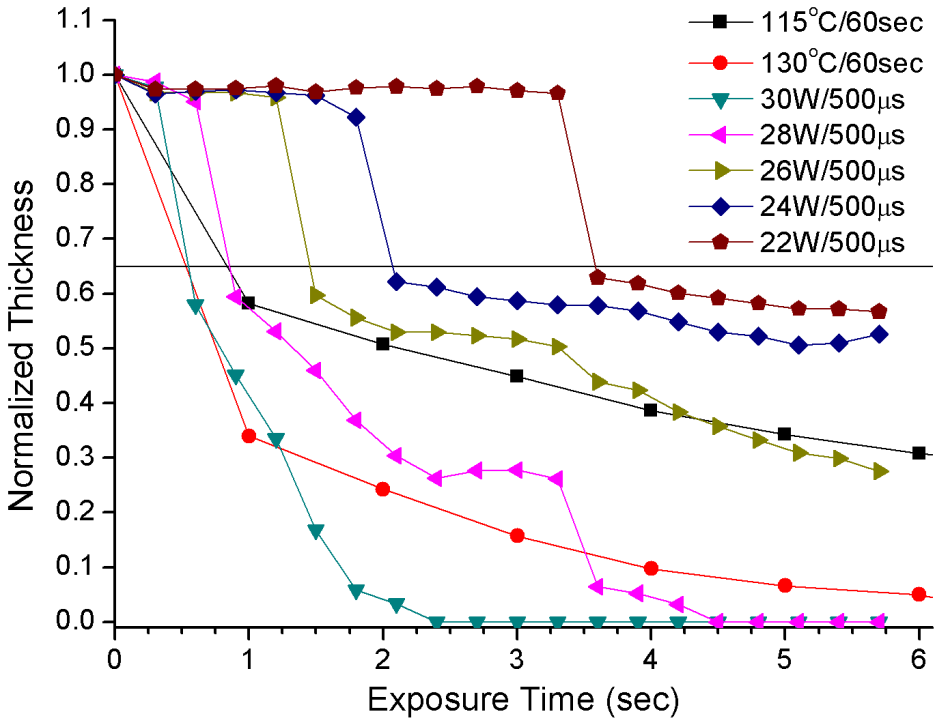

Figure 2.17: Film thickness of 193resist/THS bilayer samples after DUV exposure, hot plate or laser PEB, and development.

tone resist in real lithographic patterning. Surface roughness of the sample regions with normalized film thickness below 0.55 was measured by AFM and is displayed in Figure 2.16(b). While roughness seemed to increase slightly with higher dose, it is much more obvious that a higher laser power for PEB generally resulted in a larger surface roughness than a lower powered laser PEB, especially when the exposure conditions were comparable. Considering both the bottom layer thickness loss and developed surface roughness data shown in Fig. 2.16, it can be inferred that exposure dose, laser power, acid diffusion length, and surface roughness are all correlated and that lower laser powers may be the correct path to push for smaller acid diffusion and lower surface roughness but at the sacrifice of exposure dose.

Table 2.1: Summary of DUV exposure time, PEB conditions, and surface roughness of the post-development sample regions with a common thickness loss of ~ 10 nm in the bottom layer.

	115°C/60sec	22W/500μs	26W/500μs	30W/500μs
DUV exposure time (sec)	1.0	5.4	1.8	0.6
Thickness loss (nm)	10.5	11.2	13.3	9.6
Surface roughness (nm)	0.828	0.880	0.918	1.42

As data of EUV exposed bilayer samples by hot plate PEB was missing to compare with laser PEB, DUV exposure was conducted on another batch of 193resist/THS samples on an ABM contact aligner at 254 nm (measured power ~6 mW/cm^2) for exposure up to 6 sec. Following exposure, the films were annealed on a hot plate at 115 °C or 130 °C for 60 sec or by laser from 22 to 30 W with a dwell time of 500 μs. The processing and characterization steps after PEB were identical with those for the EUV exposed samples. Figure 2.17 plots post-development film thickness against DUV exposure time under different PEB conditions. The horizonal line at around $y = 0.65$ marks the interface between the top PAG-loaded layer and the bottom PAG-free layer. The trend that lower exposure time was needed to clear the top layer or the whole bilayer with higher laser power was again observed with DUV exposed samples. The observation was consistent with the hot plate PEB results and expected as photoacids diffuse faster at a higher PEB temperature. As shown in Figure 2.17, under the same exposure conditions, thickness loss in the bottom layer was smaller with laser PEB at 22-26W/500μs than hot plate PEB at 115°C/60sec, which is the typical PEB condition for the resist system.

Surface roughness data of post-development samples is selected and compared in two tables. Table 2.1 summarizes the exposure time, PEB conditions,

Table 2.2: Summary of DUV exposure time, PEB conditions, and surface roughness of the post-development sample regions with a common thickness loss of ~ 48 nm in the bottom layer.

	115°C/60sec	130°C/60sec	26W/500μs	28W/500μs	30W/500μs
Expo. time (sec)	5.0	1.0	4.8	1.8	1.2
Δd (nm)	47.4	48.3	49.4	42.7	48.0
R_q (nm)	1.00	1.66	0.940	1.07	1.43

and surface roughness of the post-development sample regions with a common thickness loss of ~ 10 nm in the bottom layer. The DUV exposure time for hot plate PEB at 115°C was on the same order as only that for laser PEB at 30 W but much shorter than the exposure time for laser PEB at 22 or 26 W. In terms of surface roughness, laser PEB generated rougher post-development surfaces than hot plate PEB at 115 °C, especially at higher temperatures.

Table 2.2 is similar to table 2.1 except that the comparison is made at a common thickness loss of ~ 48 nm in the bottom layer. While hot plate PEB at 130°C/60sec and laser PEB 30W/500μs appeared to give the roughest developed surfaces, laser PEB at 26 and 28 W resulted in surface roughness comparable to hot plate PEB at 115 °C with a shorter exposure time.

Figure 2.18 plots surface roughness of post-development 193resist/THS samples against thickness loss in the bottom layer under different PEB conditions, with the data uncertainty within ≈ 5 % of the mean. It is noteworthy to point out that the 193 resist material used in the DUV exposure experiments was from a product batch different from that used in the EUV exposure experiments, so the molar ratio of the two blocks in the polymers and the molecular weight distribution were not idential between batches and this may explain some inconsistency in the range of measured surface roughness data. However, the

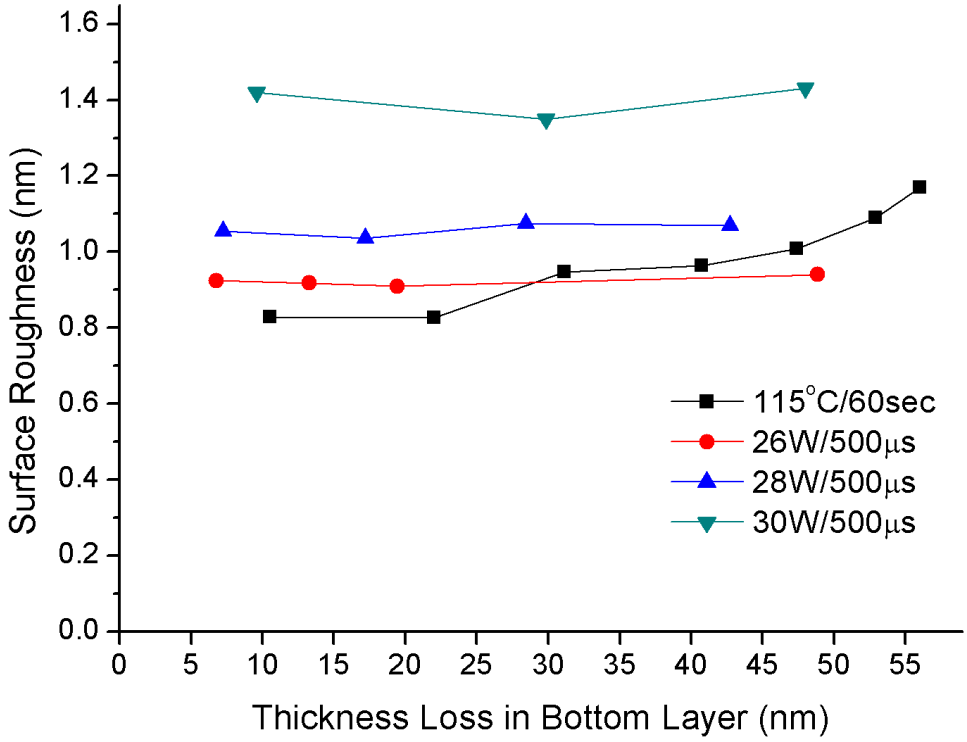

Figure 2.18: The relationship between surface roughness of post-development 193resist/THS samples (with hot plate PEB at 115 °C and laser PEB at 26, 28, and 30 W) and thickness loss in the bottom layer.

comparison between hot plate and laser PEB is not compromised because the same resist formulation was used in this case for both the PEB methods.

For hot plate PEB at 115°C/60sec, there was a clear trend of surface roughness increasing monotonically with thickness loss in the resist bottom layer. The dependance of surface roughness on film thickness loss was surprisingly not evident with laser PEB while laser power still had a large impact on surface roughness. For laser powers of 26 and 28 W, a similar range of surface roughness was observed for hot plate PEB at 115 °C. Based on the data presented in the plot, decreasing the laser power below 26 W can be expected to reduce surface roughness below that of a hot plate PEB.

2.8 Conclusions and Future Work

Preliminary and fundamental studies have been carried out to explore laser spike annealing for the first time as an alternative to hot plate annealing with hopefully improved performance. Sensitivity to exposure, LER in real lithographic patterning, and acid diffusion in resists and its effect on LER have been observed to be all different for laser PEB when compared to hot plate PEB. No proposed model is confirmed to explain the differences, but physical chemistry of resists during a post exposure bake with an enormously faster thermal ramp rate and a significantly shorter annealing time frame may account for some of the experimental observations.

For better understanding of laser PEB working mechanism and utilizing it to our advantage, future work should include studying the impact of varying laser anneal dwell time on acid diffusion and LER in resists, more research effort on low laser powers (< 26 W), expanding the resist library for study, and even using neutron reflectometry to determine and compare acid reaction-diffusion front profiles in resist films heated by laser and hot plate.

CHAPTER 3

SUPERCRITICAL CARBON DIOXIDE DEVELOPMENT FOR PHOTORESISTS

Supercritical fluids are a state of matter above both critical pressures and critial temperatures and possess properties intermediate between liquid and gas. Their liquid-like densities can facilitate dissolution of reagents and tunability of solvating power while their gas-like properties including high diffusivity and low viscosities are ideal for processing at the sub-micron scale. This chapter briefly reviews materials processing with supercritical CO_2 in the semiconductor industry, especially development of polymeric and molecular photoresists in supercritical CO_2. Since some of the processes depend highly on dissolution of materials in CO_2, mechanisms of material solubility in CO_2 are discussed and an approximation modeling method is proposed to predict the solubility. Experimental work on alicyclic molecular glass resists is presented as an example of incorporation of 193-nm lithography with supercritical CO_2 development. Future directions in the field of supercritical CO_2 development are discussed at the end of the chapter.

3.1 Materials Processing with Supercritical CO_2

For the semiconductor industry, supercritical CO_2 has been involved in materials processing steps such as conformal metal and metal oxide deposition [47, 48]

[1]Section 3.2.1 is reproduced with permission from J. Sha and C. K. Ober, "Fluorine- and siloxane-containing polymers for supercritical carbon dioxide lithography", *Polymer International*, 58, 302 (2009). Copyright 2009 John Wiley and Sons.

[2]Section 3.4 is reproduced with permission from J. Sha, J.-K. Lee, and C. K. Ober, "Molecular Glass Resists Developable in Supercritical CO_2 for 193-nm Lithography", *Proceedings of SPIE*, Vol. 7273, 72732T (2009). Copyright 2009 Society of Photo Optical Instrumentation Engineers.

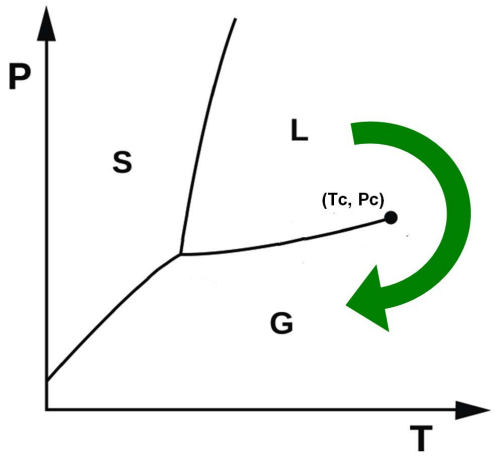

(a) Supercritical drying process

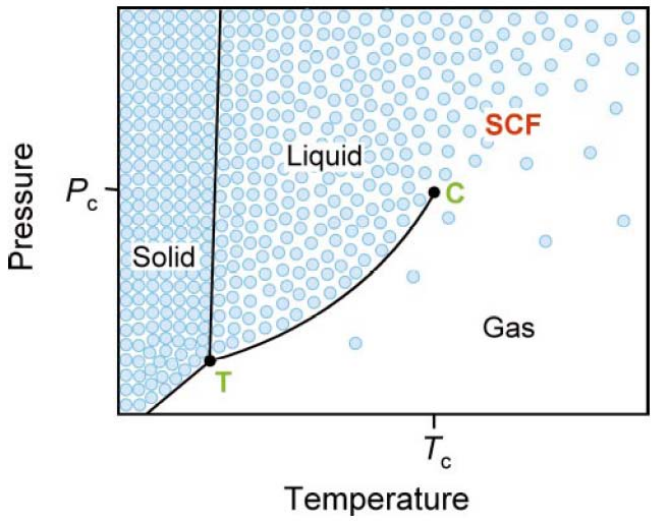

(b) CO_2 phase diagram

Figure 3.1: (a) Schematic of supercritical drying process and (b) CO_2 phase diagram.[76] Reproduced by permission of The Royal Society of Chemistry.

and etching [49, 50], preparation of porous ultra low k dielectrics [51, 52], wafer cleaning [56] and photoresist stripping [57], and photoresist processing [53] and development [54, 55, 75].

To show one of the advantages of supercritical fluids over conventional solvents, a supercritical drying process is illustrated in a $P - T$ phase diagram (Fig. 3.1(a)). The arrow shows the phase change path from liquid to gas phase

through the intermediate supercritical state. The benefit of this path is that the liquid-gas equilibrium line is never crossed and thus the drying fluid exists in only one phase all the time. Because of zero surface tension during the process, supercritical drying allows dense and high-aspect ratio features to be cleaned without causing any collapse. Fluids suitable for supercritical drying include carbon dioxide, freon, nitrous oxide and water. CO_2 is usually chosen as a supercritical drying solvent because its supercritical conditions are easily accessible (T_c = 31.1^oC, P_c = 7.39MPa) (Fig. 3.1(b)) and CO_2 is relatively inert compared to other solvent candidates.

3.2 Supercritical CO_2 Development

3.2.1 Polymeric Resists for Supercritical CO_2 Development

Although CO_2 tends to be a very poor solvent for most polymers including current mainstream photoresists, certain fluorine- and siloxane-containing polymers have been shown soluble under moderate supercritical conditions.

Fluorinated Polymers

In an early example of a scCO_2-developable photoresist, tetrahydropyranyl methacrylate (THPMA) and fluorinated methacrylate (F7MA) were combined in a block copolymer [P(THPMA-*block*-F7MA)] and shown to possess submicrometer patterning capabilities with scCO_2 development.[75] The very nonpolar fluoromethacrylate, highly soluble in scCO_2, was chosen for copolymer-

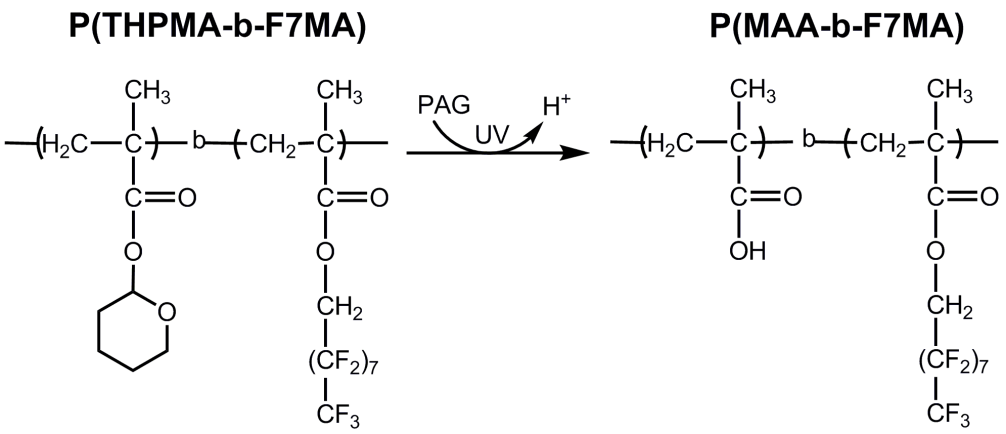

Figure 3.2: Lithographic patterning mechanism of the negative-tone $scCO_2$-developable P(THPMA-*block*-F7MA).

ization with THPMA, which in the presence of protons undergoes chemically amplified polarity change and thus solubility change of the block copolymer in $scCO_2$. Figure 3.2 shows the patterning mechanism of this chemically amplified negative-tone photoresist. The lithographic performance of the resist was characterized after 193 nm exposure and $scCO_2$ development. The achieved resolution was 0.1 μm.

Using the same block copolymer system, *in situ* chemical modification through silylation was proposed to create a positive-tone $scCO_2$ developable resist.[77] Light exposure at 248 nm of a cast film of the block copolymer and photoacid generator (PAG) molecules resulted in the formation of photoacids in the exposed region. After a post-exposure bake step, the acids cleaved the tetrahydropyranyl (THP) groups to produce methacrylic acid. During the subsequent silylation with either hexamethyldisilazane (HMDS) or tetramethyldisilazane (TMDS), the vapor of the silylation agent diffused into the polymer film and reacted with the available carboxylic acid groups. The attachment of $O\text{-}Si(CH_3)_3$ groups to the acid functions helped the exposed region regain

solubility in $scCO_2$ due to the favorable interaction between the organosilicon functional groups and CO_2. UV flood exposure was then applied to activate unreacted photoacid generators to cleave nonpolar THP protecting groups in the previously unexposed regions and render the polymers less soluble in $scCO_2$. After the silylation step and the following flood exposure, positive-tone patterns were achieved with good structural integrity down to 500 nm lines/spaces. Figure 3.3 illustrates the process for image reversal of the polymer resist.[78] While image reversal was successfully achieved with P(THPMA-block-F7MA), performance limitations such as incomplete film removal and excessive surface roughness were apparent, which might result from a block copolymer segregation effect. These problems could be solved by employing a P(THPMA-F7MA) random copolymer (60:40 molar ratio).[77] Figure 3.4 demonstrates the negative-tone and positive-tone patterning capabilities of the random copolymer. Besides using the aforementioned fluoromethacrylates as a block in some polymeric photoresists, efforts have also been made to explore other polymer backbones for $scCO_2$ development. One example is fluorinated polymers with stiff alicyclic backbones. Addition polymers (Fig. 3.5) containing a norbornyl backbone and fluorinated moieties were synthesized and the hydroxyl groups were protected with chemically amplified switching groups such as *t*-butoxycarbonyl group.[79] Lithographic imaging produced dense lines of the photoresist as small as 3 μm.

Besides developing high-aspect-ratio photoresist patterns in a more environmentally friendly way, supercritical CO_2 provides additional advantages over conventional developers because of the inert property of CO_2. One of the challenges for patterning organic semiconducting materials with conventional photolithography is the use of aqueous developer solutions which can

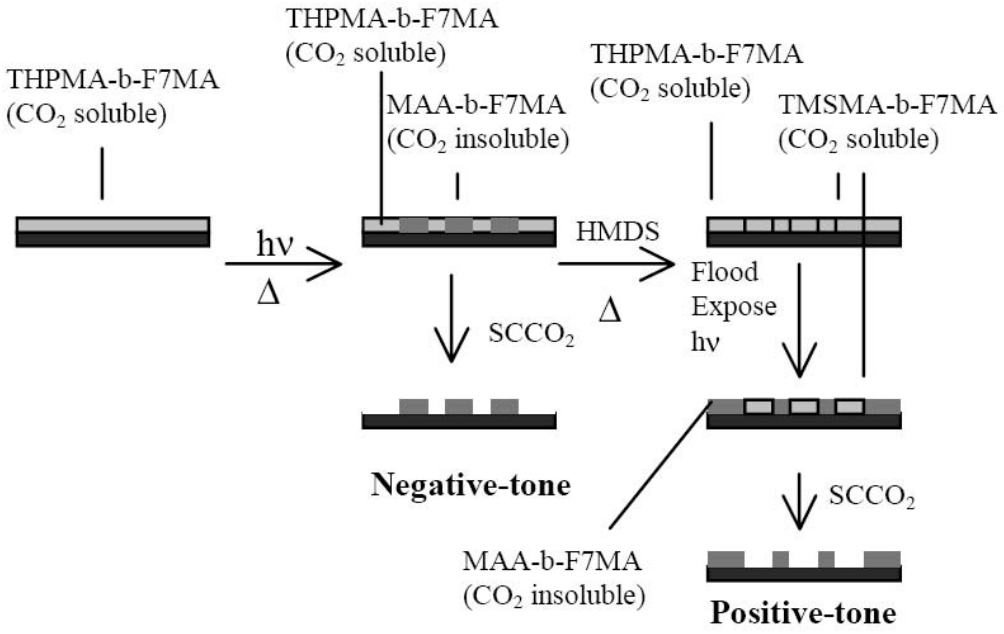

Figure 3.3: Schematic of the process to achieve image reversal and thus positive-tone $scCO_2$-developable resist with an additional silylation step using HMDS. Reprinted with permission from the authors of Pham *et al*.[78]

degrade the integrity of delicate organic materials so as to affect device performance. Recently, Lee and co-workers demonstrated the concept of orthogonal development by fabricating a patterned organic light-emitting device using $scCO_2$ development.[84] A resist similar to P(THPMA-F7MA) (shown in Fig. 3.2) was exposed to UV light through a mask and developed in $scCO_2$ at 40 °C and 27 MPa to give a negative-tone resist image on top of a film of poly(3,4-ethylenedioxythiophene):polystyrenesulfonate (PEDOT:PSS) (Figs. 3.6 (a) and (b)). It is worth mentioning that conventional aqueous developers can seriously damage the water-soluble PEDOT:PSS conducting film while $scCO_2$ leaves the film intact. Following the development, a solution of an organic light emitting material was spin-coated onto the patterned resist/PEDOT:PSS surface and finally a CsF/Al cathode was thermally deposited on top. The electroluminescent device showed uniform light emission during operation even from 5 μm pat-

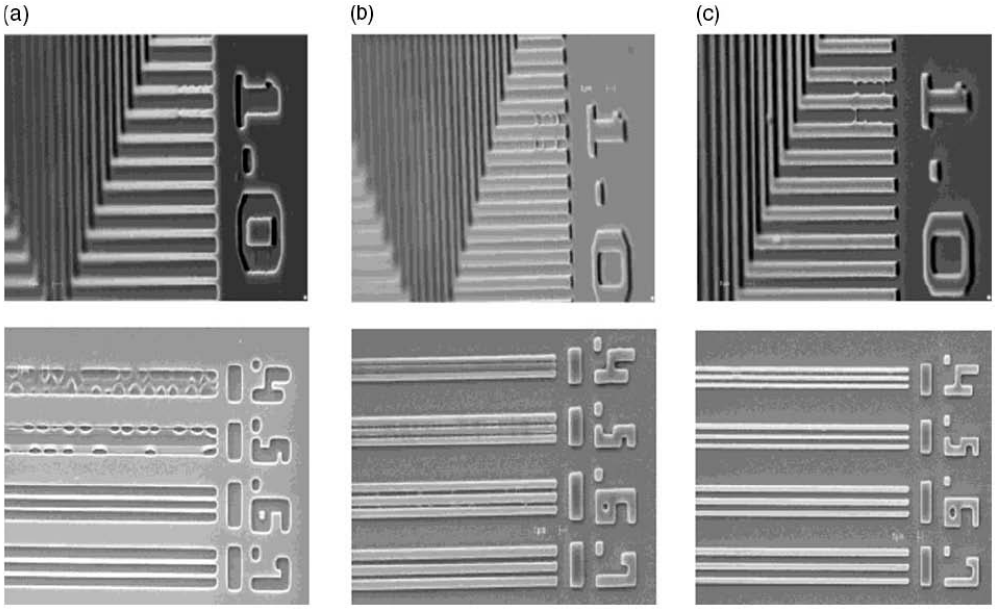

Figure 3.4: SEM images of the THPMA-F7MA random copolymer resist patterned by 248 nm photolithography: (a) negative-tone patterns developed by $scCO_2$; (b) positive-tone patterns after silylation with HMDS and $scCO_2$ development; (c) positive-tone patterns developed by $scCO_2$ after silylation with TMDS which was used to improve the lithographic performance. (Reprinted with permission from Pham *et al*.[77] Copyright 2008 American Chemical Society.)

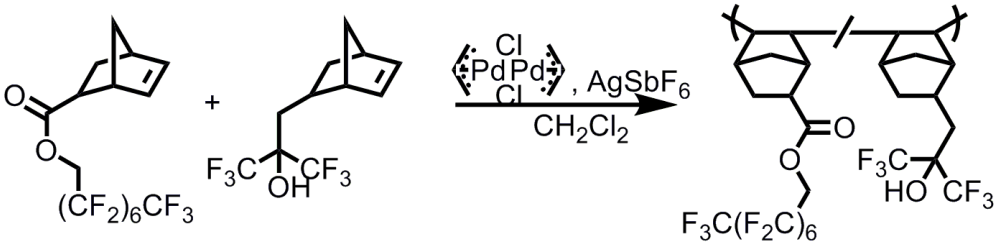

Figure 3.5: Synthesis schematic of the fluorinated addition copolymer of (norbonyl)perfluorooctyl acrylate (NBFOA) and (norbornyl)-1,1,1-trifluoro-2-tri(fluoromethyl)propan-2-ol (NBHFA). (Adapted from scheme 1 of Boggiano *et al*.[79]).

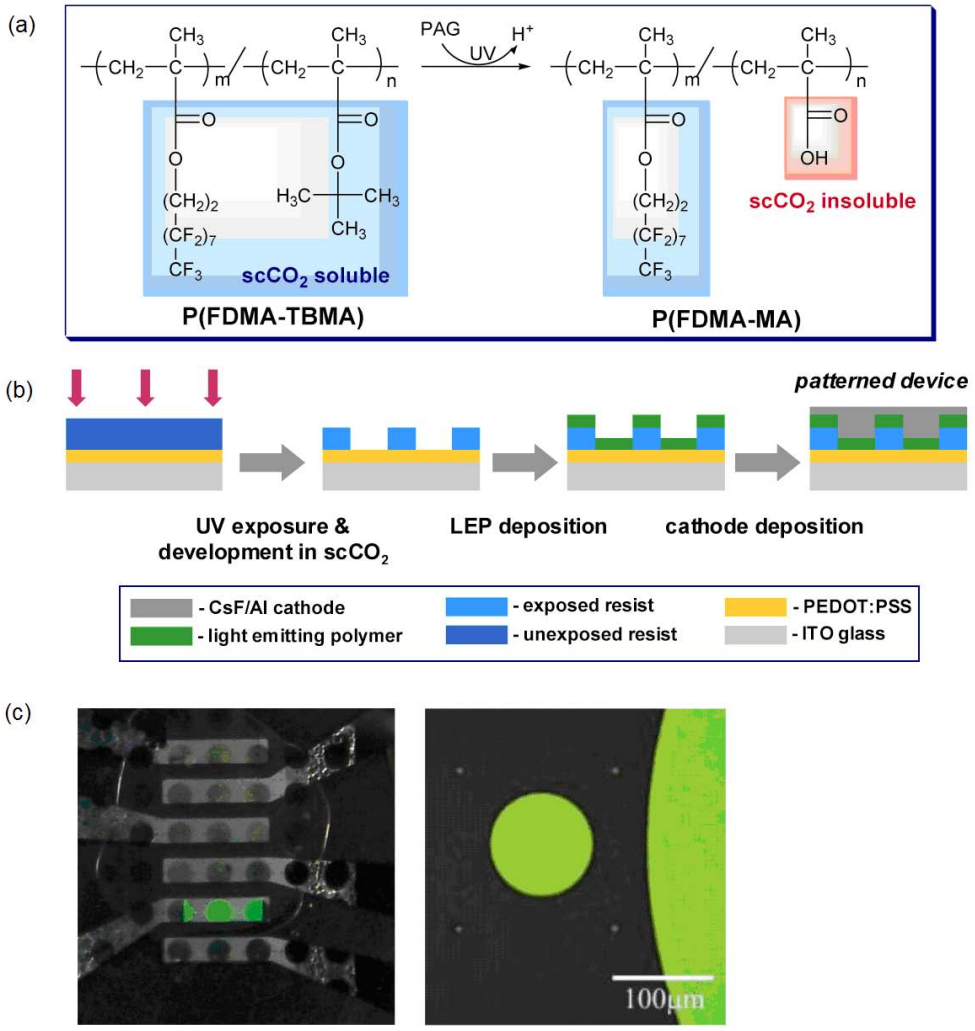

Figure 3.6: Photolithographic patterning an organic light-emitting diode with $scCO_2$ development: (a) the chemical reaction of the patterning materials upon exposure and baking; (b) schematic of device fabrication steps; (c) images of the final light-emitting device.[84] Reproduced by permission of The Royal Society of Chemistry.

terns (Fig. 3.6c). This $scCO_2$ development approach is highly compatible with the majority of materials used in organic electronic devices as well as materials in inorganic electronics.

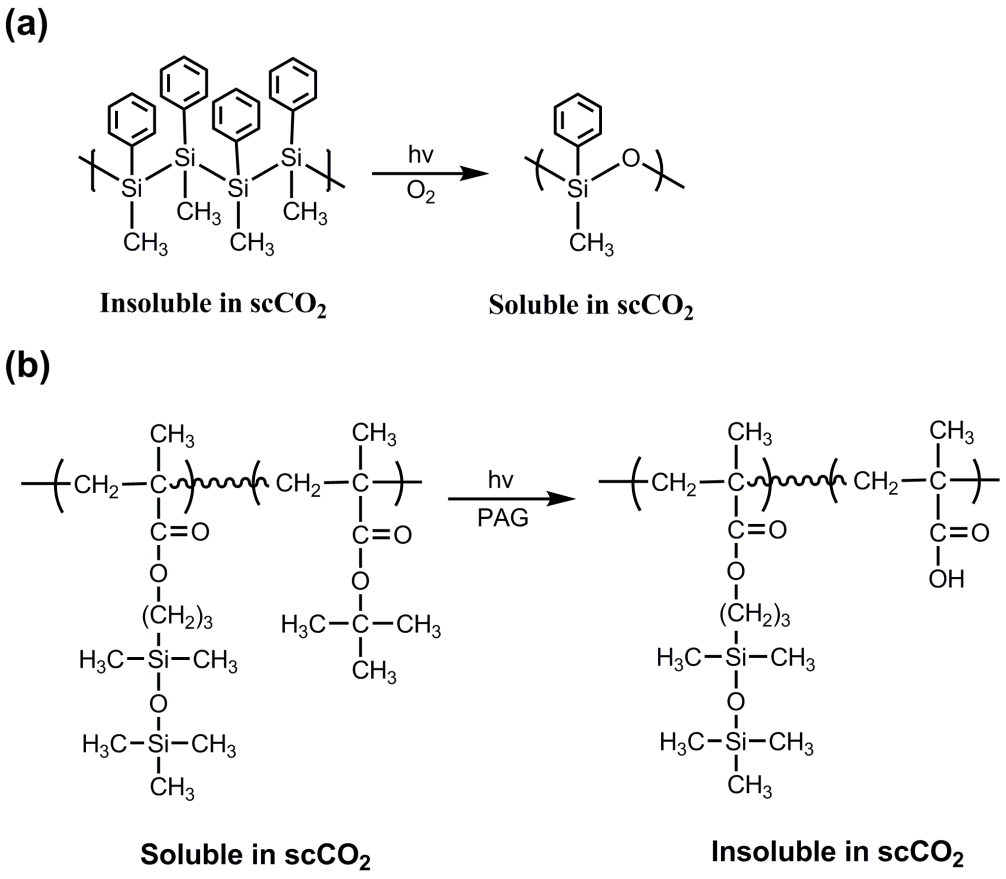

Figure 3.7: Solubility change mechanism of polysilane and P(*t*-BMA-*block*-SiMA) by photoinduced chemical reactions. (Adapted from Fig. 1 of Ober *et al*.[81])

Siloxane-Containing Polymers

Like fluorinated polymers, siloxane-containing polymers are also often soluble in $scCO_2$. They not only have the needed solubility in $scCO_2$ but also may be used as etch-resistant components. One of the early attempts to construct siloxane containing polymers that are processable in $scCO_2$ was to convert polysilanes to polysiloxanes by the photoinduced insertion of oxygen (Fig. 3.7a).[80, 81] The polymers were transformed from insoluble in $scCO_2$ to soluble and successfully imaged as a positive-tone resist. For negative-

tone imaging, several $scCO_2$-developable copolymers were produced from *t*-butyl methacrylate (*t*-BMA) and 3-methacryloxypropylpentamethyldisiloxane (SiMA) (Fig. 3.7b).[81, 82, 83] Although poly(*t*-BMA) homopolymer is usually insoluble in $scCO_2$, the solubility of the block copolymer poly(*t*-BMA-*block*-SiMA) was observed to increase when the weight fraction of the SiMA monomer units was raised. The block copolymer demonstrated excellent photosensitivity and good contrast as patterning materials.

3.2.2 Molecular Glass Resists for Supercritical CO_2 Development

Although $scCO_2$-processable polymeric photoresists have been investigated, sub 100 nm features were not achieved until some recent studies on high resolution patterning of molecular glass resists.[89] Molecular glass resists are low molecular-weight, amorphous imaging materials with low polydispersity, good thermal stability, and film-forming properties. They have been recognized as outstanding candidates for next-generation lithography because of their smaller addressable sizes compared to polymeric resists.[85, 86] In the aforementioned study by Felix *et al.*, CO_2-insoluble hexa(hydroxyphenyl) benzene (HHPB) molecules were investigated as a molecular glass resist for $scCO_2$ development.[89] It was found that protection of the six hydroxyl moieties with *tert*-butoxycarbonyl (*t*Boc) groups produced an amorphous material which is soluble in $scCO_2$ (Fig. 3.8a). Electron beam exposure of a thin film of *t*Boc protected HHPB and PAG and subsequent development of the film in $scCO_2$ (35 ^{o}C, 34 MPa, 3 min) resulted in non-collapsed 50 nm line/space patterns with an

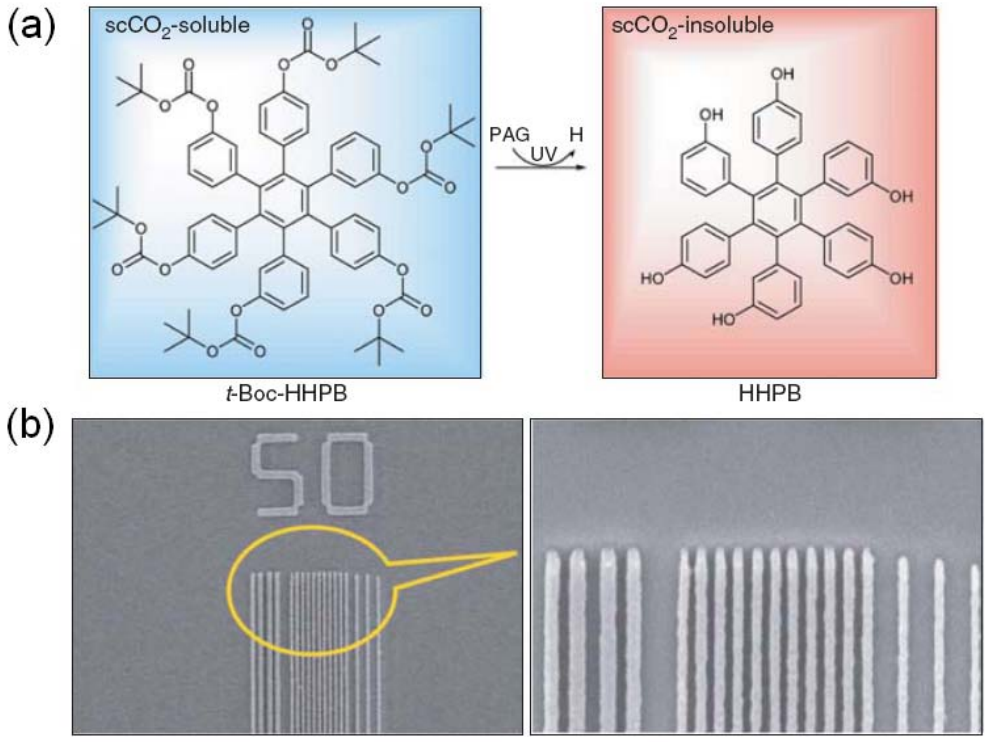

Figure 3.8: Lithographic patterning of a nonfluorinated molecular glass resist with $scCO_2$ development. (a) chemical reactions during the patterning process, (b) SEM images of 50-nm line/space patterns. The right image is an expansion of the left. Note: HHPB is hexa(hydroxyphenyl)benzene, *t*-Boc-HHPB is *tert*-butoxycarbonyl-protected HHPB, and PAG is photoacid generator. Reproduced with permission from Reference [89].

aspect ratio of around 3 (note the 11 lines in the middle of Figure 3.8b).

3.3 Solubility in CO_2

3.3.1 Molecular Thermodynamics of Organic-CO_2 Mixtures

The principles of molecular thermodynamics bridge classical thermodynamics with physicochemical properties of the components in solution. The molec-

ularly directed methodology provides insight for design of materials that are miscible in $scCO_2$ at moderate conditions.

To form a stable mixture of organic compounds in $scCO_2$ at a specific temperature and pressure, the Gibbs free energy must be negative and at a minimum.[62] The Gibbs free energy of mixing is $\Delta G_m = \Delta H_m - T\Delta S_m$, where ΔH_{mix} and ΔS_{mix} are the change in enthalpy and entropy upon mixing respectively. Enthalpy, in the case of dissolution of organic molecules in $scCO_2$, depends predominantly on solution density and on organic-organic, CO_2-CO_2, and organic-CO_2 interaction energies. ΔS_{mix} depends on both the combinatorial entropy of mixing and the noncombinatorial contribution associated with the volume change upon mixing. The combinatorial entropy always promotes the mixing of organic molecules with CO_2. Although it is impossible to rigorously decouple energetic and entropic contributions to the Gibbs free energy of mixing, it is possible to design phase behavior experiments that magnify or minimize the impact of enthalpies relative to entropic contributions. For those design experiments, molecular thermodynamics provides an approach to quantifying the interactions that govern the phase behavior of organic-$scCO_2$ mixtures.

For a dense solution of $scCO_2$ and organic molecules, ΔH_{mix} is approximately equal to the change in internal energy upon mixing, ΔU_{mix}, which is expressed by the following equation.[63]

$$\Delta U_{mix} \approx \frac{2\pi\rho(P,T)}{kT} \sum_{i,j} x_i x_j \int \Gamma_{ij}(r,T) g_{ij}(r,\rho,T) r^2 dr \tag{3.1}$$

where x_i and x_j are mole fractions of components i and j respectively, $\Gamma_{ij}(r,T)$ is the intermolecular pair-potential energy of $scCO_2$ and organic segments, $g(r,\rho,T)$ is the radial distribution function, r is the distance between molecules,

$\rho(P,T)$ is the solution density, and k is the Boltzmann constant. The equation provides some generalities about phase behavior. For example, given that the internal energy of the mixture is roughly proportional to density, the solubility of an organic compound is expected to improve with increasing system pressure or use of a denser $scCO_2$ solvent. However, the organic will dissolve only if the energetics of organic-CO_2 interactions outweigh organic-organic and CO_2-CO_2 interactions, i.e. the intergral in eq. 3.1 cannot be completely ignored.

An approximation form of the intermolecular potential energy $\Gamma_{ij}(r,T)$ is

$$\Gamma_{ij}(r,T) \approx -[C_1\frac{\alpha_i\alpha_j}{r^6} + C_2\frac{\mu_i^2\mu_j^2}{r^6kT} + C_3\frac{\mu_i^2Q_j^2}{r^8kT} + C_4\frac{\mu_j^2Q_i^2}{r^8kT} + C_5\frac{Q_i^2Q_j^2}{r^{10}kT} + \cdots] \tag{3.2}$$

where α is the component polarizability, μ is the component dipole moment, Q is the component quadrupole moment, and C_{1-5} are constants.[62] In the case of dissolving organic molecules X in $scCO_2$ ($\mu_{CO_2} = 0$), the equation can be rendered as

$$\Gamma_{X,CO_2}(r,T) \approx -[C_1\frac{\alpha_X\alpha_{CO_2}}{r^6} + C_3\frac{\mu_X^2Q_{CO_2}^2}{r^8kT} + C_5\frac{Q_X^2Q_{CO_2}^2}{r^{10}kT} + \cdots] \tag{3.3}$$

The term for the potential energy of dipole-quadrupole interactions in eq. 3.3 is inversely proportional to temperature. At elevated temperatures, thermal energy disrupts the configurational alignment of the polar moments of the X molecules so that they behave as if they were nonpolar. Hence, it may be possible to dissolve a polar organic material in a nonpolar solvent like $scCO_2$ by increasing temperature. Besides, the strengths of dipole interactions and quadrupole interactions scale with $v^{-1/2}$ and $v^{-5/6}$ respectively, where v is the molar volume. Elevated pressure favors polar interactions and thus dissolution of organic molecules in $scCO_2$. Equations 3.1 and 3.3 describe how the solvating quality of $scCO_2$ can be tuned with changes in pressure and/or temperature, a degree of flexibility not available with liquid solvents.

3.3.2 Prediction of Solubility by Modeling

Phase behavior of organic compounds in $scCO_2$ has been predicted by several modeling theories including Statistical Associating Fluid Theory (SAFT) equation of state [64, 65, 66, 67, 68], group contribution theory [70, 71, 72], and theories about strong electron-withdrawing groups [73, 74] promoting solute solubility in $scCO_2$.

For more accurate results, *ab initio* methodology has been used to model the interaction of CO_2 with specific functional groups on polymers.[60, 61] Beckman *et al.* carried out the calculations of the interaction energies between CO_2 and the molecules of interest in three steps.[61] First, initial guesses were made for the configurations by placing a CO_2 molecule at various locations around the target molecule. Second, a Møller-Plesset perturbation theory (MP2) with the 6-31+g(d) basis set was used to optimize the initial configurations. This medium-sized basis set was chosen to increase the efficiency of the optimization calculations. Finally, single point energy calculations were performed with MP2 and the Dunning aug-cc-pVDZ basis set on the optimized structures to obtain more accurate interaction energies.

This modeling process for interaction energies between the target molecule and CO_2 is both time consuming and computing capacity demanding. For a rough estimation of material solubility in CO_2 at an early step of molecular design, a simpler and more straightforward method is needed. Results of some modeling work by Beckman and coworkers suggest that, in the configurations of lowest binding energies, CO_2 molecules were observed to be closer to the most negatively charged elements and their chemically bonded and most positively charged elements. This can be explained with the fact that only at those

sites can CO_2 quadrupoles have strong attractive interactions with the local dipoles formed by the highly charged and chemically bonded elements of the target molecule to promote dissolution.

Following this reasoning, a method for estimation of solubility of molecules/functional groups in CO_2 is proposed here. A simplified chemical structure is used to increase calculation efficiency. Energy minimization is first carried out to optimize the initial configuration. Subsequently, Mulliken charges of all the elements of the molecule are calculated using the HF/6-31g(d) model (Hartree-Fock theory using a medium-sized basis set). Introducing a zero-dipole-moment CO_2 molecule in the surrounding of an organic molecule should not result in a significant disturbance of the charge distribution in the organic molecule. Therefore, a calculation of charge distribution of the organic molecule, without the effect of CO_2 taken into account, is sufficient for qualitative analysis. To prove the validity of the method, three sets of modeling examples are presented here to compared with experimental results.

Protonated versus Fluorinated Methacrylates

Figure 3.9 shows the simplified chemical structures of protonated and fluorinated methacrylates for modeling. The fluorinated methacrylate was demonstrated as a very CO_2-soluble block in some copolymers while the protonated counterpart was not. As seen from the calculated Mullikan charges labeled in the figure, the major difference between the two methacrylates is that the carbon atoms in the side chain of the fluorinated molecule are significantly more charged than their counterparts in the protonated molecule and the bonded fluorine atoms are also more charged than the bonded hydrogen atoms. Therefore,

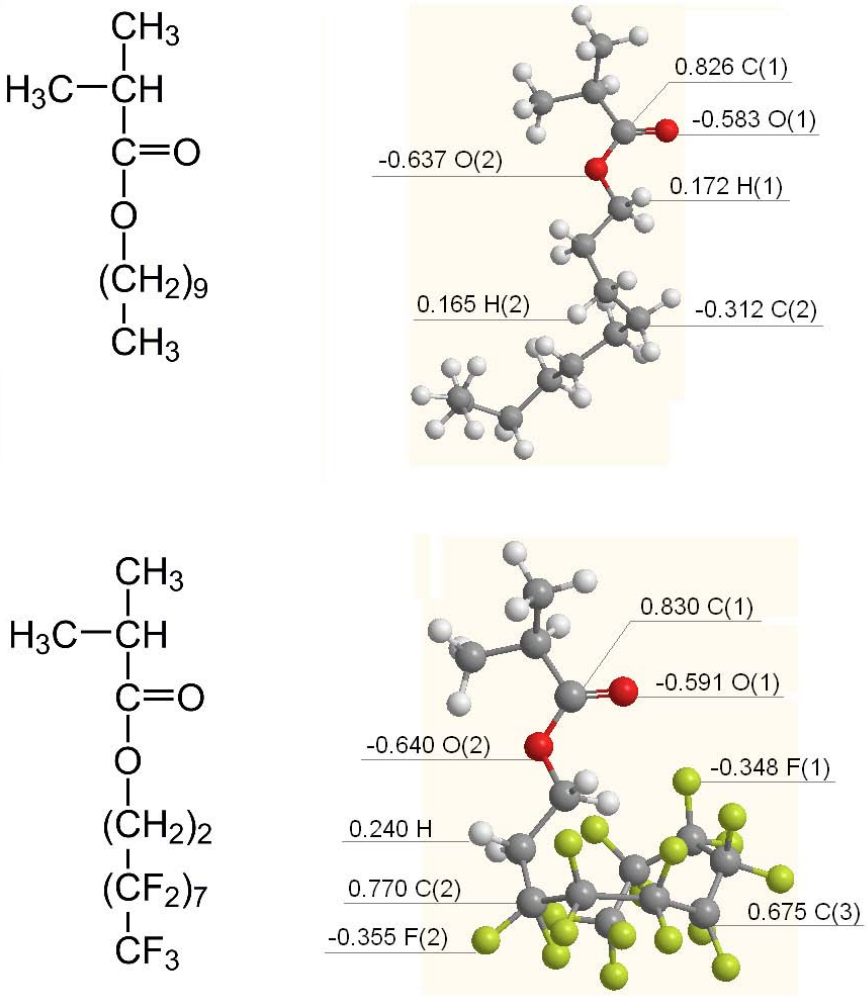

Figure 3.9: Simplified chemical structures and modeling results of protonated (upper) and fluorinated (bottom) methacrylates.

a higher solubility of fluorinated methacrylate results from the stronger local dipoles caused by fluorine's electron-withdrawing property.

Silane versus Siloxane

Figure 3.10 displays the simplified models of the chemical structures in Figure 3.7 and the calculated Mullikan charges of atoms of interest. When silicon

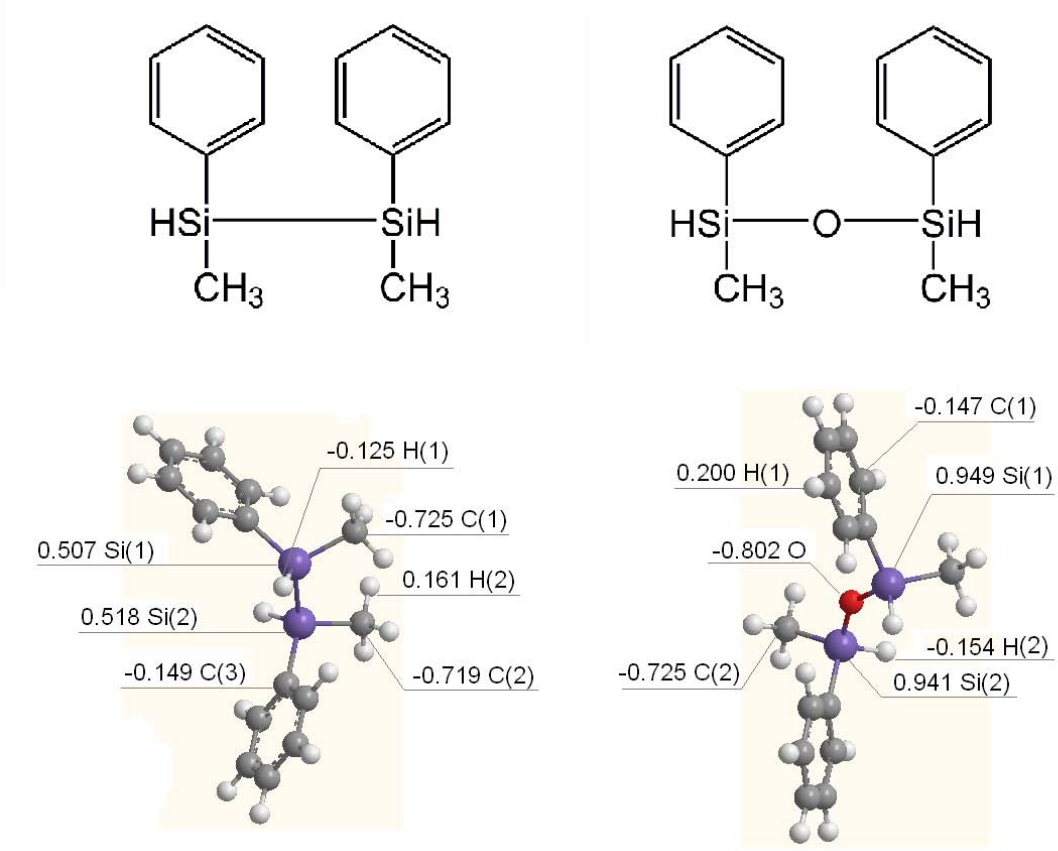

Figure 3.10: Simplified chemical structures and modeling results of polysilane (upper) and polysiloxane (bottom).

atoms are directly bonded, they possess moderate Mullikan charges of about 0.5 and the carbon atoms bonded to them are charged at approximately -0.7. After the insertion of an oxygen atom between the silicon atoms, both the oxygen (O) and silicon atoms (Si(1) & Si(2)) are highly charged compared to the previous case while the charges of the carbon atoms (C(2)) bonded to Si almost remain unchanged. Stronger local dipoles and thus higher solubility of siloxane is confirmed by the modeling method. Due to a solubility difference, the polysilane in Figure 3.7 was successfully used as a positive-tone resist after $scCO_2$ development.[81] It may also be argued that polysiloxane has a more flexible backbone than polysilane and thus provides a larger change in entropy upon

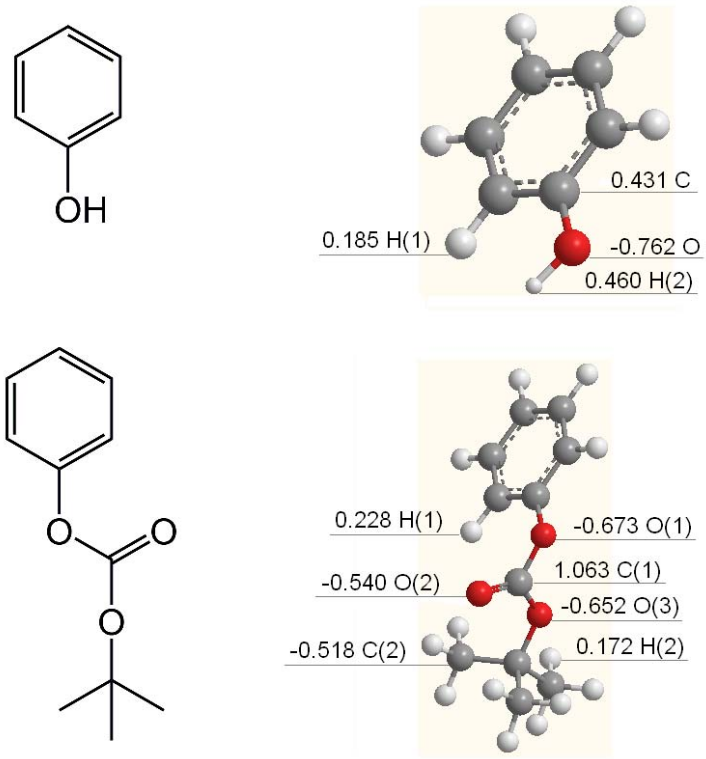

Figure 3.11: Simplified chemical structures and modeling results of phenol (upper) and *t*Boc-protected phenol (bottom).

mixing with CO_2 which favors dissolution. However, the enthalpic contribution is the dominant factor according to the estimation results here.

Phenol versus *Tert*-Butoxycarbonyl Protected Phenol

The *tert*-butoxycarbonyl (*t*Boc) group has been widely used in CO_2-developable molecular glass resists with aromatic cores. The modeling results as shown in Figure 3.11 indicate that the high solubility of *t*Boc in CO_2 results from the high Mullikan charges of the carbon atom (C(1)) and its surrounding oxygen atoms. It is confirmed by modeling that *t*Boc protected molecules are much more soluble in CO_2 than their unprotected counterparts terminated by hydroxyl groups.

The approximation modeling method has proved useful in most cases for an estimation of material solubility in CO_2 and a prediction of contrast between exposed and unexposed photoresist after $scCO_2$ development. Because this method is based on the interaction of CO_2 with one specific molecule, it may be limited when predicting solubility of certain compounds, e.g. carboxylic acids which tend to form dimers resulting in a weaker attractive interaction with CO_2 molecules because of the possible atomic charge redistribution. However, in terms of modeling solubility contrast in general, the approximation method should be able to provide some theoretical insight into the molecular design for CO_2-developable photoresists.

Most of the examples modeled above are based on aromatic cores which have strong absorption at deep UV wavelengths and cannot be used with the current preferred leading exposure technique, 193 nm (immersion) lithography. Molecular designs based on non-aromatic cores need to be tested to check whether their solubility contrast (solubility before and after protecting groups are removed) is high enough to qualify for $scCO_2$-developable 193-nm photoresists. Below are two examples of non-aromatic based molecular glass resist designs for 193 nm lithography and $scCO_2$ development.

Cyclohexanol versus *Tert*-Butoxycarbonyl Protected Cyclohexanol

The Mullikan charges were calculated on the elements of a cyclohexanol and its *t*Boc protected version. Modeling of the simplified chemical structures were used to demonstrate whether *t*Boc protecting groups could still facilitate solubility in CO_2 when they were attached to non-aromatic cores. Figure 3.12 shows that C(1) and its surrounding oxygen atoms were still highly charged even when

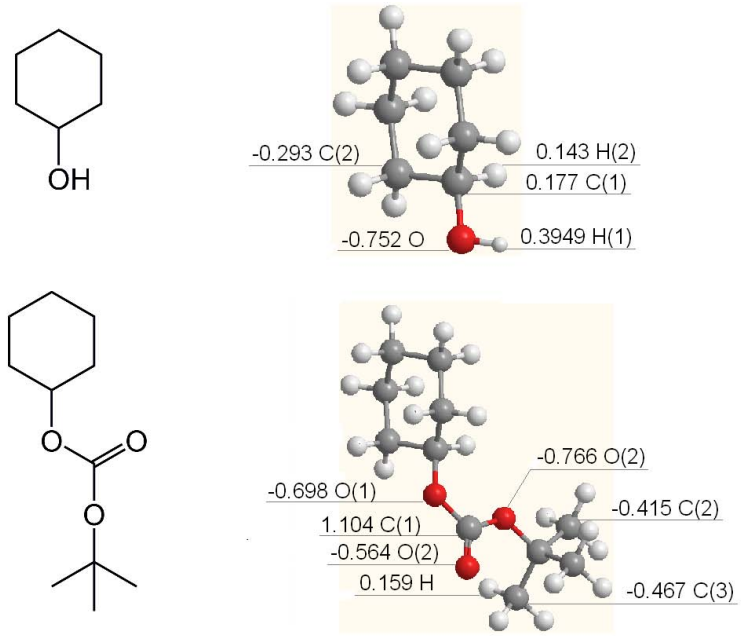

Figure 3.12: Simplified chemical structures and modeling results of cyclohexanol (upper) and *t*Boc-protected cyclohexanol (bottom).

the *t*Boc protecting group was attached to a cyclohexanol instead of a phenol. Considering the charge distributions in the cyclohexanol unit, different solubilities in CO_2 were expected for cyclohexanol and its *t*Boc-protected version, just as the case of phenol and *t*Boc-protected phenol.

Methylated Cyclodextrin versus *tert*-Butyl Ester of Methylated Cyclodextrin

Methylated cyclodextrin was simplified to the chemical structure in Figure 3.13 as another non-aromatic core for 193 nm lithography. Considering the ease of chemical synthesis, a new protecting group was attached to methylated cyclodextrin and measured for its charge distribution in a simplified molecular model. While the charges of the elements on the methylated cyclodextrin core only changed slightly after the introduction of the *tert*-butyl ester protecting

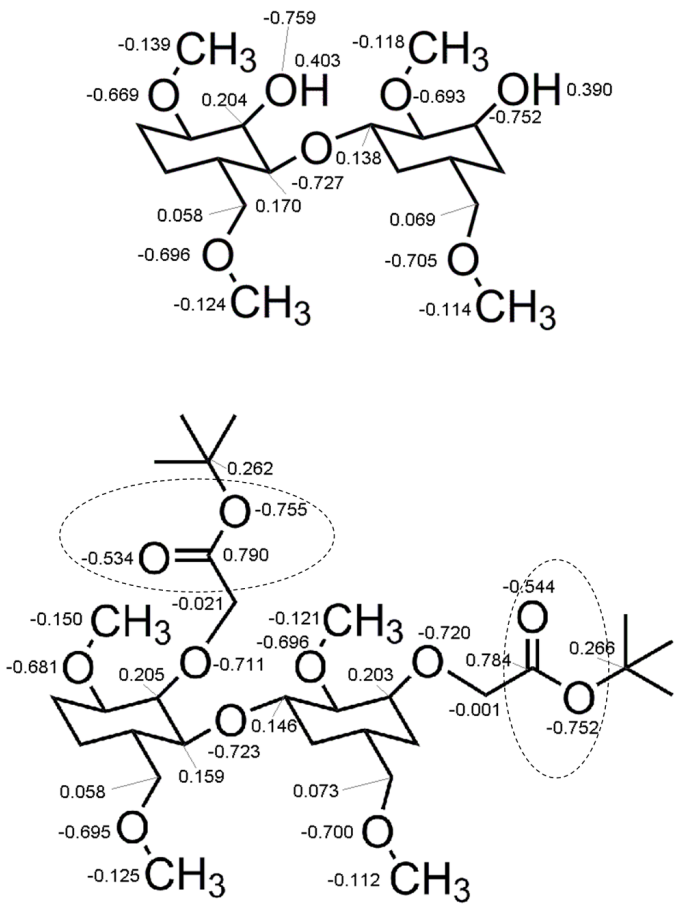

Figure 3.13: Simplified chemical structures and modeling results of methylated cyclodextrin (upper) and *tert*-butyl ester of methylated cyclodextrin (bottom).

group, the carbon and oxygen atoms of the protecting group circled in the figure possessed very high Mullikan charges compared to the rest of the molecule and could form strong local dipoles which would in turn have strong attractive interactions with the quadrupole found in CO_2 molecules.

The modeling results of the two above simplified non-aromatic molecules suggested that a CO_2 solubility switch was theoretically possible for these molecules with an acid-catalyzed deprotection step. The next section will present the experimental testing of two alicyclic molecular glass resists based

on these predicted CO_2-soluble designs.

3.4 Alicyclic Molecular Glasses for 193-nm Lithography

3.4.1 Introduction to Alicyclic Cores for scCO$_2$-Developable Molecular Glass Resists

Although CO_2 tends to be a very poor solvent for polymers such as those used in current photoresists are composed of, certain fluoropolymers [87], silicones [88] and molecular glass resists [89] have been shown to be soluble under moderate supercritical conditions. Molecular glass materials (defined as non-polymeric glass-forming macromolecules) are considered to have several advantages over linear polymers for photoresists. First, higher patterning resolution is expected due to the smaller molecular size of the molecular glass photoresists compared with that of polymeric resists. Second, since the low molecular weight molecular glasses are free of intermolecular chain entanglement, less internal stress can build up during lithographic processes compared to their polymeric counterparts. Therefore, pattern distortion resulting from film stress and polymer chain entanglement should be reduced during development.[90, 91, 92]

Most of the molecular glass resists explored for CO_2 development prior to this study are based on aromatic rings [93] which have strong absorption at deep UV regime and thus their applications cannot extend beyond EUV and electron-beam lithography to 193-nm lithography. However, some contributions towards molecular glass designs for 193-nm lithography are noteworthy.

One of the earliest reports is based on several branched structures including adamantane and cholic acid derivatives.[94, 103] Recent progress involves cyclodextrin ring structures [96] and POSS-based molecular systems [97]. These resist materials don't show high enough glass transition temperatures and can have difficulty achieving high contrast for sub 100 nm pattern resolutions. Also, liquid solvents are used for the development of all the materials.

Molecular glass materials based on naturally occurring cores are reported here for the first time as $scCO_2$-developable resists for 193-nm lithography. Cyclodextrins (cyclic oligomers of amylase) have drawn much interest since their discovery in 1891.[98] The geometry of cyclodextrins gives the hydrophilic molecules hydrophobic inner cavities so that various hydrophobic molecules can be fitted inside to form supramolecular inclusion complexes. Obtained from a renewable source (starch), cyclodextrins have low-toxicity and are biodegradable.[99, 100] Methylated β-cyclodextrin is used here as the core of a molecular glass resist because chemical modification on the molecule can be easily accomplished due to its improved solubility in common organic solvents compared to β-cyclodextrin. The reduced number of hydroxyl groups in methylated β-cyclodextrin can be protected more easily and give better contrast when the protection ratio remains the same as that of β-cyclodextrin. Another example of alicyclic natural materials is cholic acid. Cholic acid is well known to have strong intermolecular interactions contributing to the high glass transition temperatures of itself and cholates (cholic acid salts) as well. *Tert*-butyl cholate is employed because it has good etch resistance and transparency at 193 nm due to its alicyclic saturated chemical structure. These core molecules are protected with acid-labile and CO_2-soluble *t*Boc or *tert*-butyl ester groups. Photoacids generated during exposure can cause catalytic deprotection of *t*Boc

groups and render the molecular glass resists insoluble in $scCO_2$, making them negative-tone 193-nm resists.

According to the modeling results in the previous section, a CO_2 solubility switch was theoretically predicted for the two molecules glass resists based on alicyclic cores with an acid-catalyzed deprotection step. The following subsections will present the patterning capabilities of these compounds with electron-beam exposure and $scCO_2$ development for 193nm lithography.

3.4.2 Experimental

Materials

Cholic acid was purchased from Alfa Aesar, and used as received. Di-*tert*-butyl dicarbonate [$(t\text{BOC})_2\text{O}$], 4-(dimethylamino)pyridine, NaH (60% oil dispersion), methylated β-cyclodextrin (1.6-2 methyl groups per each glucose unit), *tert*-butyl bromoacetate were purchased from Sigma-Aldrich and used without further purification. Anhydrous tetrahydrofuran and *N*,*N*-dimethylformamide were purchased from Sigma-Aldrich and used without further drying.

Synthesis of cholic acid derivatives and methylated β-cyclodextrin

To a magnetically stirred solution of *tert*-butyl cholate [101] (5.00 g, 10.8 mmol) and 4-(dimethylamino)pyridine (0.13 g, 1.1 mmol) in tetrahydrofuran (30 ml) was added $(t\text{BOC})_2\text{O}$ (3.52 g, 16.1 mmol) at room temperature. The solution was stirred overnight and then poured into water (300 ml). The precipitated solid was recovered, washed with a copious amount of water and dissolved in

EtOAc (100 ml). The organic solution was then washed with brine (100 ml), dried over anhydrous $MgSO_4$, and concentrated under reduced pressure. The resulting foam was dried at 50 °C under reduced pressure to give the *t*BOC protected *tert*-butyl cholate as an off-white amorphous solid (4.95 g). Thermogravimetric analysis (TGA) suggested that one mole of product was protected with roughly one mole of *t*Boc protecting groups. The doubly *t*Boc protected *tert*-butyl cholate could be obtained by using two molar equivalent $(t\text{Boc})_2O$ over *tert*-butyl cholate.

To a magnetically stirred suspension of NaH [(60% oil dispersion, 4.27 g, 107 mmol), washed with anhydrous hexanes before use] in *N*,*N*-dimethylformamide (70 ml) was added methylated β-cyclodextrin (1.6-2 methyl groups per each glucose unit, 7.00 g, 5.3 mmol) in a water bath. The suspension was stirred for 10 min. *Tert*-butyl bromoacetate (14.6 g, 74.8 mmol) was then added slowly to the suspension drop-wise (Caution! Highly exothermic reaction). The reaction mixture was stirred overnight at room temperature and then poured into brine (300 ml). The aqueous/organic mixture was neutralized with a 10% (w/w) aqueous citric acid solution. The crude product was then extracted with EtOAc (300 ml). The organic solution was washed with brine (200 ml $\times$ 2), dried over anhydrous $MgSO_4$ and concentrated under reduced pressure. The resulting viscous solution was dripped into stirring hexanes (300 ml) to give an off-white precipitate. The powder was dried at 50 °C under reduced pressure to give the *tert*-butyl ester of methylated β-cyclodextrin as an off-white amorphous solid (9.97 g).

Characterization

The glass transition temperatures (Tg's) of the molecule glass materials were measured on a TA Instruments Q1000 Modulated Differential Scanning Calorimeter (DSC) at a heat/cool rate of 10 °C/min under N_2 for three heat/cool cycles. Tg was determined from the second heating/cooling cycle. Powder X-ray diffraction (XRD) was carried out on a Scintag Inc Theta-Theta Diffractometer at room temperature. Refractive indices and extinction coefficients were measured by a J. A. Woollam ellipsometer. Film thickness measurements were performed by a Tencor P10 profilometer.

Lithographic evaluation

The molecular glass compounds were dissolved in propylene glycol methyl ether acetate (PGMEA). A 5 wt.% loading (with respect to molecular glass solids) of iodonium nonafluorobutanesulfonate photoacid generator (PAG) was added to the spinning solutions before filtering through 0.2 μm filters and spin coating. After post-apply baking at 115 °C, films were then flood exposed at various doses at 254 nm using an ABM high resolution mask aligner. Post-exposure baking (PEB) was performed at 115 °C/60 seconds for *tert*-butyl ester of methylated β-cyclodextrin and 90 °C/60 seconds for *t*Boc-protected *tert*-butyl cholate. These exposed films were then developed in $scCO_2$. Electron-beam (e-beam) patterning was performed using a Leica VB6 operating at 100 keV, followed by PEB and $scCO_2$ development. LEO 1550 FESEM was used to characterize the patterns for scanning electron microscopy (SEM) images.

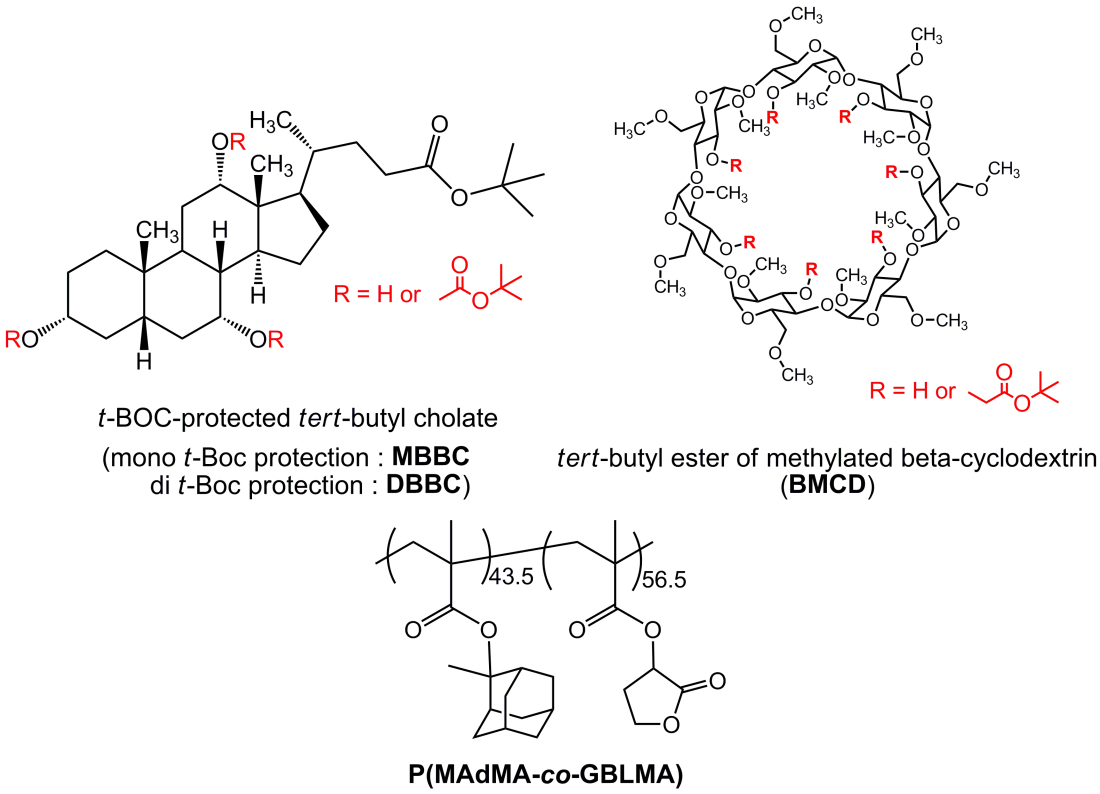

Figure 3.14: Chemical structures of *t*Boc-protected *tert*-butyl cholate, *tert*-butyl ester of methylated β-cyclodextrin, and P(MAdMA-co-GBLMA) [poly(methyl adamantyl methacrylate-co-(γ) butyrolactone methacrylate)].

3.4.3 Results and Discussions

The chemical structures of *t*Boc-protected *tert*-butyl cholate and the *tert*-butyl ester of methylated β-cyclodextrin are depicted in Figure 3.14. The amorphous character of the compounds was established using powder XRD. The results are shown in Figure 3.15. Broad amorphous peaks were observed at a 2θ value of around 18°. Absence of sharp peaks confirmed the glass-forming abilities of the molecules.

The thermal characteristics of the compounds were examined by thermogravimetric analysis (TGA) and differential scanning calorimetry (DSC). TGA

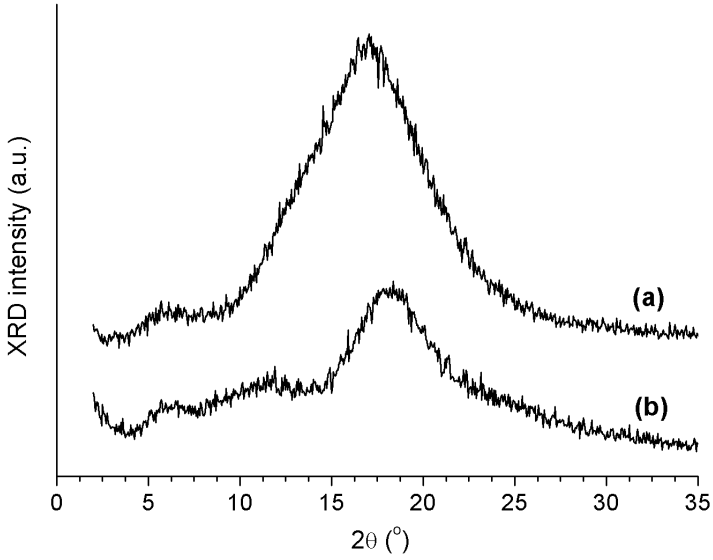

Figure 3.15: XRD analysis of (a) *t*Boc-protected *tert*-butyl cholate and (b) *tert*-butyl ester of methylated *β*-cyclodextrin at room temperature.

showed that all the samples began to decompose around 200 °C, regardless of the degree of functionalization. DSC analysis (Fig. 3.16) revealed that protected methylated *β*-cyclodextrin (**BMCD**) and mono-*t*Boc protected *tert*-butyl cholate (**MBBC**) exhibited Tg's around 125 °C and 113 °C respectively. *t*Boc groups are known to lower glass transition temperatures of materials, but di-*t*Boc protected *tert*-butyl cholate (**DBBC**) still possessed a high Tg of ~100 °C, possibly due to the strong intermolecular hydrogen bonding between the cores.

To investigate the transparency of these molecular glass materials at 193 nm, the optical constants were measured by ellipsometry. Refractive indices and extinction coefficients of *tert*-butyl ester of methylated *β*-cyclodextrin, *t*Boc-protected *tert*-butyl cholate, and the copolymer of 2-methyl-2-adamantyl methacrylate and tetrahydro-2-oxofuran-3-yl methacrylate [**P(MAdMA-co-GBLMA)**], a commercially available 193-nm resist with the chemical structure

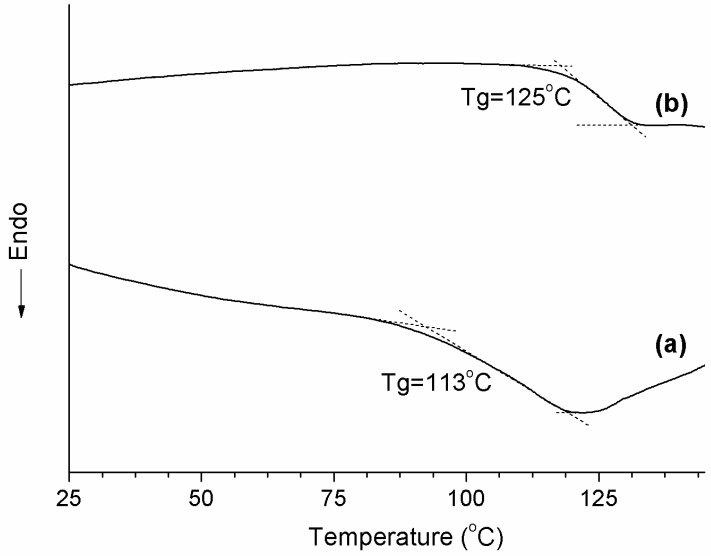

Figure 3.16: DSC analysis of (a) *t*Boc-protected *tert*-butyl cholate and (b) *tert*-butyl ester of methylated β-cyclodextrin.

shown in Fig. 3.14] are plotted in Figure 3.17. The molecular glass resists demonstrated similar optical properties as the 193-nm polymer resist in the deep UV regime.

The well-defined chemical structure of molecular glass resists provides a way to eliminate adverse pattern fluctuation and surface roughness effects caused by variability in dissolution rates among polydisperse polymeric resists.[102] The uniform dissolution rates of molecular glass resists in developers are expected to produce sharp solubility contrast between exposed and unexposed regions and low roughness of final patterns. In this study, the changes in film thickness before and after developing in $scCO_2$ at 40 °C were measured by profilometry and thus dissolution rates were calculated accordingly (Fig. 3.18).

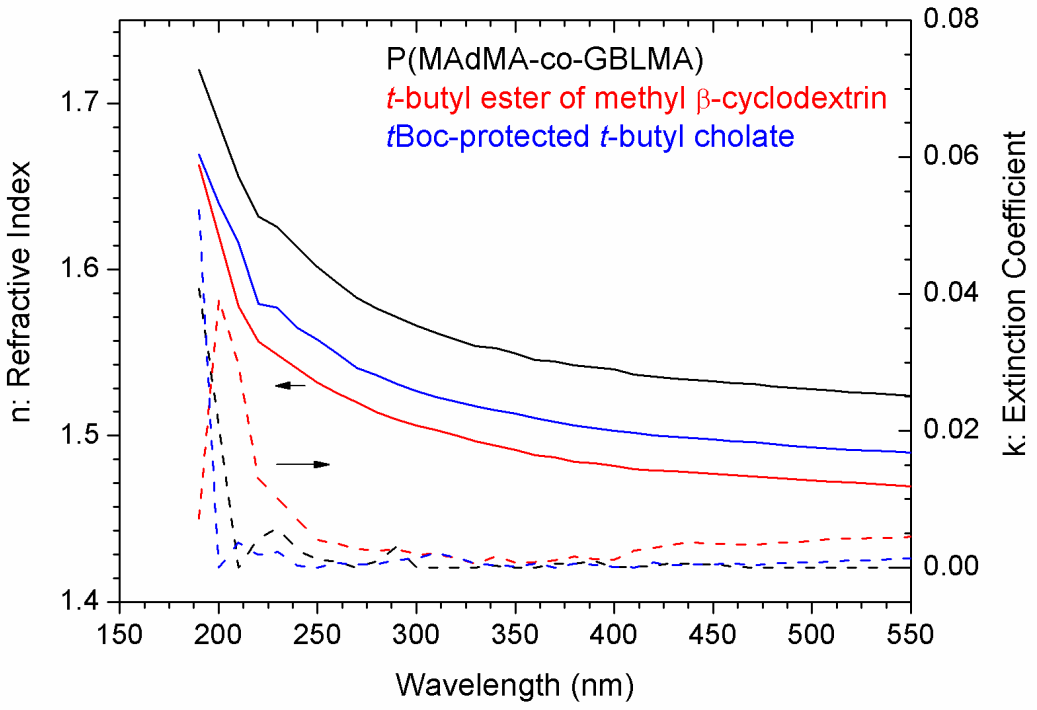

Figure 3.17: Optical constants of P(MAdMA-co-GBLMA), *tert*-butyl ester of methylated *β*-cyclodextrin, and *t*Boc-protected *tert*-butyl cholate.

BMCD showed dissolution rates similar to **MBBC** in the examined $scCO_2$ pressure range, despite the fact that the molecular weight of the former compound is almost twice that of the latter. **BMCD** has a Tg about 10 °C higher than **MBBC**, indicating that stronger intermolecular attractive interactions exist among **BMCD** molecules than among **MBBC** molecules. However, the methyl *β*-CD molecules have all the hydroxyl groups protected with *tert*-butyl ester groups while only one out of the three hydroxyl groups in each *tert*-butyl cholate molecule is protected for **MBBC**. Therefore, the interaction with CO_2 molecules is expected to be stronger for **BMCD** than for **MBBC** because of the larger density of CO_2-soluble functional groups. Thus the strong intermolecular interactions between the resist molecules may counteract the strong interactions

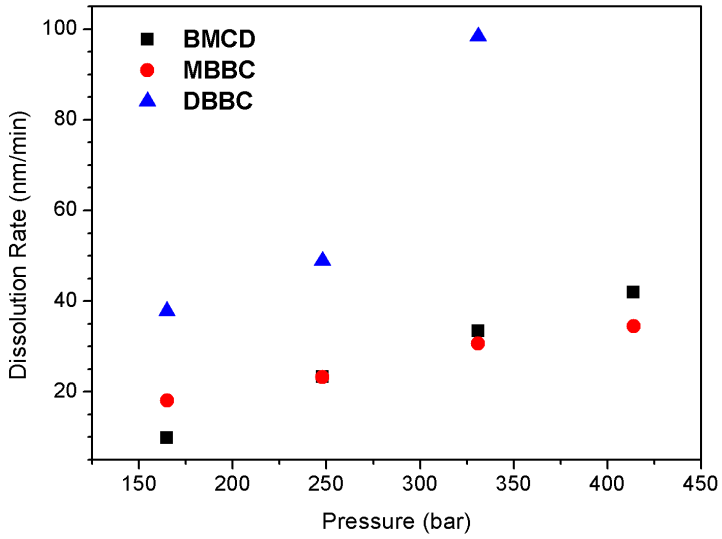

Figure 3.18: Dissolution rates of mono- and di- *t*Boc-protected *tert*-butyl cholates (**MBBC**, **DBBC**) and *tert*-butyl ester of methylated *β*-cyclodextrin (**BMCD**) in $scCO_2$ at 40 °C and varying pressures.

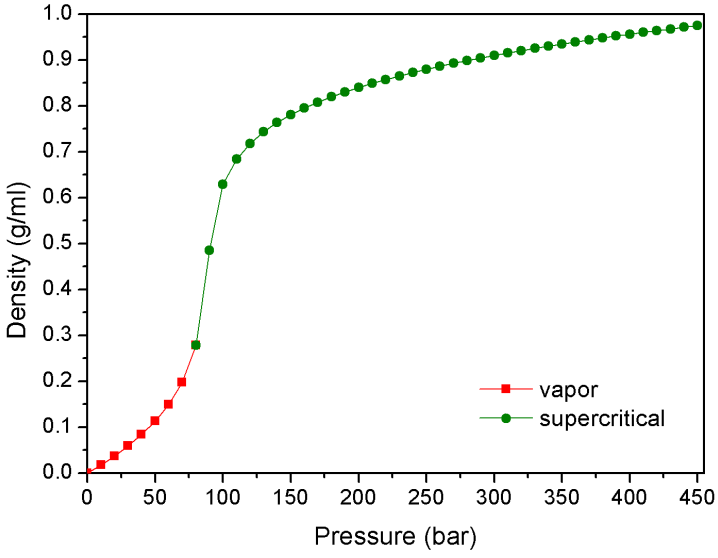

Figure 3.19: Isothermal properties of CO_2 at T = 40 °C.

between CO_2 and the resist molecule, providing the two structurally different molecular glass compounds (**BMCD** and **MBBC**) with similar dissolution behaviors in $scCO_2$.

Another observation is that **DBBC** demonstrated prominently higher dissolution rates than **MBBC** and **BMCD**, especially at higher CO_2 pressure. It might be explained by a larger number of attractive CO_2-resist interactions in **DBBC** which had twice as many CO_2-soluble *t*Boc groups per molecule as in **MBBC**. As shown in Figure 3.19, the density of CO_2 increases by less than 15 % when the pressure increases from 165 bar to 330 bar at 40 °C. During this pressure increase, the dissolution rate increased approximately 240 % for **BMCD**, 70 % for **MBBC**, and 160 % for **DBBC**. The impact of CO_2 pressure on dissolution rate is not the same for different molecular glass resists and even the same molecular core with different protection levels. This might be associated with plasticization levels of the resist films not responding to CO_2 pressure change at the same rate.

Upon exposure to either UV or electron-beam radiation, the molecular glass materials respond by cleaving the acid-labile protecting groups with photogenerated acid during the post-exposure baking step. Contrast curves of photoresists reflect the dependence of photoresist film thickness change on exposure dose after development. Figure 3.20 shows the contrast curves of the molecular glass compounds with UV exposure and $scCO_2$ development. For the *t*Boc-protected *tert*-butyl cholate, the normalized film thickness levels off at almost 0.75 of the original thickness, because the uncleaved *tert*-butyl groups have attractive electrostatic interaction with CO_2 molecules and thus fully *t*Boc-deprotected *tert*-butyl cholate dissolves slightly in $scCO_2$.

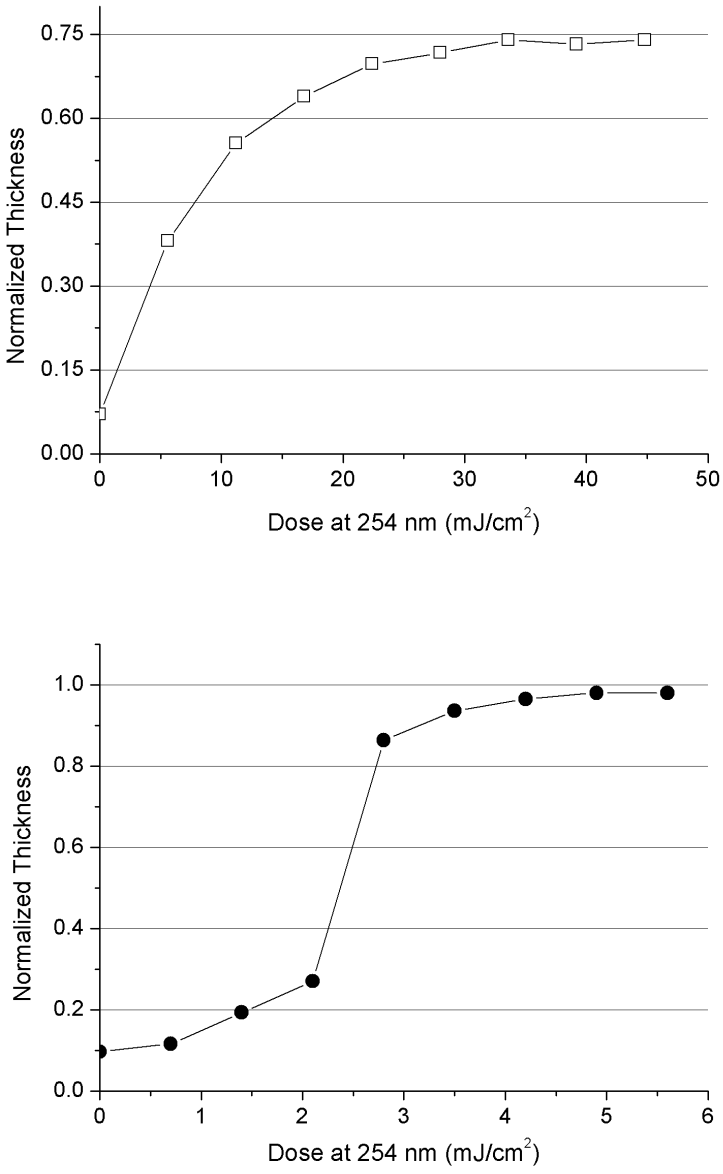

Figure 3.20: Contrast curves for mono-*t*Boc-protected *tert*-butyl cholate (**MBBC**) (upper) and *tert*-butyl ester of methylated β-cyclodextrin (**BMCD**) (lower) after development in $scCO_2$ at 40 °C and 276 bar for 5 minutes.

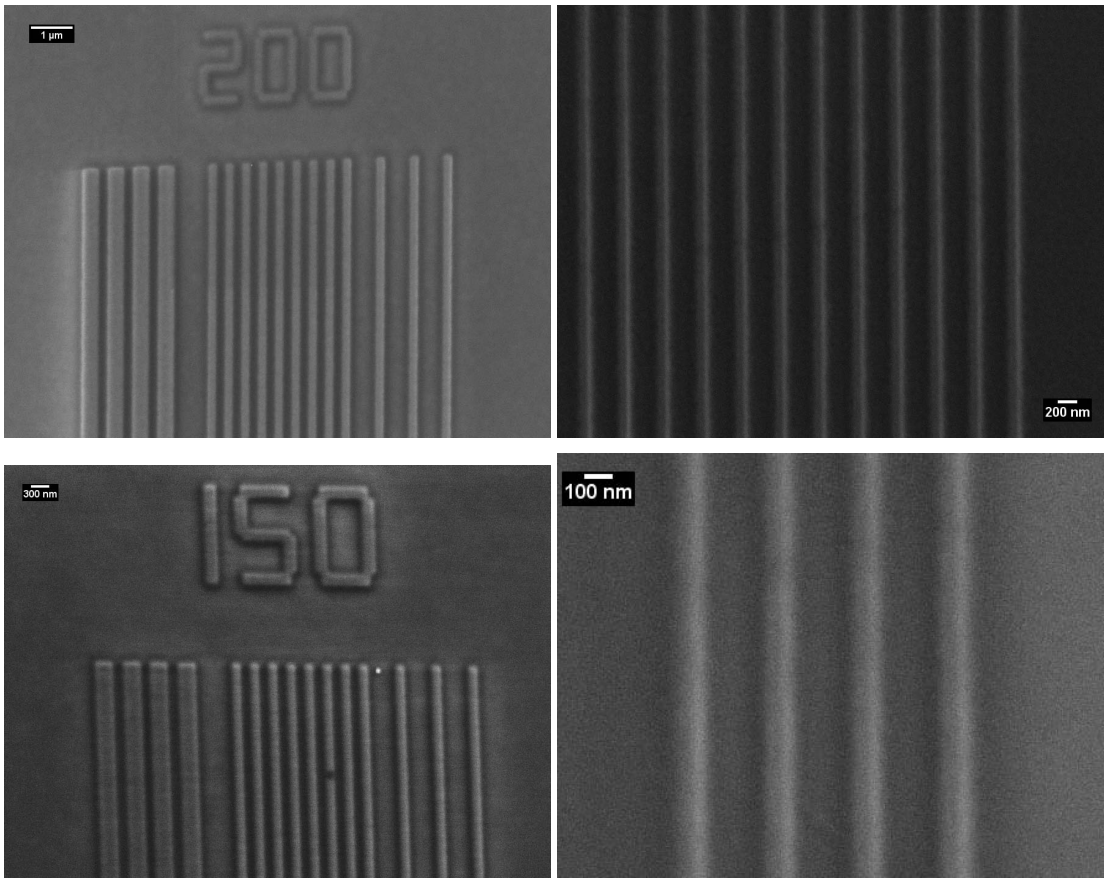

Figure 3.21: SEM images of mono-*t*Boc-protected *tert*-butyl cholate (**MBBC**) (upper) and *tert*-butyl ester of methylated β-cyclodextrin (**BMCD**) (lower) patterned by electron-beam lithography and developed in $scCO_2$.

Following electron-beam patterning, development of resist films in $scCO_2$ was performed at 40 °C and 276 bar for 5 minutes. SEM images of some resist patterns are shown in Figure 3.21. Feature sizes as small as 150 or 200 nm were obtained with the alicyclic molecular resists. These results confirm that high Tg's ensure pattern fidelity with high resolution by preventing plasticization under $scCO_2$ development.

3.5 Conclusions and Future Work

Research progress in supercritical CO_2 development has been presented. An approximation modeling method has been proposed to estimate material solubility in CO_2 for molecular design in the future. Our recent experimental work in the area includes exploring naturally occurring alicyclic cores for CO_2-developable 193-nm molecular glass resists. This work illustrates that combining the concepts of molecular glass resists and scCO_2 development has the potential to improve the performance of photoresist processes while reducing their environmental impact. The compounds tested in the experiments were based on the modeling predictions and demonstrated promising qualities as 193-nm resists. Besides the high glass transition temperatures, they provide additional interesting characteristics. Cholates are known to possess great etch resistance while cyclodextrins can host functional moieties in their cavities to form supramolecular inclusion complexes.[103] Future work along these lines can be explored for resist performance optimization and/or introduction of multifunctional 193-nm photoresists. Other future opportunities in supercritical CO_2 development can be found in exploring more CO_2-soluble functional groups by both modeling and experiments, orthogonal patterning [84] of special materials, and expanding the cosolvent library of CO_2-compatible salts for development of conventional polymeric photoresists [59].

CHAPTER 4

IN SITU FTIR STUDY OF ACID REACTION-DIFFUSION KINETICS IN RESISTS

Understanding acid reaction-diffusion kinetics is crucial for controlling the lithographic performance of chemically amplified photoresists. In this chapter, we study how the molecular architectures of positive-tone chemically amplified molecular glass resists affect the acid reaction-diffusion kinetics during the post exposure bake (PEB) or annealing step. We compare the acid reaction-diffusion kinetics of a common photoacid generator in molecular glass resists with chemical similarity to poly(4-hydroxystyrene), and that are designed with branched and ring architectures. *In situ* Fourier transform infrared (FTIR) spectroscopy methods are used to measure reaction rate, acid trapping behavior, and acid diffusivity as a function of PEB temperature. We find that the acid reaction-diffusion kinetics in molecular glass resists is correlated to the film molar density that in turn depends on the architecture of the molecular glass molecules. These results allow modeling of the latent image formation in molecular glass resists that is critical for pattern feature resolution and line edge roughness. A comparison between experimentally measured and theoretically predicted diffusion lengths in one molecular glass resist system was made. Because little is understood of the fundamentals of acid diffusion in this class of molecular glass resists, this chapter provides critical insight into the molecular design of next-generation photoresists for high-resolution lithography.

[1]Reproduced with permission from J. Sha, J.-K. Lee, S. Kang, V. M. Prabhu, C. L. Soles, P. V. Bonnesen and C. K. Ober, *Chemistry of Materials*, **2010**, 22 (10), pp 3093 - 3098. Copyright 2010 American Chemical Society.

4.1 Introduction to Acid Reaction-Diffusion in Photoresists

Chemically amplified resists (CARs), a concept proposed by Ito, Willson, and Fréchet [6, 8] in 1982, are the current workhorse in photolithography for semiconductor device manufacturing because of their high sensitivity and good patterning performance. Irradiation activates photoacid generators (PAGs) in a CAR and the resulting photoacid molecules subsequently catalyze numerous reactions in a resist film before being trapped or quenched during the post-exposure bake (PEB) step. These photoacids must be mobile enough within the CAR film to decompose a sufficient number of acid-labile protecting groups to achieve a solubility switch in the photoresist. However, excessive acid diffusion leads to image blur and resolution loss.[42, 43, 44, 104] Given the importance of this balance, measurements that quantify photoacid diffusion and the mechanisms of image blur and resolution are crucial to optimize CAR photopatterning.[108, 105, 106, 107, 35, 109, 110] Quantitative methods have been developed to measure photoacid diffusion using numerous strategies.[35, 111, 112, 113, 114, 115, 116, 117, 118, 119, 120] Conventional CARs with polymer-based resist systems appear to have resolution limits, such that critical dimensions of less than 22 nm may not be achieved. Because acid diffusion lengths are now approaching these CD values, acid diffusion remains critical to measure and control for the continued development of materials for next-generation patterning.

Recently, a new category of patterning materials, molecular glass (MG) resists, have attracted great attention as an alternative to polymeric CARs because of their potential to improve line edge roughness (LER) and achieve smaller CD. MG resists are low molar mass glass-forming organic materials and considered

to have some advantages over linear polymers as photoresists. The small molecular size of MGs is believed to give a finer patterning "pixel" size to photoresists in comparison to their polymeric counterparts, which should enable high resolution patterning. This would be enabled by intimate mixing between PAG and molecular resist as determined by solid state nuclear magnetic resonance experiments on bulk blends [121]. Also, because the molecular glass resists have lower molecular mass, they are free of intermolecular entanglement, so less internal stress can build up during the development processes. Image distortion resulting from film stress is thereby reduced for MGs during pattern development. Despite these advantages, acid diffusion still occurs during the PEB step of chemically amplified MG resists and plays as important a role as in polymeric photoresists [39, 122]. In this study, we try to understand the photoacid catalyzed reaction-diffusion kinetics in different types of MG resist materials for next-generation lithography.

MG resists investigated to date have structures including spiro [123], ring [86, 90, 124, 125, 126], and branched architectures [93]. In this chapter, we focus on four representative MG structures of both the ring and branched structures to investigate the effect of molecular architecture on acid reaction-diffusion kinetics. Two calix[4]resorcinarene derivatives [86, 90, 125] (**CM4R** and **CHPB**) and two phenolic MGs [89, 93] (**HHPB** and **CR15**) were fully protected with *tert*-butoxycarbonyl (*t*Boc) groups and used as the resist materials in this work (Fig. 4.1). The MG resists possess structural similarity to novolac or poly(hydroxystyrene) (PHOST) based resists due to the incorporation of rigid phenyl rings. The glass transition temperatures for these materials are between $\approx$ 80 ^{o}C and $\approx$ 90 ^{o}C in the bulk form, so processing temperatures among the MGs are not substantially different. As the *t*Boc groups are deprotected by acids

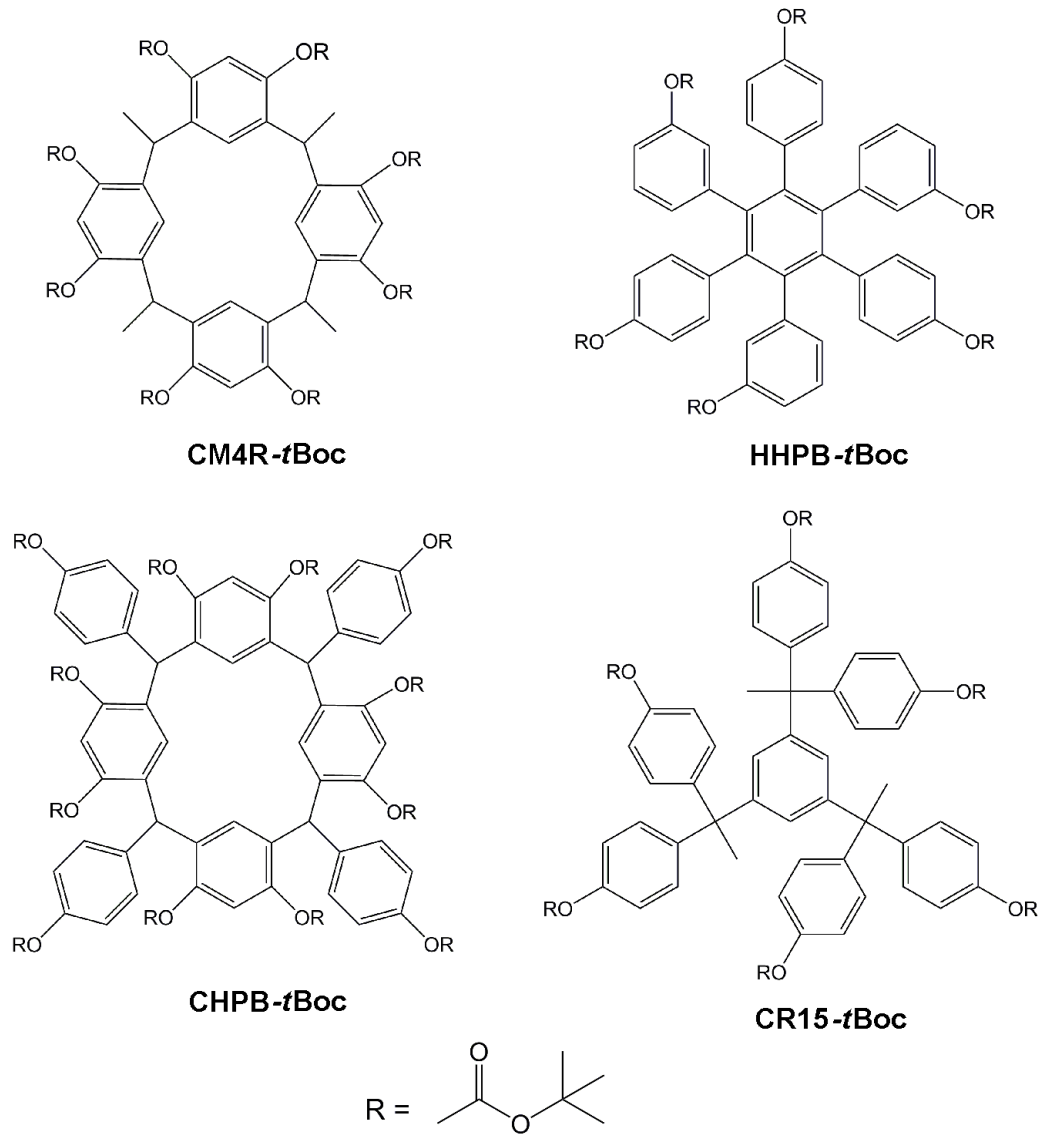

Figure 4.1: Chemical structures of the molecular glass resists studied in this chapter and the corresponding labels used to identify these compounds.

during the post-exposure bake (PEB) step and the average degree of deprotection reaches a critical concentration, the MG resist film is transformed from insoluble to soluble in an alkaline developer (positive-tone development).

4.2 *In Situ* FTIR and Reaction-Diffusion Model

In situ FTIR methods are used to measure the *t*Boc group deprotection kinetics and thus acid reaction-diffusion kinetics in exposed MG resist films during PEB.[39, 111, 122] We have applied the strategy of using a bilayer film structure with a PAG-loaded MG resist layer on top of a PAG-free MG layer.[39, 111, 122] This approach mimics an ideal lithographic line-edge that forms a well-defined step gradient of photoacids after flood ultraviolet (UV) light exposure. A soft-contact film transfer method using a poly(dimethylsiloxane) (PDMS) stamp was utilized for bilayer sample fabrication as described elsewhere [39, 111, 122] (Fig. 4.2a). This approach proved to be more convenient than double spin coating methods [35] which limit the use of the same spin casting solvents and/or the same resist materials for both layers. Single layers of PAG-loaded MG resists were prepared, exposed and put on a preheated hot stage for *in situ* FTIR measurements. These experiments estimate the reaction kinetics constants (k_P and k_T) for each PEB temperature from the measured time-dependent deprotection level ϕ. Subsequent *in situ* FTIR measurements on bilayer samples provide the diffusion coefficient D_H and the reaction kinetics constants (k_P and k_T) through simultaneous model fitting. Distinct reaction-diffusion kinetics performance was observed for each MG. Subsequently, the PEB bilayer samples were then developed in an aqueous base solution to determine the film thickness change and surface roughness of the bottom layers that relate to the CD and LER of MG resists in a true lithographic interface.

A reaction-diffusion model [39, 122] was used to describe the acid-catalyzed deprotection and the acid diffusion/trapping during the PEB (Equations 4.1 and 4.2). In the differential equations, H is the acid concentration and ϕ is *t*Boc de-

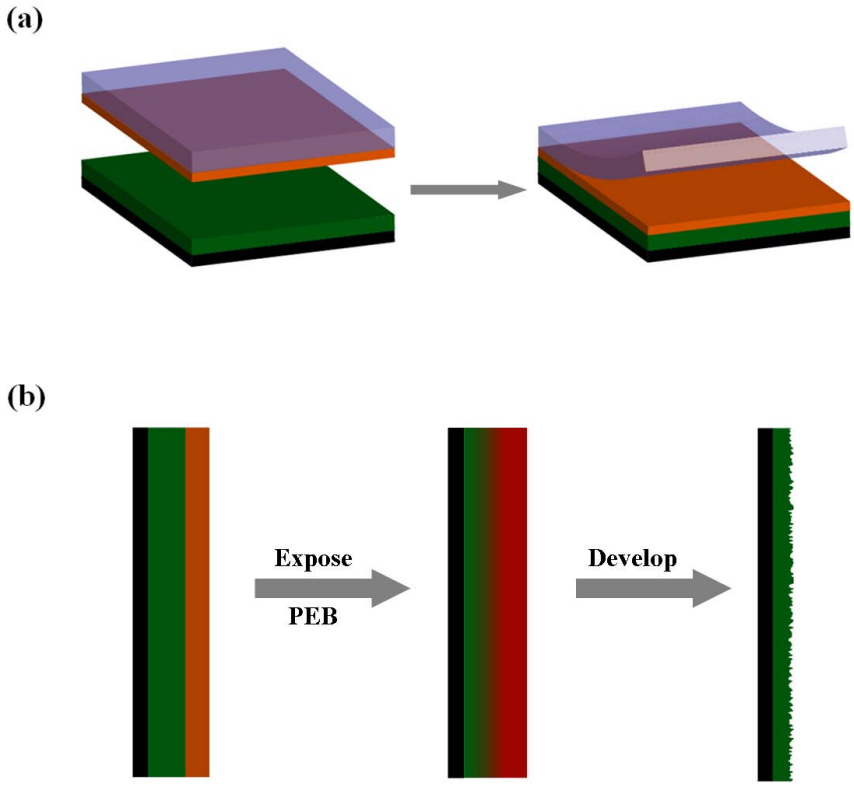

Figure 4.2: (a) Illustration of MG bilayer sample preparation: stamping PAG-loaded top layer (orange) onto PAG-free bottom layer (green) and peeling off PDMS stamp after the stack cools down. (b) Mimicking ideal exposure edge with a bilayer structure and processing of MG bilayer: exposure, PEB and development.

protection level of the MG resist which was quantified by the C=O stretching vibrational spectroscopic band around 1760 cm^{-1}. The reaction rate constant k_P, the trapping rate constant k_T and the acid diffusion coefficient (D_H) are the three kinetic parameters that were measured and compared in this study. The relationship between the initial acid concentration H and PAG loading concentration $[PAG]$ can be described as $H = [PAG](1-e^{C \cdot E})$ where C is Dill's parameter and E is the exposure dose. Because we exposed all the PAG-loaded MG resist films at high doses and essentially all the PAGs were activated, the initial acid

concentration H is considered the same as the PAG loading concentration.

$$\frac{\partial \phi}{\partial t} = k_P \cdot H \cdot (1 - \phi) \tag{4.1}$$

$$\frac{\partial H}{\partial t} = D_H \cdot \nabla^2 H - k_T \cdot H \cdot \phi \tag{4.2}$$

4.3 Experimental

4.3.1 Materials

1,3,5-Triacetylbenzene was purchased from TCI America and used as received. 4-Hydroxylbenzaldehyde, resorcinol, aldehyde, BBr_3 (1 M solution in dichloromethane), 3-iodoanisole, triphenylsulfonium perfluoro-1-butanesulfonate (TPS-PFBS), anhydrous tetrahydrofuran (THF) and propylene glycol monomethyl ether acetate (PGMEA) were purchased from Sigma-Aldrich and used without further purification. 4-Ethynylanisole and $Co_2(CO)_8$ were purchased from AlfaAesar and used as received. Di-tert-butyl dicarbonate was purchased from either Fluka or Aldrich and used as received. Dioxane was dried over Na/benzophenone and distilled under reduced pressure. Commercially available AZ 300 MIF was employed as the developer (0.26 N tetramethylammonium hydroxide in water, TMAH). Sylgard 184 silicone elastomer kit was purchased from Dow Corning and used to make polydimethylsiloxane (PDMS) stamps.

4.3.2 Synthesis of molecular glass photoresists

Tetra-C-methylcalix[4]resorcinarene (**CM4R**) [121, 125], C-4-hydroxyphenylcalix[4] resorcinarene (**CHPB**) [86], hexa-(3 or 4-hydroxyphenyl)benzene (**HHPB**) [89], 1,3,5-tri(1,1-di(4-hydroxyphenyl)ethyl)benzene (CR15) [93], and their fully *tert*-butoxycarbonyl (*t*Boc)-protected molecular glass resists were prepared according to the procedures in the literature. The compounds were characterized by proton and carbon NMR, and chemicals shifts were consistent with those reported in the literature.

Of specific note, the parent resorcinarene compound **CM4R** was synthesized following literature procedures and purification methods known to afford the pure all *cis* or "*ccc*" isomer (which is the cup-shaped isomer). Our 1H and 13C NMR spectral data on the tetra-C-methylcalix[4]resorcinarene were in agreement with the literature NMR spectral data [90] in the manuscript reported for the *ccc* isomer as well as the NMR data of reference [126]. Because the parent **CM4R** is all *cis*, the *t*Boc derivatives will also be all *cis*. However, the parent **CHPB** was not purified as **CM4R** and is believed to be a mixture of *cis* and *trans* isomers.

4.3.3 Sample preparation

Single layers and bilayers of each MG resist were prepared. Resist solutions were used containing (3 to 5) % by mass MG in PGMEA. The photoacid generator, TPS-PFBS, was added to the solution at a concentration of 5 % by mass of the MG for both the single layer samples and the top layer of the bilayer samples. For single layer samples, solutions of MG resist and TPS-PFBS were spin-cast

on Au-coated silicon substrates at 2000 rpm (209 rad/s) and at a PEB temperature of 90 °C for 60 s. The final film thicknesses were generally 50 nm to 100 nm depending on the resist mass fraction. A PDMS stamping technique [39, 122] was used to create MG resist bilayers with PAG-loaded resist films at the top and PAG-free films at the bottom. The bottom layers of bilayer samples were prepared on Au-coated silicon substrates from PAG-free solutions in the same way as single layer samples. Resist solutions containing PAG were spin-cast on PDMS substrates and then stamped onto prepared PAG-free resist films at 75 °C for 20 sec. PDMS stamps were peeled off after the stacks cooled down. The resist bilayers were baked again at 75 °C for 60 sec to remove residual solvents.

4.3.4 Exposure and development

An Oriel UV exposure system was used for the reaction kinetics studies at a dose of ≈ 250 mJ/cm^2 with 248 nm broadband radiation. The samples prepared for additional development and AFM characterization were exposed with an ABM contact aligner at a dose of ≈ 250 mJ/cm^2 with 254 nm. At these exposure doses, all the photoacid generators were activated, so the initial acid concentration may be calculated using the molecular masses of the resist components. After PEB, bilayer samples were developed in a commercial developer AZ 300 MIF for 60 sec, rinsed with de-ionized water and blown dry with N_2.

4.3.5 Characterization

Thermogravimetric analysis was performed using a TA 500 TGA with a heating rate of 10 ^{o}C/min under dry N_2 atmosphere. Glass transition temperatures were measured on a TA 1000 DSC using repeated heat/cool cycles at 10 ^{o}C/min between -50 ^{o}C and 130 ^{o}C. MG resist film thicknesses were measured with a J.A. Woollam IR spectroscopic ellipsometer. All the Fourier transform infrared (FTIR) spectra were collected using polarization-modulation infrared reflection-absorption spectroscopy (PM-IRRAS) at 8 cm^{-1} resolution on exposed resist films. Silicon wafers coated with 100 nm thick Au were used as substrates for MG samples to increase IR reflectivity in all measurements and mounted on a pre-heated hot stage through vacuum contact. The uncertainty in deprotection quantification is $\approx$ (0.01 to 0.02). X-ray reflectivity measurements were carried out on a Philips X'Pert MRD diffractometer with fine focus x-ray tubes with a wavelength of 1.54 Å. Atomic force microscopy (AFM) was performed on developed bilayer samples with a Veeco Dimension 3100 in tapping mode.

4.4 Results and Discussions

Single layers of PAG-loaded MG resists were prepared and exposed using a sufficiently high exposure dose of UV light to activate all the photoacid generators in the films. Immediately following exposure, sample films were placed on the pre-heated hot stage of the FTIR spectrometer for in situ measurement of deprotection levels of *t*Boc groups. From the time-dependent deprotection level $\phi(t)$, the reaction rate constant k_P and acid trapping constant k_T were estimated by the model for each PEB temperature.

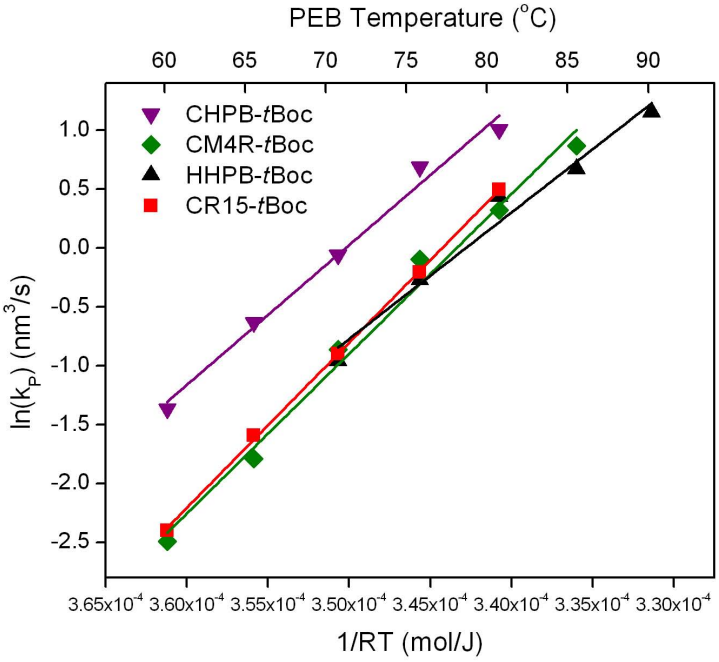

(a)

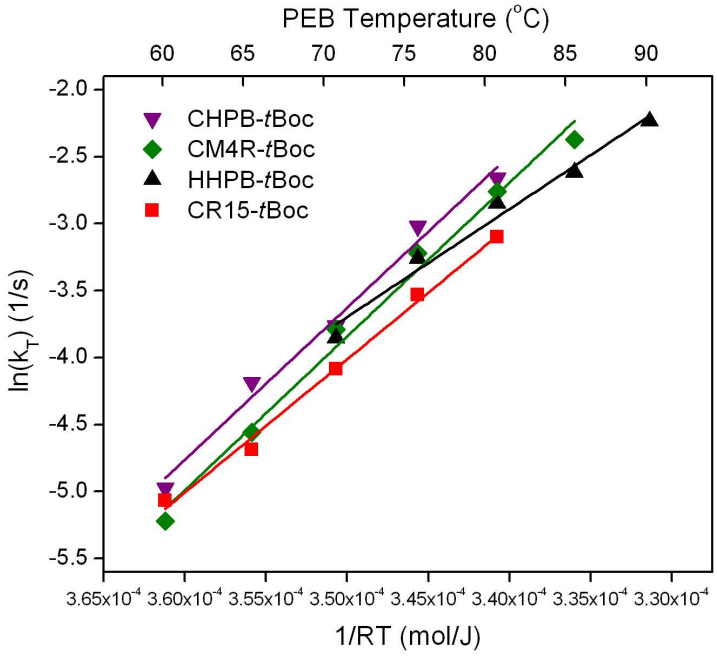

(b)

Figure 4.3: (a) Reaction rate constants k_P's and (b) acid trapping rate constants k_T's for the systems of TPS-PFBS and the four molecular glasses at varying PEB temperatures. The solid lines are fitted curves from Arrhenius model.

Table 4.1: Summary of fitted prefactors A's and activation energies E_a's for k_P, k_T, and D_H of TPS-PFBS in the MG resists.

	k_P		k_T		D_H	
	A	E_a(mJ/mol)	A	E_a(mJ/mol)	A	E_a(mJ/mol)
CHPB-*t*Boc	42 ± 2	112 ± 7	36 ± 2	114 ± 7	33 ± 2	91 ± 5
CM4R-*t*Boc	47 ± 3	136 ± 7	36 ± 2	115 ± 6	44 ± 2	125 ± 7
HHPB-*t*Boc	37 ± 3	107 ± 10	25 ± 2	81 ± 7	41 ± 4	125 ± 11
CR15-*t*Boc	48 ± 1	140 ± 2	31 ± 1	100 ± 4	44 ± 3	127 ± 8

The exposure and measurement conditions for the bilayer samples were the same as those used for the single layers. In the bilayer samples, the acids generated in the top layer deprotect the MG resist molecules in the neighboring regions and further diffuse into the PAG-free bottom layer during PEB. The time-dependent deprotection level ϕ of the bilayer samples is fit simultaneously to obtain k_P, k_T, and the acid diffusion coefficient D_H.

The resulting reaction rate constants and acid trapping rate constants for PEB temperatures varying from 60 °C to 90 °C are shown in Figure 4.3 (a) and (b) respectively, for TPS-PFBS PAG with the four MG resists. The **CM4R-*t*Boc**, **HHPB-*t*Boc** and **CR15-*t*Boc** systems show no substantial differences in the reaction rate constants while those for **CHPB-*t*Boc**/TPS-PFBS are significantly higher. The reaction rate constants increase with PEB temperature for each MG resist. Because the PEB temperatures are all below Tg, the temperature dependence of k_P can be described by an Arrhenius equation $ln(k_P) = A - E_a/RT$ where E_a is the activation energy, A is a prefactor, T is PEB temperature and R is the universal gas constant. The fitted A and E_a values of the reaction rate constants of all resist systems are summarized in Table 4.1 with uncertainty estimated as one standard deviation from the mean. The acid trapping rate constants k_T don't differ significantly among the resist systems as a function of temperature, while

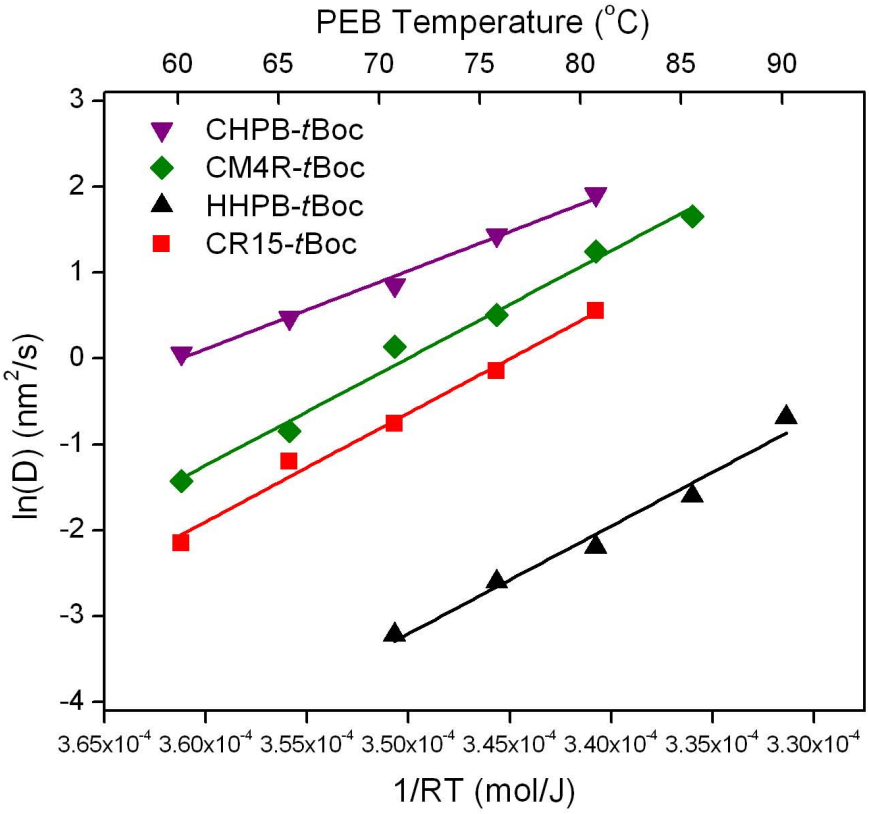

Figure 4.4: Diffusion coefficients D_H's of TPS-PFBS in the four molecular glass resists at various PEB temperatures. The solid lines are fitted curves from Arrhenius model.

significant and systematic differences in acid diffusivity were observed among different MG architectures. The acid diffusivity D_H is the lowest in **HHPB-*t*Boc**, moderate in **CR15-*t*Boc** and **CM4R-*t*Boc**, and the highest in **CHPB-*t*Boc**. The temperature dependence of both k_T and D_H also follow the Arrhenius equations with prefactors A's and activation energies E_a's summarized in Table 4.1.

Because all the *in situ* FTIR measurements were conducted below the Tg's of the MGs, the transport process was expected to follow an Arrhenius dependence and it should depend on the mass density, packing and free volume in the MGs. The mass density of the thin films was measured by X-ray reflectivity

Table 4.2: Mass/molar densities and protecting group concentrations of molecular glass resist thin films.

	CHPB-*t*Boc	**CM4R-*t*Boc**	**HHPB-*t*Boc**	**CR15-*t*Boc**
mass density (g/cm^3)	1.117	1.092	1.124	1.114
molar density (mol/cm^3)	5.427×10^{-4}	8.116×10^{-4}	9.128×10^{-4}	8.468×10^{-4}
protecting group conc. (nm^{-3})	3.922	3.910	3.298	3.060

from the critical-edge region (Table 4.4) using MG films without any additives. The mass density was converted to molar density using the known chemical composition. The trend of molar densities is **HHPB-*t*Boc** > **CR15-*t*Boc** > **CM4R-*t*Boc** > **CHPB-*t*Boc**, which shows an opposite trend to the acid diffusivity in the studied MG resist systems D_H(**HHPB-*t*Boc**) < D_H(**CR15-*t*Boc**) < D_H(**CM4R-*t*Boc**) < D_H(**CHPB-*t*Boc**). This observation follows concepts provided by free volume theory [127], such that the more free volume present in a resist film, the more freely acid molecules can "hop" and diffuse. Free volumes in resist films can be experimentally inferred from mass/molar densities. According to energy minimization modeling using the MM2 method, all the MG molecules in this study are individually estimated to be approximately 2 nm in size. Therefore, a higher molar density can be translated into less free volume in the resist system or closer packing of resist molecules. For example, the relative planarity of **HHPB-*t*Boc** molecules can contribute to a denser packing configuration while **CHPB-*t*Boc** and **CM4R-*t*Boc** molecules are ring-shaped and may leave more voids among resist molecules such as within the calix[4]resorcinarene cavity and as a result are less dense.

The protecting group concentrations can also be calculated by multiplying MG molar densities with the number of protecting groups per molecule. With a higher density of protecting groups, then after deprotection there are more

hydroxyl groups per unit volume. Therefore, this increases the probability that the photoacids interact with the hydroxyl groups and become trapped instead of moving on to deprotect more *t*Boc groups. The trapping constants in Figure 4.3(b) appear clustered but there is a noticeable trend at each PEB temperature: k_T(**CHPB-*t*Boc**) > k_T(**CM4R-*t*Boc**) > k_T(**CR15-*t*Boc**), which is consistent with the trend in protecting group concentrations (Table 4.4): **CHPB-*t*Boc** > **CM4R-*t*Boc** > **CR15-*t*Boc**. A crossover between k_T(**HHPB-*t*Boc**) and k_T(**CM4R-*t*Boc**) was observed and the difference in k_T cannot be explained just by protecting group concentrations. There may be additional mechanisms dominating in the case of **HHPB-*t*Boc** but it is not clear at the moment.

From the above results, we can see that the acid diffusivities in the MG resist systems show apparent variances while the reaction and trapping processes are not widely different. Therefore, the choice of a MG resist system may not be able to control reactivity but only acid diffusivity. Both acid reactivity and diffusivity in CARs are required, however, to control latent image and resolution. Therefore we demonstrate such effects with reaction-diffusion kinetics modeling in one resist system and compare with the experimental diffusion lengths determined by the difference in film thickness before and after development.

In another set of experiments, separate sets of bilayer samples were exposed, post exposure baked at 75 °C for 30 sec, 60 sec, 120 sec and 180 sec and then developed with AZ 300 MIF. A representative result of the thickness loss and surface roughness for **CR15-*t*Boc** bottom layer are plotted in Figure 4.5. As the PEB time increased, more photoacids diffused from the top to the bottom layer resulting in a higher deprotection level of *t*Boc groups in the bottom layer and thus larger film thickness loss after development. The experimental diffu-

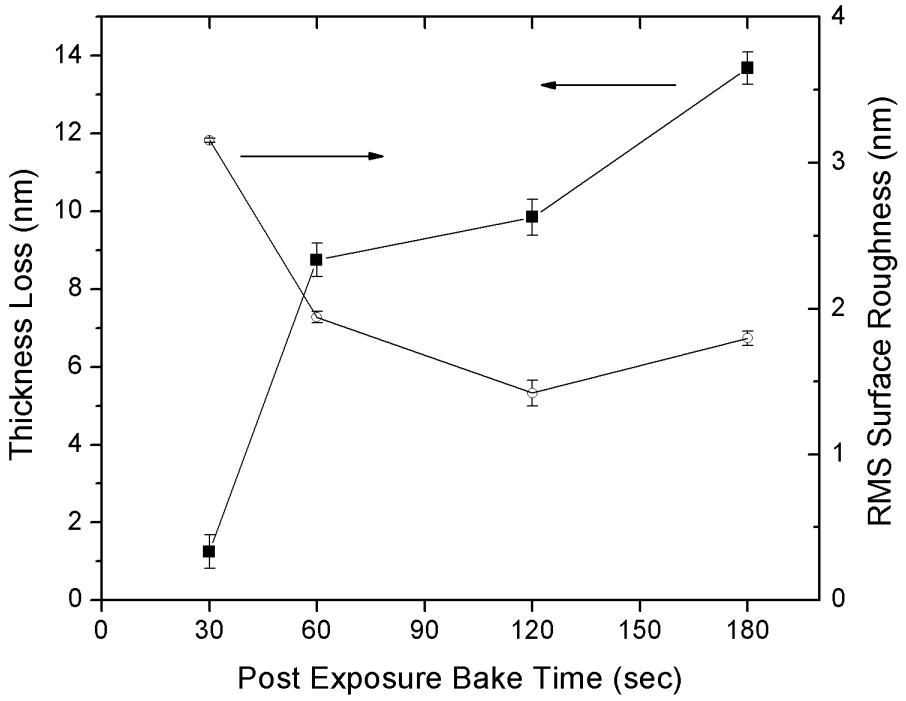

Figure 4.5: Resist film thickness loss (solid squares) and surface roughness (open circles) of the bottom layer of a **CR15-*t*Boc** bilayer sample after development. The change in film thickness, or thickness loss, is a measure of the acid diffusion length (Ld).

sion length, which is the difference in thickness between the initial bottom layer thickness and final developed thickness, was measured to be 1.3 nm, 8.7 nm, 9.8 nm, and 13.7 nm as PEB time increases from 30 sec to 180 sec. The measured surface root-mean-square (rms) roughness of the developed bottom layer dropped to the lowest value of 1.42 nm (PEB time of 120 sec) and slightly increased to *ca.* 1.80 nm at 180 sec of PEB.

The reaction-diffusion process in the **CR15-*t*Boc** resist system was simulated with the kinetic model mentioned earlier using the measured parameters (k_P, k_T, D_H) at a PEB temperature of 75 °C (Fig. 4.6). The deprotection level of **CR15-*t*Boc** was measured to be 37.5 % for solubility switching to occur and

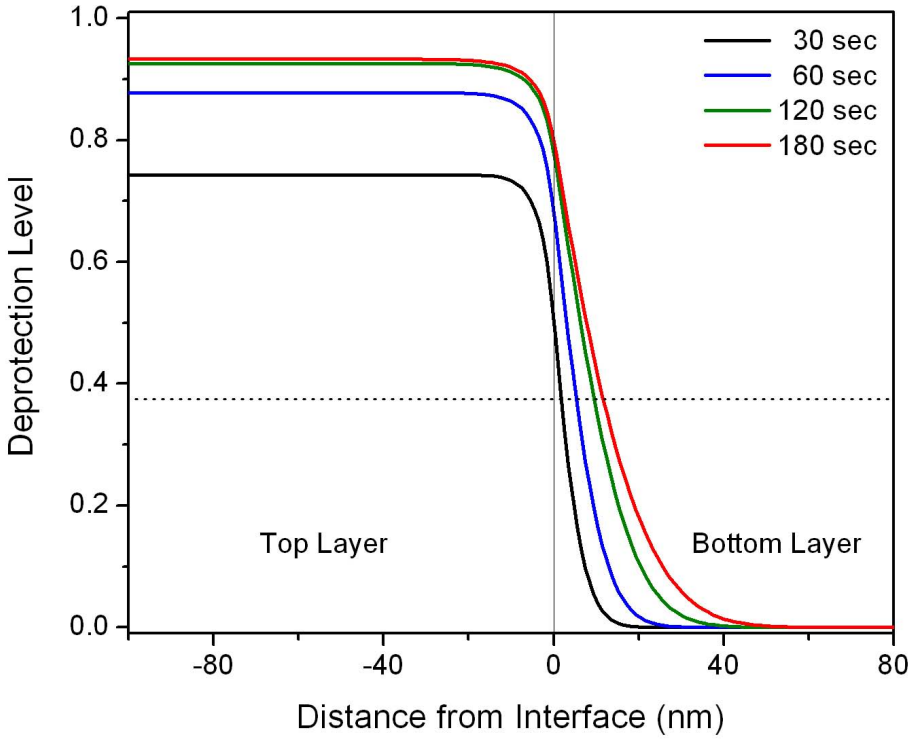

Figure 4.6: Calculated deprotection profile of **CR15-*t*Boc** at 75 °C PEB temperature for various PEB times. The dotted line marks the deprotection level at solubility switch of **CR15-*t*Boc** in the developer.

thus the simulated diffusion length was determined to be 1.5 nm, 5 nm, 9 nm, 11 nm respectively for 30 sec to 180 sec of PEB, which shows excellent agreement with the experimental data. On the other hand, the slope of the diffusion front shows a monotonic decrease as PEB time increases while the experimental surface roughness shows a slight minimum at PEB time of 120 sec. A recent theoretical study showed that post-development line edge roughness of the exposure edge is inversely proportional to the latent image log slope (LILS) [128], thus a larger deprotection level gradient at the solubility switch corresponds to lower surface roughness of the developed bottom layer. The measured surface roughness of **CR15-*t*Boc** does not agree with the trend of deprotection level

gradient at solubility switch, although the differences are small. In this case, the ideal model does not fall within the experimental data. However, there are many aspects that remain critical for final roughness, such as chemical composition heterogeneity [117] and development mechanism.

Previous efforts using AFM images of latent images of 13.5 nm extreme-ultraviolet light (EUV) exposed polymer and **CM4R** photoresists show topographic features related to the deprotection level of the resist. Comparison of latent image LER for a polymeric and molecular glass (**CM4R**) photoresist with an identical photoacid generator exhibited similar dependence on the deprotection gradient. The latent images of features as small as 20 nm were clearly resolved by AFM over a wide range of exposures despite these features not appearing after development.[130] Therefore, development process and development contrast should be an area of increased attention, perhaps this is a future role of negative-tone development with molecular resists.

4.5 Conclusions and Future Work

We have demonstrated a detailed study of acid reaction-diffusion kinetics behavior of four MG photoresists. While reactivity and trapping of acids did not show significant differences among the MG resist systems, acid diffusivity varied systematically with resist architecture and molar density. Photoacids generated in the ring-shaped **CHPB-*t*Boc** resist system was found to have both the highest reactivity and the highest acid diffusivity compared to the other MG resists used in this study. A higher reaction rate is beneficial because for a given PEB time it enables a larger extent of deprotection to occur that favors increased

trapping; therefore, **CHPB-*t*Boc** didn't show patternability inferior to the other MG resists [129]. We have also provided a hypothesis of how molecular architectures of the MGs impact acid kinetics during PEB. This study is the first attempt at a comprehensive characterization of structurally different MG resists with predictions of their lithographic performance.

APPENDIX A

MICROFABRICATION BY TWO-PHOTON LITHOGRAPHY

A.1 Introduction to Two-Photon Lithography

Although two-photon absorption was predicted as early as 1931 [131], it was experimentally observed immediately after the invention of lasers [132]. A significant application of the technology has been found in multiphoton microscopy in the biosciences.[133] Although two-photon polymerization was first reported in 1965 [134], it was not until the late 1980s that noticeable effort was devoted to developing three-dimensional lithography based on two-photon absorption.

Three-dimensional micro- and nano-scale structures have numerous applications in photonics [135], microfluidics [136, 137], tissue engineering [138, 139], chemical detection [140, 141], energy and data storage [142, 143, 144], and as catalyst supports [145]. The fabrication techniques include layer-by-layer photolithography [146, 147], nanotransfer printing [148], micro-stereolithography [149], colloidal self-assembly [150], direct ink writing [151, 152], interference lithography [153, 154], proximity-field lithography [155], and two-photon lithography [156]. Two-photon lithography stands out as the only real 3D direct write patterning approach that can fabricate structures of arbitrary shapes and also eliminate defect creation during fabrication.

Two-photon lithography is based on localized two-photon absorption and activation of photoinitiators or photoacid generators which subsequently trigger chemical reactions in the photosensitive patterning material. Two-photon absorption is a nonlinear optical process first reported by Kaiser and Garrett

in 1961.[132] The rate of two-photon absorption is proportional to the square of the light intensity, so that the near-infrared laser source light is strongly absorbed only at the focal point within the photosensitive material. (Near-infrared light undergoes little absorption and scattering in most photosensitive materials and thus gives rise to a deep penetration of light into the materials.) At the focal point, photoinitiators or photoacid generators in the photosensitive material absorb two near-infrared photons simultaneously in a single quantum event to produce an excitation equivalent to the absorption of a single ultraviolet photon possessing twice the energy and thus induce subsequent chemical reactions in the patterning material. The quadratic intensity dependence of two-photon absorption allows for confinement of the patterning to sub-micron dimensions, beyond the diffraction limit of light.

Two-photon focal volume approximations based on Gaussian functions fit to the integral representation of the electric field near the focus of a diffraction-limited focus are obtained from the formalism of Richard and Wolf [157] and displayed in Figure A.1 where ω is the $1/e$ radius, ω_{xy} and ω_z are lateral and axial radiuses respectively, λ is the laser beam wavelength, NA is the numerical aperture of the objective lens, and n is the refractive index of the working media of the lens. The illumination point spread function, IPSF(x,y,z), describes intensity around the laser beam focus, and in two-photon absorption only $IPSF^2$ is needed to define the true optical resolution. As shown in Figure A.1, the imaging voxel in two-photon lithography is a prolate spheroid with the axial radius larger than the lateral radius.

Besides $IPSF^2$, patterning resolution of two-photon lithography is also dependent on exposure dose [158] and special treatments such as introduction of

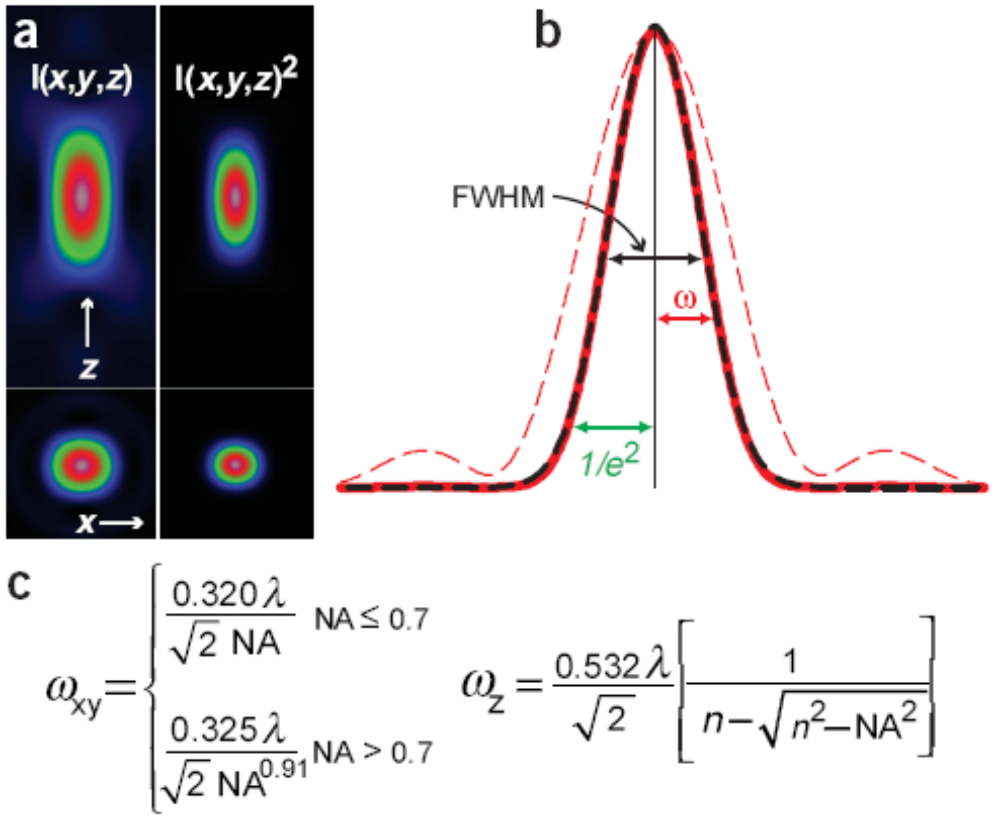

Figure A.1: The two-photon excitation volume. (a) Axial and lateral views of IPSF and IPSF^2. (b) Axial profile $(0, 0, z)$ of IPSF (dashed red) and IPSF^2 (solid red). (c) Equations for calculating the $1/e$ widths (ω) of the lateral (xy) and axial (z) intensity-squared profiles.[133] Reprinted by permission from Macmillan Publishers Ltd: Nature Biotechnology, "Nonlinear magic: multiphoton microscopy in the biosciences", Vol. 21, pp1369-1377. Copyright 2003.

radical quenchers [159] and controlled post-fabrication shrinkage [160]. The best pattern resolution achieved so far with two-photon lithography is 23 nm.[158]

Two-photon lithography has been utilized to fabricate micro-devices for mechanical [161], electrical [162], microfluidic [163], and photonic [164] applications. A three-dimensional spiral-architecture photonic crystal was successfully fabricated by two-photon lithography.[164] Photonic crystals, also known as

photonic band gap materials, are periodic dielectric structures that forbid propagation of electromagnetic waves in a certain frequency range. They can be engineered to manipulate the flow of light for emerging applications such as telecommunication and photonic computing. Since two-photon lithography is a point-by-point direct-write technique, the majority of photonic crystals are fabricated by other more time efficient methods such as interference lithography and colloidal self-assembly. However, two-photon lithography offers a facile solution to introducing defects of arbitrary shapes inside photonic crystals. An example is discussed in the following section.

A.2 Three-Dimensional Patterning Inside Photonic Crystals

This section discusses our attempts at patterning three-dimensional polymer structures inside an inverse-opal C-dot template, a porous photonic crystal.

As mentioned in the previous section, photonic crystals are periodically structured optical materials controlling the flow of photons in a similar way as semiconductor crystals controlling the motion of electrons. Applications of photonic crystals can be significantly broadened when specially designed defects are fabricated in these materials. Engineered defects break the symmetry in photonic crystals and introduce light modes with frequencies in the photonic band gap. Therefore, light at these frequencies can be localized at point defects but propagate along line defects inside photonic crystals. In this section, two-photon lithography is demonstrated as a convenient method to pattern polymers three-dimensionally inside an inverse-opal C-dot template, a porous photonic crystal.

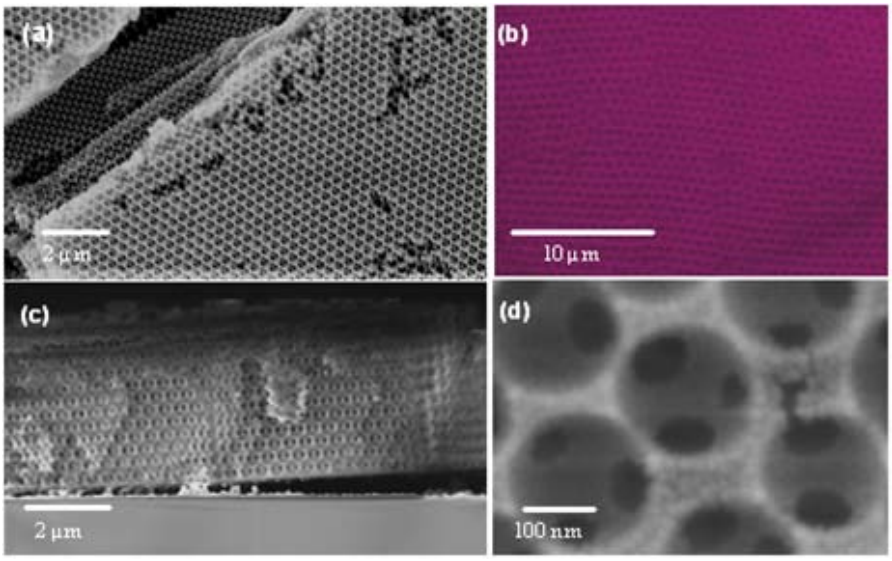

Figure A.2: (a)(c)(d) SEM images and (b) confocal image of an inverse-opal C-dot template. Courtesy of Poorna Praveen Rajendran in Prof. Chekesha Liddell's group at Cornell University.

Core-shell fluorescent silica nanoparticles, also known as Cornell-dots or C-dots, were synthesized and provided by Prof. Ulrich Wiesner's group at Cornell University. C-dots are basically nanoparticles with fluorescent dyes encapsulated in silica shells. Prof. Chekesha Liddell's group also at Cornell convectively co-assembled the C-dots with some monodisperse polystyrene microbeads, which resulted in a face-centered cubic (fcc) structure of polystyrene beads with the voids closely packed with C-dots. After plasma etching away the polystyrene beads, an inverse-opal C-dot template (Fig. A.2) remained on the substrate which is usually silicon or glass. This template is an example of active photonic crystals. Our goal is to manufacture polymer structures of arbitrary shapes (defects) inside the template (photonic crystal) by two-photon lithography.

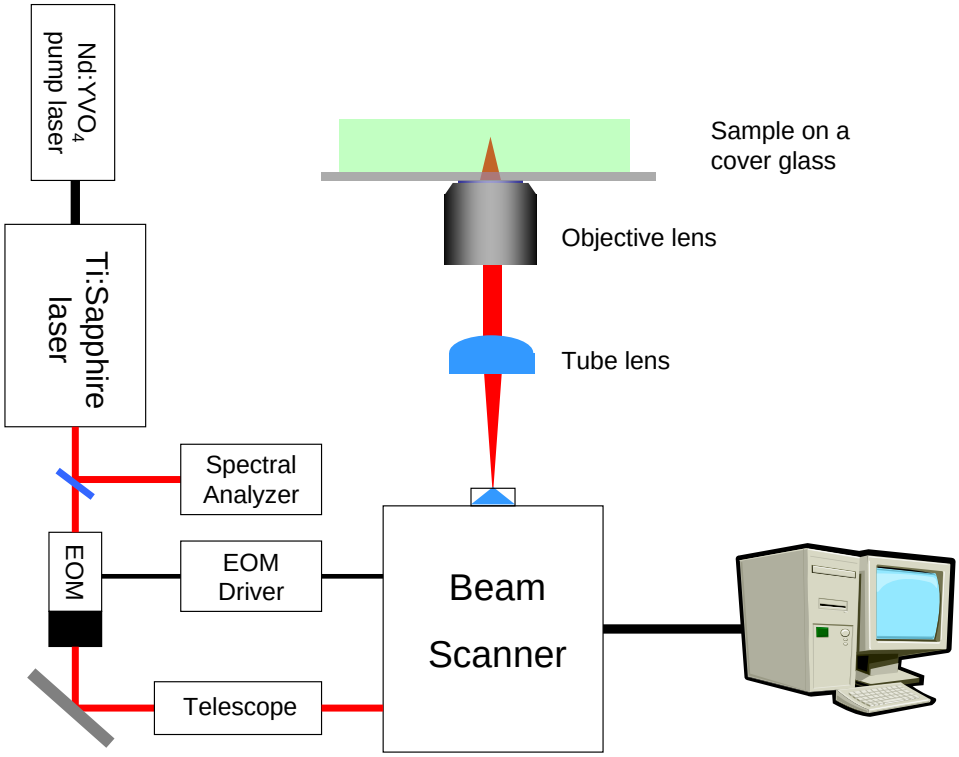

Figure A.3: An illustration of the setup of multiphoton microscope system used in the study.

A.2.1 Experimental

The multiphoton microscope system used in this work is a Bio-Rad MRC-1024, equipped with a Nd:YVO_4 pump laser, a Ti-sapphire laser, an electro-optic modulator (EOM), motor driven mirrors and stage, and some other optical elements (Fig. A.3). It is attached to an Olympus IX70 inverted microscope, with a 10× long working distance objective, 20× and 40× water-immersion objectives, and 63× and 100× high NA oil-immersion objectives. The Ti:sapphire laser operates at 80 MHz and produces pulses with durations of 200 femtoseconds after mode-locking. The operating wavelength was set at 780 nm.

A C-dot template was first infiltrated with a photosensitive resin of 95 wt.% polymerizable monomer PETA (penta-erythritol-triacrylate) and 5 wt.% photoinitiator ITX (isopropyl-9H-thioxanthen-9-one). Since the substrate of the template was a non-transparent silicon wafer piece, a thin cover glass was placed on top of the sample and then the stack was flipped and mounted on the microscope stage upside down. Usually a 40× 1.15 NA water lens was used and brought in contact with the cover glass. Since the multiphoton microscope used is also a confocal microscope, the fluorescent C-dots template was mapped out in the confocal mode before two-photon exposure, providing the information of the location of the laser beam focus relative to the template. Subsequently, the beam focus was located inside the template to polymerize the resin in the middle of the template. The location and exposure dose of each polymerized voxel were controlled by software on the computer connected to the microscope. The exposure dose for the defects reported here was 0.6 mJ/voxel and separations between neighboring voxels are approximately 100 nm. After exposure, the resin was developed in ethyl acetate for approximately 1 to 3 minutes. Only the exposed and polymerized volumes remained inside the template after development.

In order to charaterize the engineered defects inside the C-dots template using confocal microscope, a dye different from the TRITC dye (tetramethylrhodamine-5-(and 6)-isothiocyanate) encapsulated in the C-dots was needed to add to the resin formulation so that the emission peaks from the fluorescent template and defects could be distinguished by the microscope. Dye DEAC (7-diethylaminocoumarin-3-carboxylic) was chosen for the purpose because it has an absorption peak around 432 nm and an emission peak around 472 nm while the dyes in the C-dots template have an absorption peak around

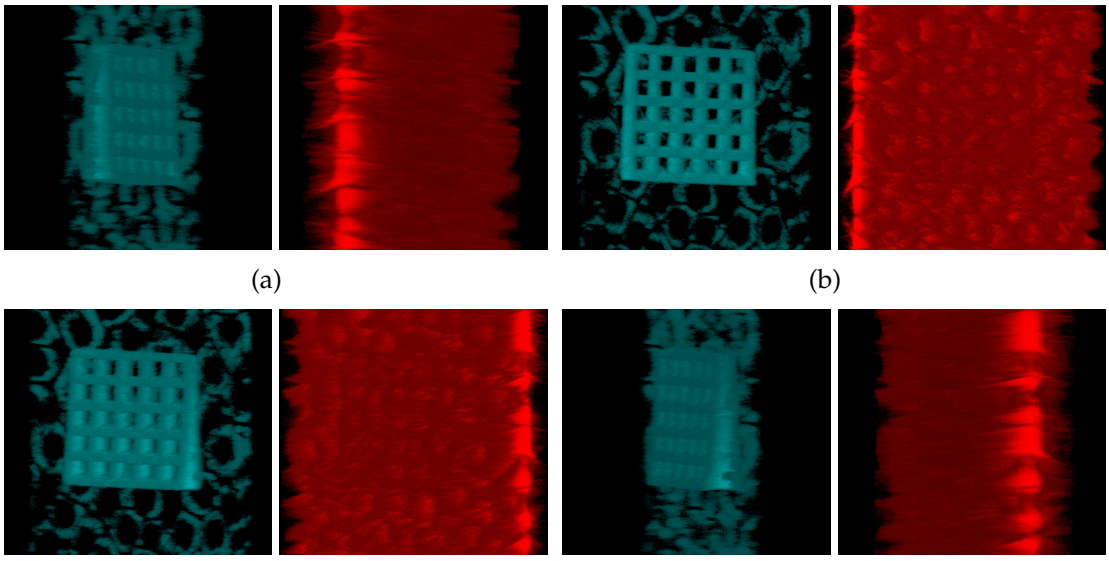

Figure A.4: Three-dimensional fluorescence images reconstructed from signals collected from PMT 1 (blue) and PMT 2 (red). (a)-(d) display four sets of signals at four different angles.

541 nm and an emission peak around 572 nm. The laser wavelengths of the confocal microscope are 458 nm and 543 nm, perfect to excite DEAC and TRITC dyes. Photomultiplier (PMT) detectors were set to collect signals at approximately 520 nm and 580 nm for detection of emitted light from the DEAC and TRITC dyes respectively.

A.2.2 Results and Discussions

Figure A.4 shows some three-dimensional fluorescence images reconstructed from signals collected from the two PMT channels of the confocal microscope. The images are diplays of the waffle-like defect and the template at a series of observing angles. If the signals (blue and red in Fig. A.4) are combined at the four different angles, the defect can be clearly observed embedded in the

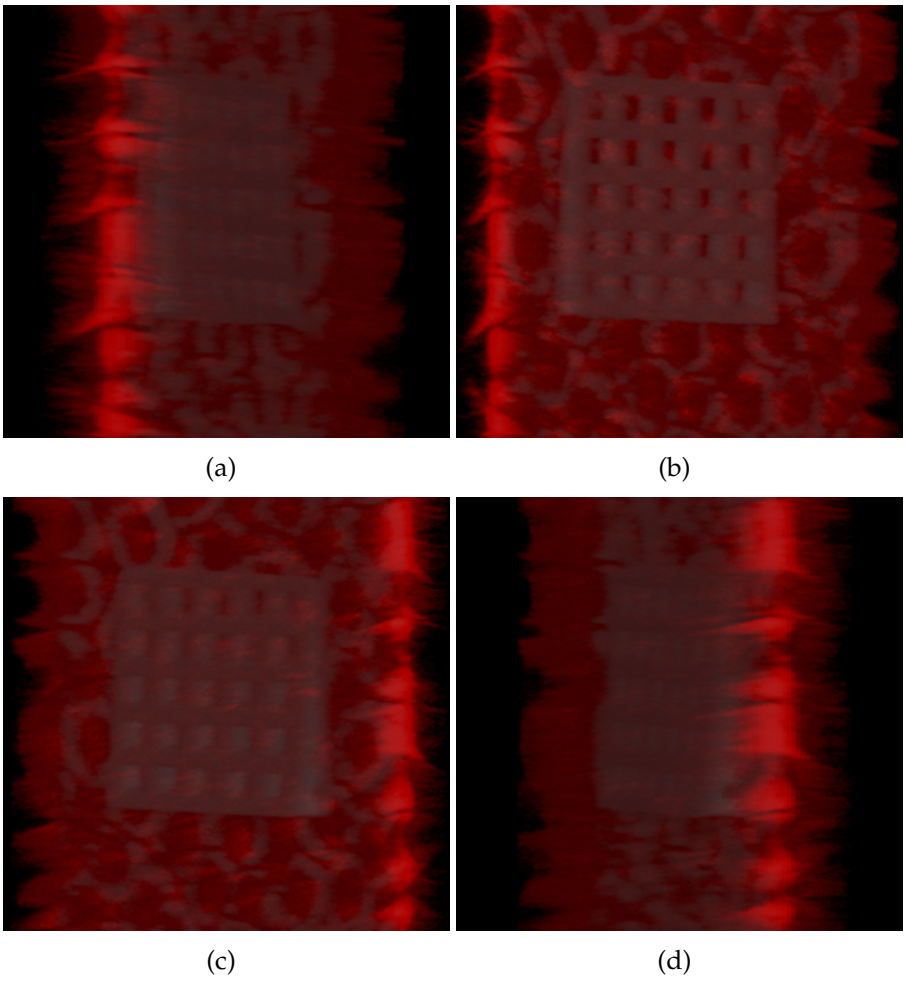

Figure A.5: Three-dimensional reconstruction of confocal microscopy images of a fluorescent waffle-like polymer structure inside an inverse-opal C-dot template (combined signals of PMT 1 & 2 from Figure A.4).

template as shown in Fig. A.5. The dimensions of the polymer "waffle" are about 50 μm by 50 μm by 2 μm.

A.2.3 Summary and Future Directions

So far, we have demonstrated that it is facile to pattern polymer structures of arbitrary designs inside a porous photonic crystal by two-photon lithography.

The next step would be to design some functional defect structures, fabricate them and take some optical measurement. We have proven that two-photon lithography is a powerful tool to fabricate three-dimensional structures for potential optical applications, and this research may be continued in the future.

A.3 Two-Photon Patterning of Molecular Glass Resists

This section discusses our attempts at crosslinking molecular glass resists in three dimensions using two-photon lithography.

Molecular glass resists are a patterning material alternative to conventional polymeric photoresists. More details of this material will be covered in chapter 4. Here we will explore the possibility of two-photon patterning molecular glass resists via cationic crosslinking in the hope of achieving three-dimensional patterns.

The molecular glass resist used in this study is 4-[4-[1,1-bis(4-hydroxyphenyl) ethyl]]-α,α-dimethylbenzylphenol (**MG2-OH**) purchased from TCI America. Crosslinker Powderlink^{TM} 1174 (tetrakis(methoxylmethyl)glycoluril) (**TMMGU**) was obtained from Day Chem Laboratories. Ionic photoacid generator triarylsulfonium hexafluoroantimonate salts (**THS**) was purchased from Aldrich and used without further purification. Non-ionic two-photon acid generator N,N'-di-(2-nitro-4-(trifluoromethyl) benzenesulfonyloxy)-4,4'-(phenylene-1,3-dioxy) dinaphthalene-1,8;1',8'-tetra carboxylic imide (**NPOD**) was synthesized in house.[165] Two-photon sensitizer **AF-69** was received from Air Force Research Laboratory (Dayton, Ohio). The chemical structures of the materials are shown in Fig. A.6.

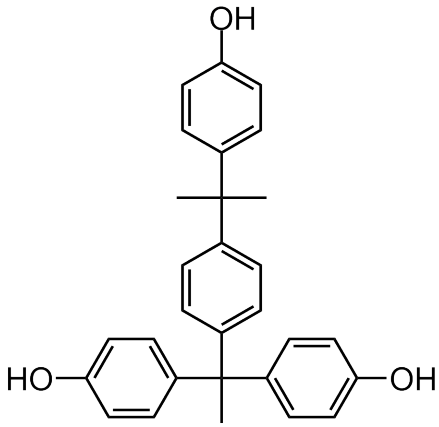

MG2-OH

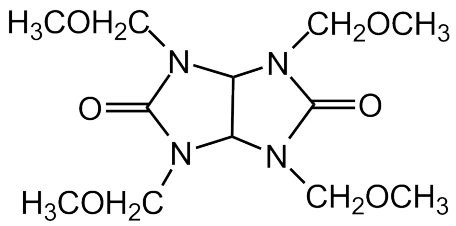

TMMGU

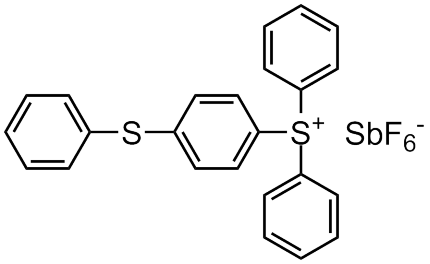

THS

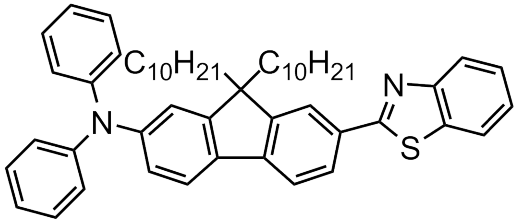

AF-69

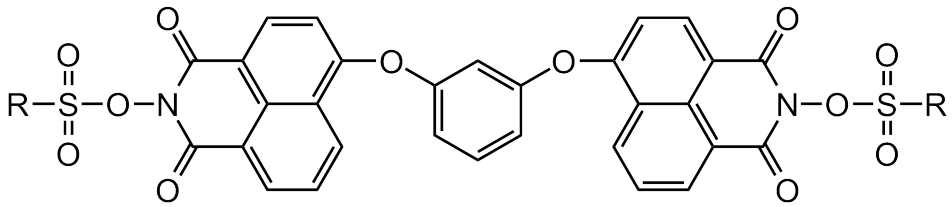

NPOD

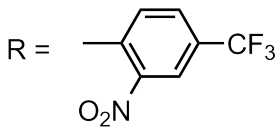

Figure A.6: Chemical structures of molecular glass MG2-OH, crosslinker TMMGU, photoacid generator THS, non-ionic two-photon acid generator NPOD, and two-photon sensitizer AF-69.

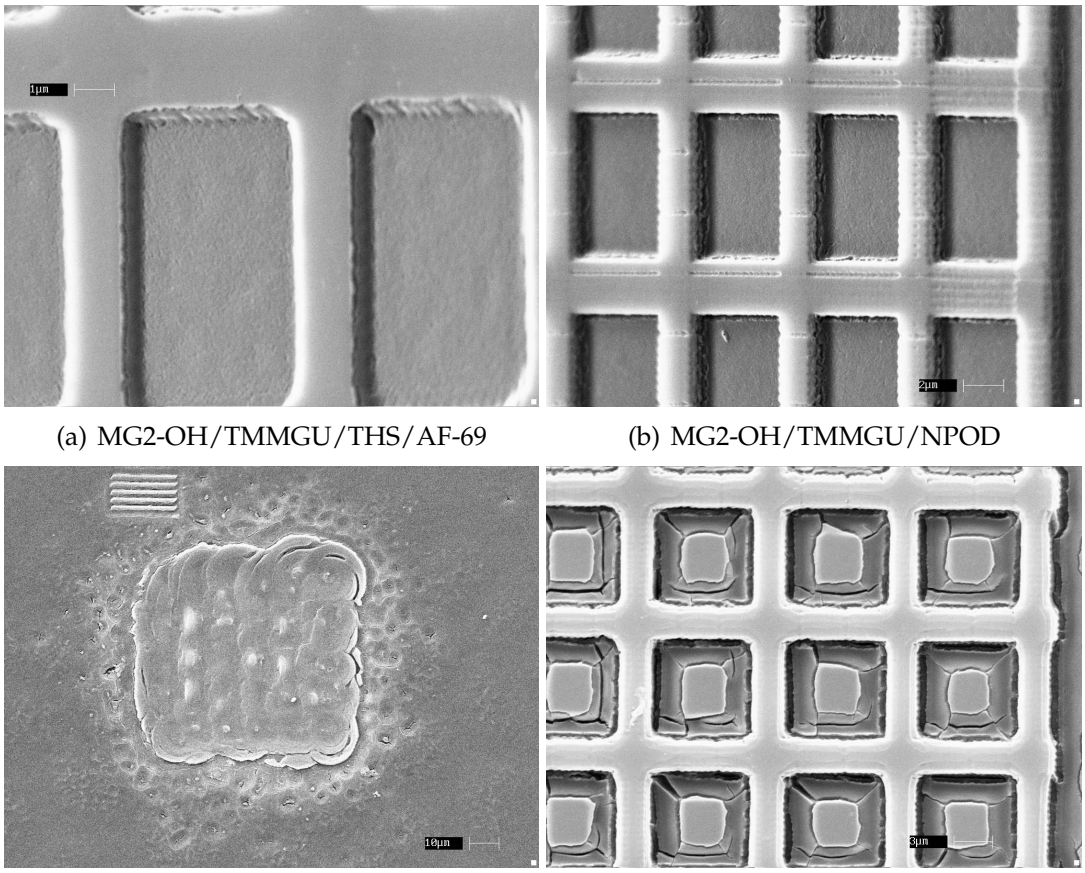

(a) MG2-OH/TMMGU/THS/AF-69 (b) MG2-OH/TMMGU/NPOD

(c) MG2-OH/TMMGU/NPOD (d) Polyphenol/TMMGU/NPOD

Figure A.7: SEM images of molecular glass resists patterned by two photon lithography.

The cationic crosslinking between MG2-OH and TMMGU is triggered by protons generated by photoacid generators (PAGs) upon irradiation. Since THS has a small two-photon absorption cross section σ (i.e. low two-photon absorption), two-photon sensitizer AF-69 with a much larger σ is a must to facilitate the activation of THS through non-radiative transfer of photon energies. NPOD is a PAG with a large σ and therefore additional photosensitizers are not necessary for the resist formulation.[165] Addition of either THS/AF-69 or NPOD to MG2-OH/TMMGU makes a photocrosslinkable molecular glass resist system. Figure A.7(a) and (b) display two SEM images of pseudo-3D

photoresist patterns of MG2-OH/TMMGU/THS/AF-69 (P=10mW) and MG2-OH/TMMGU/NPOD (P=3mW) respectively. When photoresist film thickness was increased up to 1 micron for real 3D patterning, resist structures did not seem fully developed even when MG2-OH was substituted with a chemically similar molecular glass polyphenol having slightly more crosslinking sites per molecule than MG2-OH, as shown in Fig. A.7 (c) and (d). A possible reason could be that the crosslinking density of the molecular glass resist system was low (only 3 functional groups on each MG2-OH molecule and 4 on each TMMGU molecule) and thus a dense photoresist network could not form to achieve a large solubility contrast between exposed and unexposed regions when immersed in developers.

A.4 Conclusions and Future Work

This chapter covers two-photon polymerization inside an inverse-opal C-dot template for optical applications and efforts to crosslink molecular glass resists in three dimensions by two-photon lithography. It is safe to say that two-photon lithography demonstrates an unprecedented potential in terms of introducing designed polymeric defects in photonic templates. The biggest challenge facing the patterning technique is the alignment of defects with respect to the templates for good registration accuracy. A pre-fabrication mapping of templates is foreseen to come into play. With regard to two-photon patterning molecular glass resists, branched molecules with higher crosslinking densities are expected to improve the patterning contrast.

BIBLIOGRAPHY

[1] "Intel: 'EUV Facts Don't Add Up' for 22 nm in 2011", *Semiconductor International*, 4/22/2008.

[2] "SPIE: Intel to extend immersion to 11-nm", *EE Times*, 02/22/2010.

[3] "Marching to the Beat of Moore's Law", Presentation by Y. Borodovsky, SPIE Microlithography, 2006.

[4] P. Nehmiz, W. Zapka, U. Behringer, M. Kallmeyer, and H. Bohlen, *J. Vacuum Sci. Technol. B*, **3**, 136 (1985).

[5] A. Gonzales, *Electron-Beam, X-ray, and Ion-Beam Submicrometer Lithographies VIII*, 374 (1989).

[6] H. Ito, C. G. Willson, J. M. J. Fréchet, *Digest of Technical Papers of 1982 Symposium on VLSI Technology*, p 86 (1982).

[7] H. Ito and C. G. Willson, *Technical Papers of SPE Regional Technical Conference on Photopolymers*, p 331 (1982).

[8] H. Ito and C. G. Willson, *Polym. Eng. Sci.*, **23**, 1012 (1983).

[9] W. Hinsberg, S. MacDonald, N. Clecak, C. Snyder, and H. Ito, *Proceedings of SPIE*, **1925**, 43 (1993).

[10] H. Ito, G. Breyta, D. Hofer, R. Sooriyakumaran, K. Petrillo, and D. Seeger, *J. Photopolym. Sci. Technol.*, **7**, 433 (1994).

[11] T. Kumada, Y. Tanaka, A. Ueyama, S. Kubota, H. Koezuka, T. Hanawa, and H. Morimoto, *Proceedings of SPIE*, **1925**, 31 (1991).

[12] M. Yoshizawa and S. Moriya, *J. Vacuum Sci. Technol. B*, **20**, 1342 (2002).

[13] G. W. Reynolds and J. W. Taylor, *J. Vacuum Sci. Technol. B*, **17**, 334 (1999).

[14] M. Farhoud, J. Ferrera, A. J. Lochtefeld, T. E. Murphy, M. L. Schattenburg, J. Carter, C. A. Ross, and H. I. Smith, *J. Vacuum Sci. Technol. B*, **17**, 3182 (1999).

[15] J. P. Spallas, R. D. Boyd, J. A. Britten, A. Fernandez, A. M. Hawryluk, M. D. Perry, and D. R. Kania, *J. Vacuum Sci. Technol. B*, **14**, 2005 (1996).

[16] M. Campbell, D. N. Sharp, M. T. Harrison, R. G. Denning, and A. J. Turberfield, *Nature*, **404**, 53 (2000).

[17] United States Patent 6977127.

[18] United States Patent 5928813.

[19] S. Jeon, J.-U. Park, R. Cirelli, S. Yang, C. E. Heitzman, P. V. Braun, P. J. A. Kenis, and J. A. Rogers, *Proc. Natl. Acad. Sci. USA*, **101**, 12428 (2004).

[20] I. Bita, T. Choi, M. E. Walsh, H. I. Smith, and E. L. Thomas, *Adv. Mater.*, **19**, 1403 (2007).

[21] B. Kaehr and J. B. Shear, *J. Am. Chem. Soc.*, **129**, 1904 (2007).

[22] S. Kawata, H.-B. Sun, T. Tanaka, and K. Takada, *Nature*, **412**, 697 (2001).

[23] J.-B. Park, S.-H. Kim, S.-J. Kim, J.-H. Cho, and H.-K. Oh, *Jpn. J. Appl. Phys.*, **46**, 28 (2007).

[24] United State Patent 6,335,152 B1.

[25] J. Sha, B. Jung, M. O. Thompson, C. K. Ober, M. Chandhok, and T. R. Younkin, *J. Vac. Sci. Technol. B*, **27**, 3020 (2009).

[26] J.-K. Lee, M. Chatzichristidi, A. A. Zakhidov, P. G. Taylor, J. A. DeFranco, H. S. Hwang, H. H. Fong, A. B. Holmes, G. G. Malliaras, and C. K. Ober, *J. Am. Chem. Soc.*, **130**, 11564 (2008).

[27] P. G. Taylor, J.-K. Lee, A. A. Zakhidov, M. Chatzichristidi, H. H. Fong, J. A. DeFranco, G. G. Malliaras, and C. K. Ober, *Adv. Mater.*, **21**, 2314 (2009).

[28] W.-T. Tsai, *J. Hazard. Mater.*, **119**, 69 (2005).

[29] V. Auzelyte, A. Langner, and H. H. Solak, *J. Vac. Sci. Technol. B*, **27**, 2990 (2009).

[30] K. E. Uhrich, E. Reichmanis, and F. A. Baiocchi, *Chem. Mater.*, **6**, 295 (1994).

[31] N. Sundararajan, C. F. Keimel, N. Bhargava, C. K. Ober, J. Opitz, R. D. Allen, G. Barclay, and G. Xu, *J. Photopolym. Sci. Technol.*, **12**, 457 (1999).

[32] H. Krautter, F. Houlihan, R. Hutton, I. Rushkin, and R. Opila, *Proceedings of the SPIE Advances in Resist Technology and Processing XVII*, **3999**, 1070 (2000).

[33] V. M. Prabhu, S. Sambasivan, D. Fischer, L. K. Sundberg, and R. D. Allen, *Appl. Surf. Sci.*, **253**, 1010 (2006).

[34] A. Sundaramoorthia, T. R.Younkinb, and C. L. Henderson, *Proceedings of SPIE*, **7273**, 72733V (2009).

[35] E. Lin, C. Soles, D. Goldfarb, B. Trinque, S. Burns, R. Jones, J. Lenhart, M. Angelopoulos, C. Willson, and S. Satija, *Science*, **297**, 372 (2002).

[36] K. A. Lavery, V. M. Prabhu, E. K. Lin, W.-L. Wu, S. K. Satija, K.-W. Choi, and M. Wormington, *Appl. Phys. Lett.*, **92**, 064106 (2008).

[37] C. Nelson, S. C. Palmateer, A. R. Forte, and T. M. Lyszczarz, *J. Vac. Sci. Technol. B*, 17, 2488 (1999).

[38] J. Foucher, A. Pikon, C. Andes, and J. Thackeray, *Proceedings of SPIE*, **6518**, 65181Q (2007).

[39] S. Kang, K. Lavery, K.-W. Choi, V. M. Prabhu, W. Wu, E. K. Lin, A. De Silva, N. Felix, and C. K. Ober, *Proc. of SPIE*, **6923**, 692317-1 (2008).

[40] E. Richter, S. Hien, and M. Sebald, *Journal of Photopolymer Science and Technology*, **12**, 695 (1999).

[41] C.-T. Lee, W. Yueh, J. M. Roberts, T. R. Younkin, C. L. Henderson, *Proc. SPIE*, **6923**, 692316-1 (2008).

[42] H. Ito, *Adv. Polym. Sci.*, **172**, 37 (2005).

[43] F. A. Houle, W. D. Hinsberg, M. I. Sanchez, and J. A. Hoffnagle, *J. Vac. Sci. Technol. B*, **20**, 924 (2002).

[44] W. D. Hinsberg, F. A. Houle, M. I. Sanchez, and G. M. Wallraff, *IBM J. Res. & Dev.*, **45**, 667 (2001).

[45] Y. F. Chong, K. L. Pey, A. T. S. Wee, A. See, L. Chan, Y. F. Lu, and W. D. Song, *Appl. Phys. Lett.*, **76**, 3198 (2000).

[46] S. Talwar, D. Markle and M. Thompson, *Proceedings of the Solid State Technology*, p. 83 (2003).

[47] B. N. Hansen, B. M. Hybertson, R. M. Barkley, and R. E. Sievers, *Chem. Mater.*, **4**, 749 (1992).

[48] J. M. Blackburn, D. P. Long, A. Cabanas, and J. J. Watkins, *Science*, **294**, 141 (2001).

[49] C. A. Bessel, G. M. Denison, J. M. DeSimone, J. DeYoung, S. Gross, C. K. Schauer, and P. M. Visintin, *J. Am. Chem. Soc.*, **125**, 4980 (2003).

[50] C. A. Jones, D. X. Yang, E. A. Irene, S. M. Gross, M. Wagner, J. DeYoung, and J. M. DeSimone, *Chem. Mater.*, **15**, 2867 (2003).

[51] R. A. Pai, R. Humayun, M. T. Schulberg, A. Sengupta, J. N. Sun, and J. J. Watkins, *Science*, **303**, 507 (2004).

[52] V. R. Tirumala, R. A. Pai, S. Agarwal, J. J. Testa, G. Bhatnagar, A. H. Romang, C. Chandler, B. P. Gorman, R. L. Jones, E. K. Lin, and J. J. Watkins, *Chem. Mater.*, **19**, 5868 (2007).

[53] E. N. Hoggan, K. Wang, D. Flowers, J. M. DeSimone, and R. G. Carbonell, *IEEE Trans. Semicond. Manuf.*, **17**, 510 (2004).

[54] N. Felix and C. K. Ober, *Chem. Mater.*, **20**, 2932 (2008).

[55] M. Wagner, J. DeYoung, C. Harbinson, and M. Miles, *Proc. of SPIE*, p U1551 (2006).

[56] I. Jafri, H. Busta, and S. T. Walsh, *Proc. of SPIE*, **3880**, 51 (1999).

[57] P. Miller, D. Price, M. Burtch, C. Bowers, *GaAs MANTECH International Conference on Compound Semiconductor*, Las Vegas, CA, 2001.

[58] H. S. Hwang, A. A. Zakhidov, J.-K. Lee, X. Andre, J. A. DeFranco, H. H. Fong, A. B. Holmes, G. G. Malliaras, and C. K. Ober, *J. Mater. Chem.*, **18**, 3087 (2008).

[59] M. Tanaka, A. Rastogi, G. N. Toepperwein, R. A. Riggleman, N. M. Felix, J. J. de Pablo, and C. K. Ober, *Chem. Mater.*, **21**, 3125 (2009).

[60] S. Kilic, S. Michalik, Y. Wang, J. K. Johnson, R. M. Enick, and E. J. Beckmans, *Macromolecules*, **40**, 1332 (2007).

[61] Y. Wang, L. Hong, D. Tapriyal, I. C. Kin, I.-H. Paik, J. M. Crosthwaite, A. D. Hamilton, M. C. Thies, E. J. Beckman, R. M. Enick, and J. K. Johnson, *J. Phys. Chem. B*, **113**, 14971 (2009).

[62] J. M. Prausnitz, R. N. Lichtenthaler, and E. G. Azevedo, *Molecular Thermodynamics of Fluid Phase Equilibria*, 2nd ed.; Prentice Hall: Englewood Cliffs, NJ, (1986).

[63] L. L. Lee, *Molecular Thermodynamics of Nonideal Fluids*; Butterworth Publishers: Stoneham, MA, 1988.

[64] S. H. Huang and M. Radosz, *Industrial & Engineering Chemistry Research*, **29**, 2284 (1990).

[65] M. Lora and M. A. McHugh, *Fluid Phase Equilibria*, **157**, 285 (1999).

[66] M. Banaszack, C. K. Chen, and M. Radosz, Macromocules, 29, 6481 (1996).

[67] G. Luna-Barcenas, S. Mawson, S. Takishima, J. M. DeSimone, I. C. Sanchez, and K. P. Johnston, *Fluid Phase Equilibria*, **146**, 325 (1998).

[68] T. J. de Vries, P. J. A. Somers, T. W. de Loos, M. A. G. Vorstman, and J. T. F. Keurentjes, *Industrial & Engineering Chemistry Research*, **39**, 4510 (2000).

[69] E. A. Muller and K. E. Gubbins, *Industrial & Engineering Chemistry Research*, **40**, 2193 (2001).

[70] K. P. Johnston, D.G. Peck, and S. Kim, *Industrial & Engineering Chemistry Research*, **28**, 1115 (1989).

[71] B.-C. Lee and R. P. Danner, *AIChE Journal*, **42**, 837, (1996).

[72] R. P. Danner, M. Hamedi, and B.-C. Lee, *Fluid Phase Equilibria*, **194**, 619 (2002).

[73] S. G. Kazarian, M. F. Vincent, F. V. Bright, C. L. Liotta, and C. A. Eckert, *J. Am. Chem. Soc.*, **118**, 1729 (1996).

[74] A. Dardin, J. M. DeSimone, and E. T. Samulski, *Journal of Physical Chemistry B*, **102**, 1775 (1998).

[75] N. Sundararajan, S. Yang, K. Ogino, S. Valiyaveettil, J. Wang, X. Zhou, C. K. Ober, S. K. Obendorf, and R. D. Allen, *Chem. Mater.*, **12**, 41 (2000).

[76] A. I. Cooper, *J. Mater. Chem.*, **10**, 207 (2000).

[77] V. Q. Pham, R. J. Ferris, A. Hamad, and C. K. Ober, *Chem. Mater.*, **15**, 4893 (2003).

[78] V. Q. Pham, P. T. Nguyen, G. L. Weibel, R. J. Ferris, and C. K. Ober CK, *Polym Prepr*, **43**, 885 (2002).

[79] M. K. Boggiano, D. Vellenga, R. Carbonell, V. S. Ashby, and J. M. DeSimone, *Polymer*, **47**, 4012 (2006).

[80] P. M. Gallagher-Wetmore, G. M. Wallraff, and R. D. Allen, *Proc SPIE Int Soc Opt Eng*, **2438**, 694 (1995).

[81] C. K. Ober, A. H. Gabor, P. M. Gallagher-Wetmore, and R. D. Allen, *Adv. Mater.*, **9**, 1039 (1997).

[82] A. H. Gabor, and C. K. Ober, *Microelectron Technol*, **614**, 281 (1995).

[83] A. H. Gabor, L. C. Pruette, and C. K. Ober, *Chem. Mater.*, **8**, 2282 (1996).

[84] H. S. Hwang, A. A. Zakhidov, J.-K. Lee, X. Andre, J. A. DeFranco, H. H. Fong, A. B. Holmes, G. G. Malliaras, and C. K. Ober, *J. Mater. Chem.*, **18**, 3087 (2008).

[85] M. Yoshiwa, H. Kageyama, Y. Shirota, F. Wakaya, K. Gamo, and M. Takai, *Appl. Phys. Lett.*, **69**, 2605 (1996).

[86] S. W. Chang, R. Ayothi, D. Bratton, D. Yang, N. Felix, H. B. Cao, H. Deng, and C. K. Ober, *J. Mater. Chem.*, **16**, 1470 (2006).

[87] C. F. Kirby and M. A. McHugh, *Chem. Rev.*, **99**, 565 (1999).

[88] J. M. DeSimone, Z. Guan, and C. S. Elsbernd, *Science*, **257**, 945 (1992).

[89] N. M. Felix, K. Tsuchiya, and C. K. Ober, *Adv. Mater.*, **18**, 442 (2006).

[90] K. Young-Gil, J. B. Kim, T. Fujigaya, Y. Shibasaki and M. Ueda, *J. Mater. Chem.*, **12**, 53 (2002).

[91] Y. Shirota, *J. Mater. Chem.*, **10**, 1 (2002).

[92] K. Takeshi, R. Nakayama, and M. Ueda, *Chem. Lett.*, **27**, 865 (1998).

[93] A. De Silva, J.-K. Lee, X. Andre, N. M. Felix, H. B. Cao, H. Deng, and C. K. Ober, *Chem. Mater.*, **20**, 1606 (2008).

[94] Y. Kwon, H. Yun, R. Ganesan, J.-B. Kim, and J.-H. Choi, *Polymer Journal*, **38**, 996 (2006).

[95] J. B. Kim, T. H. Oh, and Y.-G. Kwon, *Proc. of SPIE*, **4690**, 549 (2002).

[96] C. Vannuffel, D. Djian, S. Tedesco, D. Niakoula, P. Argitis, V. P. Vidali, E. A. Couladouros, and H. Solak, *Proc. of SPIE*, **6519**, 651949 (2007).

[97] R. Sooriyakumaran, T. Hoa, L. Sundberg, M. Morris, B. Hinsberg, H. Ito, R. Allen, W.-S. Huang, D. Goldfarb, S. Burns, and D. Pfeiffer, *J. Photopolym. Sci. Technol.*, **18**, 425 (2005).

[98] A. Villiers, *C. R. Hebd. Seances Acad. Sci.*, **112**, 536 (1891).

[99] W. Saenger, *Angew. Chem. Int. Ed. Egnl.*, **19**, 344 (1980).

[100] W. Saegner, *Angew. Chem.*, **92**, 343 (1980).

[101] R. P. Bonarlaw, A. P. Davis, and J. K. M. Sanders, *J. Chem. Soc.-Perkin Trans.*, **1** (8), 2245-2250 (1990).

[102] P. C. Tsiartas, L. W. Flanagin, C. L. Henderson, W. D. Hinsberg, I. C. Sanchez, R. T. Bonnecaze, and C. G. Willson, *Macromolecules*, **30**, 4656 (1997).

[103] J.-B. Kim, Y.-G. Kwon, H.-J. Yun, and J.-H. Choi, *Proc. of SPIE*, **4690**, 837 (2002).

[104] G. Wallraff and W. Hinsberg, *Chemical Reviews*, **99**, 1801 (1999).

[105] D. Goldfarb, M. Angelopoulos, E. Lin, R. Jones, C. Soles, J. Lenhart, and W. Wu, *J. Vac. Sci. Technol. B*, **19**, 2699 (2001).

[106] M. Stewart, H. Tran, G. Schmid, T. Stachowiak, D. Becker, and C. Willson, *J. Vac. Sci. Technol. B*, **20**, 2946 (2002).

[107] G. Schmid, M. Stewart, V. Singh, and C. Willson, *J. Vac. Sci. Technol. B*, **20**, 185 (2002).

[108] J. Hoffnagle, W. Hinsberg, M. Sanchez, and F. Houle, *Optics Letters*, **27**, 1776 (2002).

[109] J. Kim, Y. Kim, S. Chon, T. Nagai, M. Noda, Y. Yamaguchi, Y. Makita, and H. Nemoto, *J. Photopolym. Sci. Technol.*, **17**, 379 (2004).

[110] International Technology Roadmap for Semiconductors 2007 Edition, http://www.itrs.net, Lithography Section, p10 (2007).

[111] S. Kang, V. Prabhu, W. Wu, E. Lin, K. Choi, M. Chandhok, T. Younkin, and W. Yueh, *Proceedings of SPIE*, **7273**, 72733U (2009).

[112] S. Postnikov, M. Stewart, H. Tran, M. Nierode, D. Medeiros, T. Cao, J. Byers, S. Webber, and C. Wilson, *J. Vac. Sci. Technol. B*, **17**, 3335 (1999).

[113] M. Stewart, M. Somervell, H. Tran, S. Postnikov, and C. Willson, *Proceedings of SPIE*, **3999**, 665 (2000).

[114] T. Schnattinger and A. Erdmann, *Proceedings of SPIE*, **6923**, 69230R (2008).

[115] M. Zuniga and A. Neureuther, *J. Vac. Sci. Technol. B*, **13**, 2957 (1995).

[116] W. Hinsberg, F. Houle, M. Sanchez, M. Morrison, G. Wallraff, C. Larson, J. Hoffnagle, P. Brock, and G. Breyta, *Proceedings of the SPIE*, **3999**, 148 (2000).

[117] F. Houle, W. Hinsberg, M. Morrison, M. Sanchez, G. Wallraff, C. Larson, and J. Hoffnagle, *J. Vac. Sci. Technol. B*, **18**, 1874 (2000).

[118] K. Lavery, B. Vogt, V. Prabhu, E. Lin, W. Wu, S. Satija, and K. Choi, *J. Vac. Sci. Technol. B*, **24**, 3044 (2006).

[119] B. Vogt, S. Kang, V. Prabhu, E. Lin, S. Satija, K. Turnquest, and W. Wu, *Macromolecules*, **39**, 8311 (2006).

[120] B. Vogt, S. Kang, V. Prabhu, A. Rao, E. Lin, W. Wu, S. Satija, and K. Turnquest, *J. Vac. Sci. Technol. B*, **25**, 175 (2007).

[121] D. VanderHart, V. Prabhu, A. Silva, N. Felix, and C. Ober, *J. Mater. Chem.*, **19**, 2683 (2009).

[122] S. Kang, W. Wu, K. Choi, A. De Silva, C. Ober, and V. Prabhu, *Macromolecules*, accepted (2010).

[123] J. Dai, S. Chang, A. Hamad, N. Felix, and C. Ober, *Chem. Mater.*, **18**, 3404 (2006).

[124] M. Ueda, D. Takahashi, T. Nakayama, and O. Haba, *Chem. Mater.*, **10**, 2230 (1998).

[125] D. J. Cram, S. Karbach, H.-Y. Kim, C. B. Knobler, E. F. Maverick, J. L. Ericson, and R. C. Helgeson, *J. Am. Chem. Soc.*, **110**, 2229 (1988).

[126] H. Ito, T. Nakayama, M. Sherwood, D. Miller, and M. Ueda, *Chem. Mater.*, **20**, 341 (2007).

[127] J. Crank and G. Park, Diffusion in Polymers, Academic Press, 1968.

[128] R. Bristol, Proceedings of SPIE, 6519, 65190W (2007).

[129] A. De Silva, N. Felix, C. Ober, *Adv. Mater.*, **20**, 3355 (2008).

[130] J. T. Woodward, K. W. Choi, V. M. Prabhu, S. Kang, K. A. Lavery, W. L. Wu, M. Leeson, A. De Silva, N. M. Felix, C. K. Ober, *Proceeding of SPIE*, **6923**, 69232B-12 (2008).

[131] M. Göppert-Mayer, Uber elementarakte mit zwei quantensprüngen, *Ann. Phys.*, **9**, 273 (1931).

[132] W. Kaiser and C. G. B. Garret, *Phys. Rev. Lett.*, **7**, 229 (1961).

[133] W. R. Zipfel, R. M. Willaims, and W. W. Webb, *Nature Biotechnology*, **21**, 1369 (2003).

[134] Y.-H. Pao and P. M. Rentzepis, *Appl. Phys. Lett.*, **80**, 312 (2002).

[135] E. Yablonovitch, *J. Mod. Opt.*, **41**, 173 (1994).

[136] D. Therriault, S. R. White, and J. A. Lewis, *Nat. Mater.*, **2**, 265 (2003).

[137] S. Jeon, V. Malyarchuk, J. O. White, and J. A. Rogers, *Nano Lett.*, **5**, 1351 (2005).

[138] A. delCampo and E. Arzt, *Chem. Rev.*, **108**, 911 (2008).

[139] E. Fabrizio, F. Perennes, F. Romanato, S. Cabrini, D. Cojoc, M. Tormen, L. Businaro, L. Vaccari, R. Proietti, and R. Kumar, *BioMEMS Nanotechnol.*, p. 97 (2006).

[140] X. Hu, G. Li, M. Li, J. Huang, Y. Li, Y. Gao, and Y. Zhang, *Adv. Funct. Mater.*, **18**, 575 (2008).

[141] J. H. Holtz and S. A. Asher, *Nature*, **389**, 829 (1997).

[142] J. W. Long, B. Dunn, D. R. Rolison, and H. S. White, *Chem. Rev.*, **104**, 4463 (2004).

[143] L. Dhar, K. Curtis, and T. Facke, *Nat. Photonics*, **2**, 403 (2008).

[144] D. A. Parthenopoulos and P. M. Rentzepis, *Science*, **245**, 843 (1989).

[145] M. L. K. Hoa, M. Lu, and Y. Zhang, *Adv. Colloid Interface Sci.*, **121**, 9 (2006).

[146] P. Yao, G. Schneider, D. Prather, E. Wetzel, and D. O'Brien, *Opt. Express*, **13**, 2370 (2005).

[147] S. Noda, N. Yamamoto, H. Kobayashi, M. Okano, and K. Tomoda, *Appl. Phys. Lett.*, **75**, 905 (1999).

[148] J. Zaumseil, M. A. Meitl, J. W. P. Hsu, B. R. Acharya, K. W. Baldwin, Y. L. Loo, and J. A. Rogers, *Nano Lett.*, **3**, 1223 (2003).

[149] P. Dario, M. C. Carrozza, N. Croce, M. C. Montesi, and M. Cocco, *J. Micromech. Microeng.*, **5**, 64 (1995).

[150] R. Mayoral, J. Requena, J. S. Moya, C. Lopez, A. Cintas, H. Miguez, F. Meseguer, L. Vazquez, M. Holgado, and A. Blanco, *Adv. Mater.*, **9**, 257 (1997).

[151] J. E. Smay, G. M. Gratson, R. F. Shepherd, J. Cesarano, and J. A. Lewis, *Adv. Mater.*, **14**, 1279 (2002).

[152] E. B. Duoss, M. Twardowski, and J. A. Lewis, *Adv. Mater.*, **19**, 3485(2007).

[153] J. H. Moon, J. Ford, and S. Yang, *Polym. Adv. Technol.*, **17**, 83 (2006).

[154] A. J. Turberfield, *MRS Bull.*, **26**, 632 (2001).

[155] S. Jeon, J.-U. Park, R. Cirelli, S. Yang, C. E. Heitzman, P. V. Braun, P. J. A. Kenis, and J. A. Rogers, *Proc. Natl. Acad. Sci. USA*, **101**, 12428 (2004).

[156] G.Witzgall, R. Vrijen, E. Yablonovitch, V. Doan, and B. J. Schwartz, *Opt. Lett.*, **23**, 1745 (1998).

[157] B. Richards and E. Wolf, *Proc. R. Soc. Lond. A*, **253**, 358 (1959).

[158] D. Tan, Y. Li, F. Qi, H. Yang, Q. Gong, X. Dong, and X. Duan, *Appl. Phys. Lett.*, **90**, 071106 (2007).

[159] K. Takada, H.-B. Sun, and S. Kawata, *Appl. Phys. Lett.*, **86**, 071122 (2005).

[160] K. Takada, H.-B. Sun, and S. Kawata, *Proc. SPIE*, **6110**, 61100A-1 (2006).

[161] S. Maruo, K. Ikuta, and H. Korogi, *J. Micromech. Syst.*, **12**, 7 (2003).

[162] S. Maruo and J. T. Fourkas, *Laser & Photon. Rev.*, **2**, 100 (2008).

[163] C. A. Coenjarts and C. K. Ober, *Chem. Mater.*, **15**, 5556 (2004).

[164] K. K. Seet, V. Mizeikis, S. Matsuo, S. Juodkazis, and H. Misawa, *Adv. Mater.*, **17**, 541 (2005).

[165] L. Steidl, S. J. Jhaveri, R. Ayothi, J. Sha, J. D. McMullen, S. Y. C. Ng, W. R. Zipfel, R. Zentel, and C. K. Ober, *J. Chem. Mater.*, **19**, 437 (2009).